# Impact Of Local Structural Characteristics On Glass-formation In Metal-organic Frameworks

Madsen, Rasmus Skov Klitgaard

*DOI (link to publication from Publisher):*
10.54337/aau511959234

*Publication date:*
2022

*Document Version*
Publisher's PDF, also known as Version of record

# IMPACT OF LOCAL STRUCTURAL CHARACTERISTICS ON GLASS-FORMATION IN METAL-ORGANIC FRAMEWORKS

**BY**
**RASMUS SKOV KLITGAARD MADSEN**

DISSERTATION SUBMITTED 2022

AALBORG UNIVERSITY
DENMARK

# IMPACT OF LOCAL STRUCTURAL CHARACTERISTICS ON GLASS-FORMATION IN METAL-ORGANIC FRAMEWORKS

by

Rasmus Skov Klitgaard Madsen

AALBORG UNIVERSITY
DENMARK

Dissertation submitted

Dissertation submitted: November 2022

PhD supervisor: Prof. Yuanzheng Yue,
Aalborg University

PhD committee: Associate Professor Mads Koustrup Jørgensen (chair)
Aalborg University, Denmark

Professor Kasper Pedersen
Technical University of Denmark, Denmark

Professor Giulio Monaco
University of Padova, Italy

PhD Series: Faculty of Engineering and Science, Aalborg University

Department: Department of Chemistry and Bioscience

ISSN (online): 2446-1636
ISBN (online): 978-87-7573-792-5

Published by:
Aalborg University Press
Kroghstræde 3
DK – 9220 Aalborg Ø
Phone: +45 99407140
aauf@forlag.aau.dk
forlag.aau.dk



Printed in Denmark by Stibo Complete, 2022

# Rasmus S.K. Madsen

| | |
|---|---|
| **Personal Information and Education** | **Born:** December 1993, Øster Hurup, Denmark<br>**2013-2016:** Bachelor, Chemistry – Aalborg University<br>**2017-2018:** MPhil, Chemical Engineering – University of Queensland<br>**2019-2022:** PhD, Chemical Engineering – Aalborg University |
| **Work Experience** | **2015-2017:**<br>Science communicator – Kemishow Aalborg, Aalborg University<br>- Pop-science communication, Performing, teaching<br>**2014-2015:**<br>Laboratory Assistant – Environmental analysis, Eurofins<br>- Preparing samples for standardised testing, Managing and organizing samples |
| **Awards** | **2021:** Eliteforsk rejselegat (200.000 DKK) – uddannelses- og forskningsministeriet<br>**2018:** Oral Presentation award, 11th Aseanian Membrane Society conference, Brisbane Australia |
| **Publications** | **2019-2022:** 3 Peer-reviewed publications, including:<br>Madsen, R. S. K., Sarkar, S., Iversen, B. B., & Yue, Y. (2022). *Sensitivity of the glass transition and melting in a metal-organic framework to ligand chemistry*. Chemical Communications, 58(6), 823–826.<br>Madsen, R. S. K., Stepniewska, M., Yang, Y., Qiao, A., Winters, W. M. W., Zhou, C., König, J., Mauro, J. C., & Yue, Y. (2022). *Mixed metal node effect in zeolitic imidazolate frameworks*. RSC Advances, 12(17), 10815–10824.<br>**2017-2018:** 3 Peer-reviewed publications, including:<br>Madsen, R. S. K., Motuzas, J., Julbe, A., Vaughan, J., & Diniz da Costa, J. C. (2019). *Novel membrane percrystallisation process for nickel sulphate production*. Hydrometallurgy, 185, 210–217.<br>Madsen, R. S. K., Motuzas, J., Vaughan, J., Julbe, A., & Diniz da Costa, J. C. (2018). *Fine control of NaCl crystal size and particle size in percrystallisation by tuning the morphology of carbonised sucrose membranes*. Journal of Membrane Science, 567, 157–165. |

# ENGLISH SUMMARY

Metal-organic framework (MOF) is a group of materials comprised of metal nodes connected by organic ligands through coordination bonds. Due to their diverse structures, MOFs have attracted great attention from the research community for applications in areas including gas storage, energy, and gas separation. Zeolitic imidazolate framework (ZIF), a subset of MOFs, has recently been melted and quenched into glasses. Access to the glassy state of MOFs has immense potential for expanding their application range. However, most ZIFs and MOFs are known to thermally decompose without being able to melt. Computational work has been used to elucidate the melting- and glass-formation mechanism of ZIFs, though the inability to precisely relate structure to melting poses a major challenge for predicting new MOF glass formers. This work aims to elucidate the mechanism of vitrification through structural analyses by the following approaches. 1) using electron-donating moieties on linkers in a known MOF glass-former and relating the short- and long-range structure effects to the glass-forming mechanism. 2) gradually substituting metal nodes, relating structural changes and inductive effects to melting. 3) monitoring the metal node coordination environment during vitrification.

1) 5,6-dimethylbenzimidazolate (dmbIm) was incorporated into ZIF-62 [Zn (imidazolate)$_{1.75}$(benzimidazolate)$_{0.25}$]. The lattice volume increased in proportion to the quantity of benzimidazolate substituted with dmbIm. The melting point ($T_m$) and glass transition temperature ($T_g$) increased in response to the degree of substitution as well. The change in isobaric heat capacity over the glass transition decreases, as dmbIm content increases. The steric effect of the bulky linker causes a reduction in the degree of atomic freedom, resulting in the glass structure of high dmbIm content possessing a structure closer to the liquid state. Finally, the electron-donating effects of the methyl group appear to inductively stabilise the system against melting by increasing the Zn-N bond, hence increasing $T_m$.

2) the gradual substitution of metal nodes ($Co^{2+}$ and $Cu^{2+}$) in ZIF-62 and ZIF-4 [Zn (Imidazolate)$_2$], respectively, revealed the mixed metal node effect. The partial substitution of $Co^{+2}$ for $Zn^{2+}$ in ZIF-62 caused a non-linear, non-monotonic effect on $T_m$ and $T_g$. The lowest cobalt substitution led to an abrupt decrease in both the $T_m$ and $T_g$, followed by a subsequent increase with a further increase in the cobalt fraction. At complete exchange for cobalt, $T_m$ for Co-ZIF-62 is slightly higher than Zn-ZIF-62. Similarly, the introduction of a small quantity of copper into ZIF-4 produces a substantial decrease in $T_m$. Further substitution increases $T_m$ until the framework partially decompose before melting. The dissimilar electron affinity between the metal nodes is likely to partially weaken the Zn-N bonds. This weakening initiates the melting at lower temperatures, causing the framework connectivity to decrease, thus lowering $T_m$.

3) using $^{67}$Zn-NMR revealed that the Zn tetrahedral units in crystalline ZIFs can be described as two discrete Zn coordination environments. However, the vitrified ZIF samples had a single Zn peak described by a continuous distribution of coupling constants, signifying that the Zn sites become disordered during glass formation. The chemical shift is also shifting to higher fields, signifying a change in the average bond length.

By extension, it appears that the introduction of large moieties on organic ligands can be used to increase the lattice of ZIFs and attain a higher $T_g$ The electron-donating effects on the organic ligand are likely to strengthen the metal-to-linker bond, causing a higher $T_m$. The importance of the inductive effects is further highlighted by the mixed metal node effects observed by substituting zinc with cobalt and copper, where $T_m$ is decreased substantially by the addition of a small quantity of a second metal ion.

# DANSK RESUME

Metalorganisk rammestruktur (MOF) er en klasse af materialer bestående af metal-ioner der binder sig til brodannende organiske ligander gennem koordinationsbindinger. Mange forskningsområder har udvist stor interesse for MOFs på grund af den store strukturelle diversitet de tilbyder. Eksempler på potentielle applikationsområder oplagringsteknologier, energi, og separation. Nogle zeolit imidazol gitter (ZIF), en undergruppe af MOFs, har inden for de seneste år udvist evnen til at blive smeltet og omdannet til glas. Even til at omdanne MOFs til glas kan udvide deres anvendelsesområder. Størstedelen af ZIFs og MOFs dekomponerer før de smelter. Simuleringer af MOF systemer er blevet udført for at belyse smelte- og glasdannelsesmekanismen, dog er disse tiltag begrænset af at modellerne der bliver brugt, kan ikke pålideligt forudsige smelte evnen af potentielle nye MOF glas. Denne afhandling forsøger at belyse MOFs smelteegenskaber gennem følgende metoder. 1) indføre elektrondonerende funktionelle grupper på ligander i et MOF glasdannende system og relatere kort- og langtrækkende struktur til deres smelteegenskaber. 2) gradvist udskifte metal-ionerne i et glassdannende MOF krystal og relatere struktur ændringerne og de induktive effekter til smeltning. 3) Undersøge ændringerne i koordinationsmiljøet af metal-ionerne under glasdannelse.

1) 5,6-dimetylbenzimidazol (dmbIm) blev gradvist inkorporeret i ZIF-62 [Zn (imidazol)$_{1.75}$(benzimidazol)$_{0.25}$] i stedet for benzimidazol. Krystalgitter volumen steg med udskiftningsgraden af benzimidazol (bIm) for dmbIm. Smeltepunktet ($T_m$) og glasovergangstemperaturen ($T_g$) steg også med udskiftningsgraden. Ændringen i den isobariske varmekapacitet under glasovergagen viste sig at falde med introduktionen af dmbIm. Dette viser at strukturen af ZIF glas med højere dmbIm indhold har en struktur der er tættere på en underafkølet væske i forhold til den originale ZIF-62. Dette skyldes at de steriske effekter fra de funktionelle grupper reducerer den atomiske frihedsgrad. Stigningen i $T_m$ skyldes de elektrondonerende metylgrupper styrker Zn-N bindingerne in systemet.

2) kobolt og kobber blev gradvist udskiftet for zink i henholdsvist ZIF-62 og ZIF-4 (Zn (imidazol)$_2$), hvilket påviste en blandet metal effekt. Delvis udskiftning af kobolt for zink i ZIF-62 forårsager en ikke-lineær ikke-monoton effekt af $T_m$ og $T_g$. lav udskiftningsgrad af kobolt medfører et skarpt tab i $T_m$ og $T_g$, hvorefter begge stiger ved større udskiftningsgrad. $T_m$ for Co-ZIF-62 er højere end for rent Zn-ZIF-62. en lignende effekt blev observeret for ZIF-4. Ved introduktion af en lav mænge kobber ses en stor reduktion af $T_m$, som også stiger ved stigende mængde kobber, indtil at netværket begynder at dekomponere før det smelter. Zn-N bindingerne svækkes ved at introducere metal-ioner med højere elektronaffinitet. De svækkede Zn-N bindinger kan brydes ved lavere temperatur, som medfører lavere netværkssammenhæng og dermed smeltes de bi-metalliske prøver ved lavere temperatur.

3) $^{67}$Zn-faststof-NMR-analyse af zinkholdige ZIF krystaller viste, at to separate zink koordinationsmiljøer eksisterer. Disse separate koordinationsmiljøer omdannes til et enkelt Zn signal beskrevet af en kontinuer fordeling af koblingskonstanter. Dette viser at Zn tetrahedralerne bliver mere uordnet under glasdannelse. Derudover ændres det kemiske skifte, hvilket indikerer en ændring i bindingslængderne.

Dermed vises der at introduktionen af funktionelle grupper som øger krystalgitter volumen og resulterer i en øgning af $T_g$. Elektrondonerende effekter af funktionelle grupper resulterer i en øgning i $T_m$ ved at styrke koordinationsbindingerne mellem metalionerne og liganderne. Effekten af de induktive effekter er yderligere observeret ved substituering af zink for kobolt og kobber, hvor $T_m$ reduceres ved introduktion af en lille mænge af et sekundært metal.

# ACKNOWLEDGEMENTS

I would like to extend my deepest gratitude to my supervisor Professor Yuanzheng Yue for financing my PhD project with his research funds, which enabled me to begin my PhD studies under his supervision. Beyond this, I would like to thank him for his engagement with my project, our extensive and rigorous discussions have been invaluable for the completion of my project, by providing, and challenging ideas.

I would in addition to my supervisor like to thank all my colleagues at Aalborg university. The academic discussions we have had have seeded solutions to many challenges. Their input has helped me materialise and formulate explanations for novel phenomena encountered throughout my work.

My international collaborators must be thanked as well. Their willingness to participate in the joint research efforts has strengthened the content of my thesis, not only by the data their facilities have provided but also by their knowledge and expertise. Their contributions have strengthened the findings of this thesis, and I would be remiss for not acknowledging their impact on my project. Sabyasachi Sen, Zhehong Gan, Kuizhi Chen, Ang Qiao, John C. Mauro, Malwina Stepniewska, Yongjian Yang, Oxana Magdysyuk, and finally Satoshi Horike are some of my main collaborators, who's help have been instrumental for the success of my thesis. Thank you so much for the collaborations.

I would like to thank my family for being my support and inspiration to continue working on my project. They have been instrumental for keeping my morals high throughout my studies. So thank you very much for all the love and support.

Finally, thank you to the Danish ministry of higher education and science for awarding me with the Eliteforsk travel stipend. Their help allowed me to visit collaborators, which I would not have been able to do otherwise during this project

# TABLE OF CONTENTS

# LIST OF ABBREVIATIONS

Abbreviations are listed in alphabetical order.

| | |
|---|---|
| **ATR** | **Attenuated Total Reflectance** |
| **bIm** | Benzimidazolate |
| **ClbIm** | 5-Chloro-1H-benzimidazolate |
| **DCM** | Dichloromethane |
| **DEF** | N,N-Diethylformamide |
| **dmbIm** | 5,6-dimethylbenzimidazolate |
| **DMF** | N,N-Dimethylformamide |
| **DSC** | Differential Scanning Calorimetry |
| **EFG** | Electrical Field Gradient |
| **FT-IR** | Fourier Transform Infrared Spectroscopy |
| **GFQ** | Glass Forming Quality |
| **ICP-OES** | Inductively Coupled Plasma Optical Emission Spectroscopy |
| **Im** | Imidazolate |
| **MAS-NMR** | Magic angle spinning nuclear magnetic resonance spectroscopy |
| **MA** | Meltability, MA = $1 - (T_m/T_d)$ |
| **Me** | Metal |
| **MOF** | Metal-Organic Framework |
| **MS** | Mass Spectrometry |
| **NMP** | N-Methyl-2-pyrrolidone |
| **NMR** | Nuclear Magnetic Resonance spectroscopy |
| **PDF** | Pair Distribution Function |
| **PXRD** | Powder X-ray Diffraction |
| **RT** | Room Temperature |
| **SBU** | Secondary Building Unit |
| **S-NMR** | Solution Nuclear Magnetic Resonance spectroscopy |
| **STA** | Simultaneous Thermal Analysis |
| **TGA** | Thermogravimetric Analysis |
| **UV-VIS** | Ultraviolet-visible spectroscopy |
| **XRD** | X-ray Diffraction |
| **ZIF** | Zeolitic Imidazolate Framework |

# 1. INTRODUCTION

Glasses have been a fundamental material to human society since the development of tools from obsidian in the stone age (1). Technological developments through the ages have pushed glasses into increasingly advanced applications. The early applications like vessels for containing fluids and glass panes in windows have developed into tough and safe windshields on cars, and glassware capable of withstanding thermal shock found in laboratories or even in kitchen applications. In recent years, technological development has been driven by the implementation of glasses in less obvious applications, such as glass fibres for telecommunications (2) and glass matrices used in bone regeneration (3).

Glasses are amorphous materials, meaning that they are non-crystalline structures, and are more akin to the atomic structure of a liquid. This is traditionally achieved by quenching melts obtained via melting precursor materials and avoiding the formation of crystals before the liquid is cold enough that atomic rearrangement is no longer possible. This metastable state of matter behaves like solid materials, which with their generally good transparency is one of the initial advantages for their use (1). In principle, glasses are not defined by specific chemical compositions. Rather, glasses are defined by their physical state, structurally amorphous materials that are kinetically hindered from relaxing into a supercooled, unless when heated.

The chemical flexibility of glasses has resulted in the development of several glass families. Inorganic non-metallic glasses is the largest and most well-known family and contain silica ($SiO_2$) glasses, soda-lime-silica ($Na_2O$-CaO-$SiO_2$) glasses, and so on. Compared to inorganic non-metallic glasses, organic glasses (e.g., polystyrene) (4,5) are relatively new but are widely used in modern industry. These glasses consist of organic compounds (comprised of carbon-carbon and or carbon-hydrogen bonds) in their matrix. Metallic glasses were first reported 62 years ago (6) and consist of a purely metallic matrix. This group of glasses sports intriguing mechanical properties, however, are often limited due to their propensity for rapid crystallisation during quenching. The most recent addition to the glass family is metal-organic framework (MOF) glasses, which are unique due to their hybrid organic-inorganic structure. The first MOF glass was reported in 2015 by Bennett, Greaves, Yue, and collaborators (7).

Glasses are widely regarded as one of the most fascinating, yet not fully understood states of matter. The structure of glasses is still a major subject of debate (8). In 1995 Anderson expressed glasses as "*the deepest and most interesting unsolved problem in solid-state theory*" (9). The non-equilibrium state, the disordered atomic arrangement, and the structural changes during glass transitions all contribute to the mystery of glasses. Even in the current year, 2022, glasses garner such interest as the UN recognised 2022 as the UN international year of glass.

## 1.1. BACKGROUND AND CHALLENGES

The recent discovery of MOF glasses in 2015 lead to intense research interest (7). MOF glasses boast high surface areas and internal porosity (10), which makes them excellent candidates for separation applications (11) as well as for gas or energy storage (12). The flexibility in the choice of organic linkers enables fine control over pore size and surface area (13). In addition, the ability to use functional metal ions or clusters in MOFs has also attracted the attention of researchers in catalysis (14) as well as in energy storage (15). However, these technologies are limited by grain boundaries (11). This poses a major engineering challenge for the application of MOFs. Most common synthesis procedures of MOFs lead to the production of fine crystalline powder, with larger monolithic structures being hard to fabricate (16). The discovery that a subset of MOF, a zeolitic imidazolate framework (ZIF), ZIF-4 was able to be melted and quenched into glass provided a solution to the grain boundary issues. However, to this date, most MOFs and even ZIFs are known to thermally decompose before reaching their melting temperature ($T_m$) (17). The current understanding is that the structure dictates the melting behaviour of MOFs.

So far, the most successful series of meltable MOFs belong to the ZIF family (12). ZIFs are generally known to have good chemical and thermal stability (18), which is an asset for both glass formation and the practical application of ZIFs. Chemically, ZIF consists of metal ions that coordinate tetrahedrally, e.g., $Zn^{2+}$, $Cu^{+2}$, and $Co^{2+}$. These metal ions act as nodes and are bridged by imidazole-based ligands through Me-N (Me = metal) coordination bonds (19). The tetrahedral units are corner-sharing and are arranged in a 3D porous (19) network, with topologies akin to zeolites, thereby giving them the name (20). Once, vitrified, the structure resembles that of silica glasses, however, the size of the organic linkers causes the glasses to retain porosity (21).

The resultant MOF glasses present anomalous mechanical properties, e.g., indentation-induced shear bands (22), and a low fracture-toughness despite having a Poisson's ratio similar to ductile metallic and organic glasses (23). Moreover, the glasses of ZIF-62 [Zn $Im_{1.75}bIm_{0.25}$] display an unusually high glass-forming ability (GFA) ($T_g/T_m$) of 0.84, significantly above the "2/3 rule" that most glasses follow along with high resistance to recrystallisation (24). The ZIF-62 crystal family has presented a strong starting point for introducing functional groups like fluorine into the glass structure, which improves gas uptake while retaining a favourable GFA (25). The properties that predict the melting characteristics of MOFs are still poorly understood. This poses a major limitation to the development of this field of research.

## 1.2. OBJECTIVES

The ultimate objective of this PhD project is to further our understanding of the MOF melting and glass-forming mechanism. Structural analysis of MOF glass-formers at three different coordination lengths is carried out to reveal structural characteristics which govern the ability for MOFs to be melt quenched. Using the metal nodes as origin, these lengths-scales are defined in this project as long-range structure (> 20 Å), intermediate-range structure (8-20 Å), and short-range structure (8 < Å), with the metal nodes at the point of origin for these length scales. The following three points are the basis for the objectives of this thesis.

1. Elucidate the systematic effect of introducing a third linker to ZIF-62 on melting and glass formation. Relating this effect to the observed changes in long-range structure as well as intermediate-range structure.
2. Investigate the effects of introducing second metal nodes in ZIF crystals on melting and glass formation.
3. Use $^{67}Zn$ solid-state NMR to reveal the structural changes around the metal notes during the glass formation of ZIFs.

## THESIS CONTENT

The outline of this thesis is a thesis by publication. First, a literature review outlines the state-of-the-art knowledge within the field of MOFs and MOF glasses. The literature review (chapter 2) will summarise and highlight gaps in knowledge pertaining to the vitrification of MOF and will present the research strategy. The following three chapters (chapter 3-5) are peer revied papers (outlined below). The following chapters will outline unpublished research and discussions as well as the conclusion to this project (chapter 6-9).

Papers published:

I. Madsen, R. S. K.; Sarkar, S.; Iversen, B. B.; Yue, Y. Sensitivity of the Glass Transition and Melting in a Metal-Organic Framework to Ligand Chemistry. *Chem. Commun.* **2022**, *58* (6), 823–826. https://doi.org/10.1039/d1cc03541j.

II. Madsen, R. S. K., Stepniewska, M., Yang, Y., Qiao, A., Winters, W. M. W., Zhou, C., König, J., Mauro, J. C., & Yue, Y. (2022). Mixed metal node effect in zeolitic imidazolate frameworks. RSC Advances, 12(17), 10815–10824. https://doi.org/10.1039/d2ra00744d

III. Madsen, R. S. K.; Qiao, A.; Sen, J.; Hung, I.; Chen, K.; Gan, Z.; Sen, S.; Yue, Y. Ultrahigh-Field 67Zn NMR Reveals Short-Range Disorder in Zeolitic Imidazolate Framework Glasses. *Science* **2020**, *367* (6485), 1473–1476. https://doi.org/10.1126/science.aaz0251.

# 2. LITERATURE REVIEW

Metal-organic frameworks (MOFs) are generally thought of as a permanently porous coordination polymer (CP) networks with a 2D or 3D connectivity (19). MOFs are an emerging technology first coined in the 1990s by Yaghi et al. (26). Possessing metal nodes or ion clusters that are interconnected via organic ligands allows MOF to attain highly porous structures (10), with functionalities that enable them to potentially be used for many applications, e.g., separation and catalysis (13).

The presence of grain boundaries is known to impede the performance of some applications, e.g., membrane systems (11). However, the fabrication method of most MOFs results in the formation of fine crystalline powders (16), with large monoliths being hard to obtain. Therefore, finding methods to solve this issue has been an attractive area of research (13). At the forefront of this is the melt quenching of MOFs into glass monoliths, as achieved in 2015 (7). Beyond the ability to cast monolithic pieces, this also led to the discovery of a new glass type (7). Access to the vitrified state of MOFs presents unique areas of applications, like optics and more (27,28).

## 2.1. METAL-ORGANIC FRAMEWORK

Metal-organic frameworks are materials also known as porous coordination polymers (14) and belong to the more general group coordination polymers (19). Metal-organic frameworks are commonly defined as two- and three-dimensional porous crystalline materials, formed by having polydentate organic ligands coordinately bind with secondary building units (SBU), also more commonly referred to as metal cation salt or metal clusters (7,12,16,19,26,29). IUPAC defines MOFs as coordination compounds, which extend into two- or three-dimensional repeating entities while containing potential cavities/pores (30,31). Though crystallinity is not a requirement, most research focuses on the study of crystalline MOFs, as witnessed by the reported number of crystalline MOFs in the Cambridge Structural Database exceeding the number of glassy and amorphous MOFs by almost two orders of magnitude (19). What distinguishes MOFs from CPs is that the connectivity of the network must comprise 2D or 3D (generally porous) structures for the compound to be classified as a MOF (14,19).

Within the last 30 years, the vast majority of MOFs and CPs discovered have been crystalline (12). Crystalline materials are a state of matter described by the atoms, molecules, or ions being arranged in a pattern that repeats periodically in three dimensions (32,33). Consequently, by selecting any point inside a crystal (defined as lattice points), it is possible to move in straight lines from this point in such a way that a new point is reached, which is indistinguishable from the original point (32,33). In a perfect, infinite crystal, these paths can be multiplied by any integer and the atomic environment will be identical. Figure 2.1 illustrates the translational repeatability of lattice points in a crystal net.

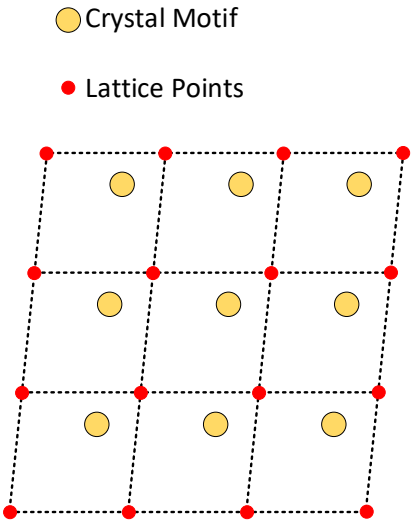


*Figure 2.1 Net of a lattice of red points in an arbitrary crystal structure of yellow spheres.*

By condensing the crystal structure to lattice points and connecting each point by lines, a unit cell is drawn. The unit cell is represented by a parallelepiped from which the entire crystal matrix can be constructed by translation of this unit (32,33). As such, unit cells are a convenient way of representing a crystal structure visually in the smallest possible way. A crystal lattice can be described by an infinite number of unit cells, because of this, the lattice is selected by the symmetries that are present in the structure (33). In general, higher symmetry crystals and smaller unit cell dimensions are preferred, when selecting the crystal structure (32).

Unit cells are divided into seven crystal systems (32). These crystal systems are triclinic, monoclinic, orthorhombic, tetragonal, rhombohedral, hexagonal, and cubic. In many contexts, these systems are segregated by the geometric characteristics of their lattice parameters, the length of the unit cell vectors ($a$, $b$, $c$), and the angles between them ($\alpha, \beta, \gamma$). Though this approach is convenient and frequently used, it is not completely appropriate. The crystal systems are defined by different essential symmetry operations. Examples of these symmetry operations are rotation, mirroring, translational symmetry and even combinations thereof. Table 2.1 outlines the symmetry operations that define each crystal system.

*Table 2.1 List of crystal systems and their essential symmetries. $C_n$ is an n-fold rotational symmetry* (32,33).

| Crystal System | Essential Symmetries |
|---|---|
| Triclinic | - |
| Monoclinic | One $C_2$ axis |
| Orthorhombic | Three $C_2$ axes |
| Tetragonal | One $C_4$ axis |
| Rhombohedral | One $C_3$ axis |
| Hexagonal | One $C_6$ axis |
| Cubic | Four $C_3$ axes in a tetrahedral arrangement |

Beyond the essential symmetries pertaining to the crystal systems, any given crystal can exhibit multiple additional symmetries. By incorporating all discrete symmetries that any crystal can possess, 230 unique combinations are possible. These 230 unique symmetry combinations are called space groups and are the most general way of classifying crystals by symmetry (33,34). MOFs display a diverse range of possible space groups, though many commonly used MOFs in research belong to the cubic system, as can be seen in Table 2.2

Many factors direct the structure of MOF crystals during synthesis. As an example, Yaghi et *al.* (35,36), synthesised 8 ZIF [Zn $Im_2$] (Im = imidazolate, $C_3N_2H_3^-$) structures from the same reactants (imidazole and zinc nitrate).

*Table 2.2 List of different MOFs, their crystal structure and examples of researched application areas.*

| Structure | Crystal System | Space group | Area of Research |
|---|---|---|---|
| UiO-66 | Cubic | $Fm\bar{3}m$ | Catalysis (37) |
| HKUST-1(Cu) | Cubic | $Fm\bar{3}m$ | Energy storage, energy conversion (38) |
| UiO-67 | Cubic | $Fm\bar{3}m$ | Catalysis (39) |
| MIL-101 | Cubic | $Fd\bar{3}m$ | Sorption, catalysis, sensor (40,41) |
| MIL-96 | Hexagonal | $P6_3/mmc$ | Gas storage (42) |
| ZIF-4 | Orthorhombic | $Pbca$ | Separation, energy storage (43) |
| ZIF-zni | tetragonal | $I4_1cd$ | Gas, olefin/paraffin separation (44) |
| ZIF-62 | Orthorhombic | $Pbca$ | Separation (45,46) |
| ZIF-7-I | Rhombohedral | $R\bar{3}$ | Gas separation (47) |
| ZIF-7-II | Triclinic | $P\bar{1}$ | Gas separation (47) |
| ZIF-7-III | monoclinic | $C2/c$ | Gas separation (47) |
| ZIF-8 | Cubic | $I\bar{4}\bar{3}m$ | Gas separation (48) |
| ZIF-67 | Cubic | $I\bar{4}\bar{3}m$ | $CO_2$ capture (35) |

Table 2.3 highlights 7 chemically identical ZIF networks, with different structures, based on the reactant ratio, reaction temperature, and solvents usage. ZIF- 3 and ZIF-6 have different space groups ($P4_2/mnm$ and $I4_1/amd$ respectively), which is caused by the difference in the solvent used. ZIF-6 is synthesised with N,N-dimethylformamide (DMF), while ZIF-3 uses DMF and N-methyl-2-pyrrolidone (NMP) as the solvents. This shift in structure originates from the solvent acting as a template during MOF formation. The solvent is adsorbed into the pores during synthesis, though no direct interaction with the framework occurs (13). This explains why solvents can be described as structure-directing agents. The structural difference between ZIF-1 and ZIF-6 is driven by the change in the ratio of the main reactants, i.e., Im and Zn-salt. This leads to the change from the tetragonal $I4_1/amd$ space group to the monoclinic $P2_1/n$. Hence, slight changes to solvothermal synthesis conditions can have a tremendous impact on the MOF structure.

*Table 2.3 Isochemical [Zn Im$_2$] ZIFs and their space group, imidazole/zinc reaction ratio, reaction temperature and solvents used for dissolving reactants. * denotes the use of different solvent mixtures to dissolve reactants.*

| Structure | Space group | Im/Zn ratio | Temperature [°C] | Solvents |
|---|---|---|---|---|
| ZIF-1 | $P2_1/n$ | 6.40 | 85 | DMF |
| ZIF-2 | $Pbca$ | 1.50 | 85 | DMF/DEF |
| ZIF-3 | $P4_2/mnm$ | 11.54 | 85 | DMF/NMP |
| ZIF-4 | $Pbca$ | 3 | 100 | DMF/DEF |
| ZIF-6 | $I4_1/amd$ | 11.95 | 85 | DMF |
| ZIF-10 | $I4/mmm$ | 2.66 | 85 | DMF + DMF/DEF* |
| ZIF-64 | $P2/n$ | 90 | 100 | DMF/DEF |

## 2.2. SYNTHESIS OF METAL-ORGANIC FRAMEWORKS

Metal-organic frameworks can be synthesised through numerous approaches. This section outlines the basic principle of 5 common synthetic routes employed to attain MOFs. These include: solvothermal, micro-wave assisted synthesis, sonochemical synthesis, electrochemical synthesis, and mechanochemical synthesis. The specific method imparts unique characteristics to the products. Some of the standout features and limitations are outlined to further highlight potential factors for deciding to use one synthesis approach over the other (e.g., good atom economy or scalable production).

MOFs are conventionally synthesised by solvothermal reactions. Solvothermal synthesis does not have an exact definition which is agreed upon (49). Despite there not being a precise definition, most definitions would agree that the reaction should take place in a closed vessel, above 373.15 K and above ambient pressure, as described by Rabenau (50). The reaction takes place in a selected solvent, in which the reactants are dissolved. Commonly, acetate or nitrate metal salts are used as the metal source for ZIFs (13). Figure 2.2 is a schematic representation of the prototypical solvothermal synthesis. Reactants are dissolved and transferred to an autoclave, which is sealed and heated until MOF crystals are produced. The simple experimental setup has made it one of the most widely used approaches for developing new MOF structures. This is in part due to the ease of synthesising many samples simultaneously (high throughput synthesis) (35). In addition to being an experimental setup with minimal setup requirements, solvothermal synthesis also reliably forms crystals large enough and of sufficient quality for single-crystal X-ray diffraction (35,51).

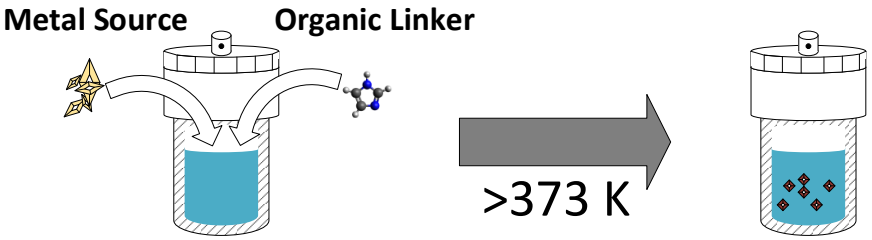


*Figure 2.2 Schematic of the solvothermal synthesis approach.*

While solvothermal synthesis is widely used, the time of production is a limitation. Micro-wave assisted synthesis, is an approach utilising the ability of micro-waves to make dielectric molecules align with the incident radiation (52). The flipping of the molecules causes the temperature to rise rapidly. This rapid increase in temperature enables MOFs to form at short time-scales. The shortened reaction time is one of the major advantages over solvothermal synthesis, as this approach requires more specialised equipment (52).

While Micro-wave assisted synthesis promise rapid synthesis, the specialised equipment is not always accessible. Sonochemical synthesis approaches rely on ultrasound to cause acoustic cavitation (53). This leads to areas in a solution to have rapid temperature fluctuations. The sonochemical synthesis approach has several desirable qualities: relatively simple in setup, rapid in time scale, and produces a high surface area product (53).

For the production of MOFs which has to adhere to a substrate, other strategies are often employed. Electrochemical synthesis or electrosynthesis generally involves one of two synthesis approaches: anodic dissolution or cathodic deposition (54). The former is an approach that has gained attention through the work of Mueller et *al.* (55), and is carried out by having the desired linkers in an electrolyte solution, and then submerging a metal anode. An applied voltage causes the metal to be oxidized to the ionic state and is then dissolved into the electrolyte, where it quickly reacts to form MOF crystals, which are then deposited onto the electrode. Cathodic deposition works by having a metal precursor, linkers, and a probase (56). The cathode will reduce the probase to the alkaline state, which enables the linker to be deprotonated due to the increased pH. The metal ion and the deprotonated linkers will then coordinate and precipitate as the MOF crystals. Figure 2.3 shows a basic concept of the synthesis approaches.

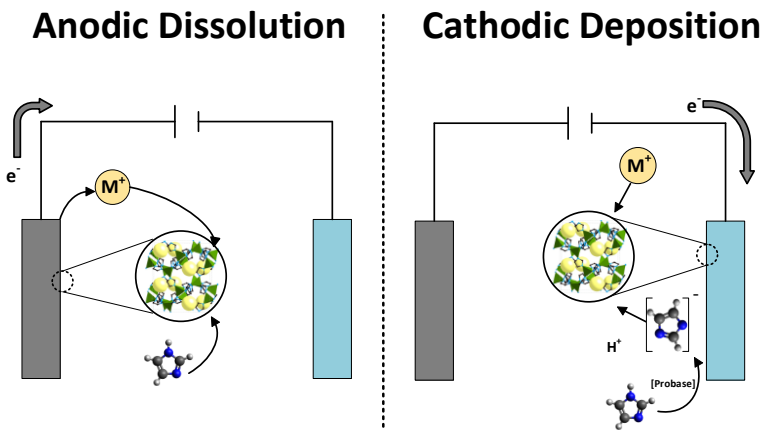


*Figure 2.3 Anodic dissolution (left) and cathodic deposition synthesis schematic. For anodic dissolution, the anode is oxidized and dissolved into the electrolyte, enabling crystal formation. For Cathodic deposition, the cathode enables deprotonation of the linker for reaction with a dissolved metal salt. The three-dimensional drawing is used from the work of Ortiz et al.* (57).

Mechanochemical synthesis exploits the ability to transfer energy to reactants via mechanical means, this typically involves ball-milling (58). The mechanical force of the ball-milling causes the intramolecular (e.g., N-H bonds in imidazole) bonds to be broken, which enables the reaction between metal nodes and organic ligands (59,60). Compared to conventional solvothermal synthesis, two of the major attractions of this method are the fast synthesis and low solvent consumption and good atom economy (61).

Despite many syntheses approaches available, a substantial fraction of all research output is still carried out by solvothermal synthesis, in part, this can be explained by the ability to do high throughput synthesis (35). Despite solvothermal synthesis being preferable in research, more scalable approaches can be used for industrial synthesis, especially for the application of MOFs on a larger scale (14).

## 2.3. APPLICATIONS OF METAL-ORGANIC FRAMEWORKS

MOFs are porous compounds and generally are considered to bridge micro- (2 < nm) and mesoporous compounds (2-50 nm) (10,62). Beyond highly tailorable pore sizes, MOFs also possess the ability to be used as sorbents with an extremely high measured Brunauer-Emmett-Teller (BET) surfaces, with some being able to exceed 10,000 $m^2 g^{-1}$, thereby outperforming the adsorption density capabilities of conventional activated carbons and zeolites (14). MOFs have attracted such attention, that they are being produced at the ton scales, with the most presently used MOFs being MIL-53, HKUST-1, Fe-BTC, and ZIF-8 (14). As expected from a compound that bridges the

functionality of inorganic and organic chemistry, the properties of MOFs are investigated for application in many areas, e.g., gas storage, energy conversion, sensing, drug delivery, catalysis, and energy storage (15,63–67).

In catalytic applications, the presence of a catalyst facilitates a reaction to occur quicker under milder conditions by lowering the activation energy for a reaction to occur (32). MOFs serve as excellent templates for catalysis (14). MOF catalysts can be designed and synthesised with direct catalytic application in mind, by selecting catalytically active metal nodes (such as Cr, Mn, Co, or Cu ions) (68–72). The porosity of MOFs enables them to act as a host for catalytic nano particles (73). The pores of MOFs can be used for catalysis by having specific organic ligands tune the pore size to enable size-selective catalytic reactions (74). Currently, MOFs have been used for the hydrogenation of unsaturated hydrocarbons, for instance, Zhang et al. used palladium in ZIF-8 for the conversion of 1-hexene to 1-hexane (75). Cu-BTC@$Fe_3O_4$ has been used for the reduction of nitroarene to anilines (76).

Perhaps more intuitively, MOFs display great potential for membrane and separation applications. Several approaches are used for preparing a selective membrane with MOFs (77). For instance, growing a selective layer of MOF crystals on a substrate or mixing crystalline materials into a mixed matrix membrane (78,79). MOF membranes have potential use in areas like natural gas purification, where certain ZIF-8 and UiO-66 mixed matrix membranes have surpassed the Robeson 2008 line of perm-selectivity (77,80). Similarly, hydrogen recovery and purification from hydrocarbon refineries is a topic of great interest (81,82). Several MOFs have been investigated, though ZIFs, UiO-66, and HKUST- and MIL-based MOFs represent the bulk of the research (77). Separation applications like $O_2/N_2$ and $C_3H_6/C_3H_8$ provide ample reason for their immense interest in separation processes. The substitution of metal nodes in MOFs displays the ability to tune properties for applications like gas separation (83,84). Indeed, bimetallic Co+Zn-ZIF-8 has been prepared by Kaur et al. (85), which shows that the incorporation of cobalt into Zn-ZIF-8 caused an increase in both surface areas and pore volume, resulting in a higher $CO_2$ and $H_2$ uptake. By extending the scope of application to the closely related coordination polymers (CP), it is possible achieve applications in proton conductivity (86) and general ion transport (19). As CPs exhibit different network connectivity compared to MOFs, CPs are only briefly mentioned in this thesis.

While there are plenty of promising applications for crystalline MOFs, there are generally some overlapping challenges for effective implementation in the industry: First, the stability of MOFs can be a limiting factor in many catalytic and separation applications (14,77). Many MOFs exhibit poor thermal stability as seen with paddlewheel containing structures (two metal nodes bound together by four bridging ligands), along with MIL-100 variants have decomposition temperatures ($T_d$) below 400 °C (36,87). The issue of stability is further exacerbated by several MOFs being reactive when submerged in water (88–90). Even exposure to moisture causes certain MOFs to collapse and dissolve (88,91,92).

Another concern is the emergence of grain boundaries, which limits the practical usability in membrane application of MOFs significantly (11,77). This is a major engineering challenge to overcome and is yet to be solved completely. However, the specific synthesis approach of the MOF could significantly affect the surface characteristics of the MOFs. Therefore, selecting an appropriate synthetic approach can elevate issues of grain boundaries and pinholes (56). However, in recent years, the development of meltable MOFs has shown to be a viable method for preparing MOF membranes (11).

## 2.4. MOF GLASSES

Most metal-organic frameworks are known to thermally decompose at rather low temperatures, even in a protective argon or nitrogen atmosphere, which has historically excluded MOFs from being melted into desired geometries (87). This made it arduous to prepare MOFs in complex geometries, as most synthesis approaches either result in fine crystalline powders or polycrystalline coatings on substrates (24,56,64). The grain boundaries and surface defects negatively impact the performance in various applications. Especially in MOF-based membranes used for gas and liquid separation. This issue has previously been addressed by novel synthesis approaches, which allow preparing high-quality coatings of MOFs on substrates. These synthesis approaches do however present inherent limitations. For instance, using cathodic deposition is only viable on conductive materials. Insulating materials, like polymeric substrates, would pose engineering challenges to attain a continuous coating of active MOF material on the surface if electrochemical synthesis is applied. Other synthesis approaches suffer from scaling issues such as solvothermal synthesis (93). Hence, being able to melt and cast MOFs would greatly improve the industrial viability of metal-organic frameworks, as this would remove the importance of the synthesis route for the fabrication of specific geometries.

In 2015, Bennet et *al.* (7) discovered through differential scanning calorimetry (DSC) that the zeolitic imidazolate framework, ZIF-4 (*Pbca*) exhibits several interesting thermodynamic responses to heating. Initial amorphization occurs, followed by recrystallisation into ZIF-zni ($I4_1cd$), with subsequent melting, as shown in Figure 2.4. Peak 1 is the amorphization into a low-density amorphous state at ~603 K, peak 2 is the transition to a high-density amorphous state at ~ 615 K, peak 3 is the recrystallisation into ZIF-zni at ~750 K, and peak 4 is the melting peak $T_m$ = 866 K of the ZIF-zni phase. On the second upscan, a glass transition peak (peak 5) $T_g$ = 565 K is the first reported case of a MOF glass. The discovery of MOF glasses is significant, as they do not belong to any conventional glass families. Conventional glasses are divided into three separate chemical groupings, non-metallic inorganic glasses, polymeric glasses and metallic glasses (4,5). Their characteristic chemical bonds are: ionic-covalent, covalent and metallic bonds respectively (4,5). MOF (and CP) glasses do not fit in any of these categories, as they are characterised by a hybrid organic-inorganic structure with the metal nodes being bridged by the organic ligands via coordination bonds (a weak sub-type of covalent bond (94)). Therefore, the reported ZIF glass by Bennett et al. is not only the first reporting of a MOF glass but also the discovery of an entirely new glass family.

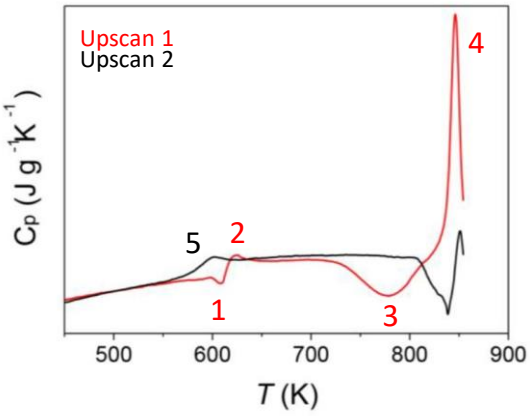


*Figure 2.4 DSC scan illustrating the calorimetric response of ZIF-4 and ZIF-8 during heating. ZIF-4 reveals the amorphization to a low-density and high-density state (1-2), followed by crystallisation to ZIF-zni (3), with subsequent melting (4). On the second upscan, a glass transition peak (5) is present. The figure is modified from the literature* (7)*.*

Unsurprisingly, the discovery of the new glass family evoked great interest in the glass research community (19). This interest is also extended to other fields like membrane science and more (12). This is partly due to the unprecedented opportunities the melting of MOFs affords. For glass researchers, the unique chemistry of MOFs provides exciting and new materials to be researched for the application of glassy materials. For membrane scientists, the casting of MOFs is a facile procedure for producing defect-free active layers on a membrane support. Moreover, by converting MOF crystals to glass, the properties will become isotropic, meaning performance is easier to exploit in engineering applications (12).

ZIF-62 [Zn $Im_{2-x}$ $bIm_x$] (bIm = benzimidazolate, $C_7H_5N_2^-$) glasses, were quickly found after the discovery of ZIF-4 glasses (24), which share the same space group and topology as ZIF-4 (95). However, the introduction of benzimidazolate into the structure significantly reduces the melting temperature ($T_m$) to 711 K, while retaining a similar $T_d$ (7,24). The increased working range ($T_d$ - $T_m$) is favourable as pieces of glass without visible signs of decomposition are easier to attain when compared to ZIF-4 (28,96,97). Beyond ZIF-4 and ZIF-62, several other MOF glass formers have been discovered. The closely related coordination polymers have also displayed great GFA (86,98). These exhibit interesting reversible transitions (86) and have potential uses in optics (99).

Table 2.4 outlines a list of predominantly ZIF crystals and their glasses. It should be noted that most of the current ZIF glass formers are based on a modified ZIF-62 composition, retaining the *Pbca* space group (21,27,100–105). The ability of ZIF-62 to

function as a template for novel MOF glasses suggests that the space group is likely tied to the melting mechanism.

*Table 2.4 non-exhaustive list of MOF glass formers.*

| Structure | Space Group | $T_m$ [°C] | $T_g$ [°C] | Research |
|---|---|---|---|---|
| ZIF-4 | $Pbca$ | 590 | 292 | (101) |
| [Zn $(Im)_2$] (GIS) | $I4_1/a$ | 584 | 292 | (101) |
| TIF-4 | $Pbca$ | 467 | 343 | (101) |
| ZIF-62 | $Pbca$ | 437 | 318 | (101) |
| ZIF-76 | $P\bar{4}3m$ | 451 | 310 | (21,100) |
| ZIF-UC-2 | $Pbca$ | 406 | 250 | (102) |
| ZIF-UC-3 | $Pbca$ | 390 | 336 | (102) |
| ZIF-UC-4 | $Pbca$ | 421 | 290 | (102) |
| ZIF-UC-5 | $Pbca$ | 266-423 | 296-336 | (100,102) |
| $Zn_{1-x}Co_x$-ZIF-62 | $Pbca$ | 399−452 | 331−334 | (27,103) |
| $[Co_{0.2}\,Zn_{0.8}\,(Im)_{1.95}\,(bIm)_{0.025}(ClbIm)_{0.025}]$ | $Pbca$ | 310 | 288 | (104) |
| $[Zn\,(Im)_{2-x-y}\,(bIm)_x\,(mbIm)_y]$ | $Pbca$ | 418−433 | 305−316 | (105) |

### 2.4.1. CALORIMETRIC PROPERTIES OF MOF GLASSES

Great efforts have been made through calorimetric studies to further understand the nature of the melting and vitrification mechanism of MOF glass-formers and in material science as a whole (106).

ZIFs glasses display a range of interesting calorimetric properties. Zhang et al. (107) revealed the presence of an exothermic release exhibited by ZIF-4 glass, which occurs at temperatures beyond $T_g$. The exothermic peak was initially ascribed to partial crystallisation, however, no appreciable changes in long-range structure could be detected. Therefore, the exothermic release is caused by a structural rearrangement via densification.

Qiao et *al.* (24) studied the calorimetric characteristics of ZIF-62. They showed that the heat of fusion ($\Delta H_f$) and entropy of fusion ($\Delta S_f$) increase in response to increasing benzimidazolate substitution. $\Delta H_f$ increases from 2924 to 4058 J $mol^{-1}$ as the bIm/(Im+bIm) ratio is increased from 0.1 to 0.22, while $\Delta S_f$ increases from 4.22 to 5.77 J $mol^{-1}$ $K^{-1}$. The larger bIm linker requires more thermal energy for structural reconfiguration. By extension, $T_m$ and $T_g$ both increased (708 to 724 K and 595 to 607 K respectively) in response to bIm substitution (24,108). They found that ZIF-62 exhibits an extraordinarily high GFA of 0.84, much higher than the empirical 2/3 Kauzmann law (5,109). The liquid fragility index *m* of ZIF-62 glasses is quite low (23), which approaches the value of silica glass ($SiO_2$) of $m = 21$ (110). The liquid fragility is a measure of the temperature dependence of the viscosity of the melt around $T_g$. The low fragility, mixed with the high viscosity ($\eta$) of $10^{5.1}$ Pa·S at $T_m$, makes ZIF-62 exhibit no appreciable recrystallisation when annealed at similar $T/T_g$ that would result in crystallization of silica glass (24). The inability to recrystallise ZIF-62 is in contrast to the fact that the Gibbs free energy difference between the supercooled liquid and the crystal state increases as T is lowered from $T_m$ (97).

Crystalline ZIFs are known to have interesting responses to pressure (111). Additionally, ZIF-4 crystals have demonstrated extremely high flexibility by their ability to convert into the zni phase during heating as well as converting to a monoclinic structure at elevated pressures. Beyond this, they have been shown to contract significantly during cooling (112). As an extension, Widmer et al. (113) developed a pressure-temperature (*P*-*T*) phase diagram for ZIF-62 and ZIF-4. They found two amorphous regions in ZIF-62 ranges initiated by either high pressure or high temperature. The two amorphous phases for ZIF-62 were determined to be significantly different in structure as observed by their e.g., different densities. In addition, they found that using elevated pressures promotes melting. The melting point decreased from 703 K to 633 K as pressures are an increase from $1 \cdot 10^{-4}$ to 2.1 GPa. Interestingly, the pressures required to extend the liquid range are within the realm of industrially achievable parameters. The decrease of $T_m$ at higher pressures show that ZIF-62 liquids are higher densities than their crystalline counterpart. This follows the exceptional negative thermal expansion observed in certain crystalline MOFs (18).

### 2.4.2. APPLICATION OF MOF GLASSES

The ability to cast MOFs into a bulk structure via melt quenching has enabled hitherto unfeasible applications. For example, using a vacuum hot press Qiao et al. (28) made high-quality glass samples, with good transmittance (up to 90%) in the visible and near-infrared wavelength. They produced samples with a refractive index similar to inorganic glasses (1.56). Further, Ali et al. (27) discovered that doping the ZIF-62 glasses with cobalt leads the glasses to exhibit mid-IR luminescence caused by the d-d transition of the $Co^{2+}$ ions. Photonics and optic application has thus been enabled through the vitrification of MOFs.

By vitrification of MOFs, the structure becomes isotropic, a feature that is desirable for applications where the properties have to be similar in any direction. What is more, this makes mechanical testing simpler and more feasible at macro-scale testing. Stepniewska et al. (22) found that the indentation of ZIF-62 glasses causes shear bands in the matrix. A feature that is unprecedented in fully polymerised glasses. The shear banding is attributed to the low bond strength of Zn-N coordination bonds (3,114), which are believed to break during indentation. Further, the Poisson ratio of ZIF-62 glass is 0.45, which is a significant departure from the crystalline ZIF-62 of 0.15 (24). Single-edge pre-crack beam experiments revealed, that despite the high Poisson ratio, ZIF-62 glasses exhibit very low fracture toughness (23). The low fracture toughness and the fact that Young's modulus of ZIF-62 is much greater than most elastomers means that ZIF-62 glasses occupy a new region of the Asby plot. The breaking of Zn-N bonds is ascribed to the low fracture toughness, similarly to the shear banding. This suggests that the mechanical properties of ZIF-62-based glasses provide a limited avenue for application for ZIF glasses where structural integrity is paramount. However, the unusual mechanical properties of MOF glasses are still of research interest.

As porosity and surface area are two major attractive aspects of MOFs, the development of porous vitrified MOFs has been a point of research. Initial work was based on dissolution-evaporation vitrification, where the evaporation of a plasticiser drives the vitrification of MOF (115). Only a few years later, Zhou et al. (21) found that melt-quenched ZIF-76 glass [Zn $Im_{1.62}$ 5-Clb$Im_{0.28}$] (5-Clb$Im_{0.28}$ = 5-chlorobenzimidazolate), which has a pore size distribution well within the range of microporous range. A year later (2019), Beyme et al. found that cobalt-containing ZIF-62 glasses possess accessible porosity as well (95). These studies served as a proof of concept that the fabrication of MOF glasses for membrane application would be possible. In 2020 Wang et al. (11) developed the first MOF glass membrane. They grew a polycrystalline ZIF-62 coating onto a membrane substrate. After coating, the membrane was heat treated to allow the ZIF-62 crystals to melt and produce a homogenous, defect-free layer. The membrane was then tested for single-gas permeance of $H_2$, $CO_2$, $N_2$, and $CH_4$, and the resultant ideal selectivity was calculated with the lowest reported being the $CO_2/N_2$ selectivity of 23, and the highest being $H_2/CH_4$ with 59. The isotropic and continuous layer provides several advantages, which conventional MOF separation systems suffer from. Some of these complications include grain boundaries, compatibility issues with substrates and or polymer matrices (116–118), and costs of production (119).

### 2.4.3. MELTING- AND GLASS-FORMATION MECHANISM

The potential application of MOF glasses, and the melting- and glass-formation mechanism of MOFs have garnered great interest. Computational modelling of MOFs (120,121), molecular density functional theory simulations (DFT) (122–124), and molecular dynamics (MD) simulations (125–130) have been applied to gain a fundamental understanding of the structure-property relationship within MOFs. Simulation-based studies have also extended their efforts to understanding and predicting the melting mechanism of MOFs. DFT has been used to probe the ZIF-4 structure during heating via calculation of the pair density function (PDF) evolution (131). In addition to this, they plotted the generalised Lindemann ratio of the Zn-N bonds as a function of temperature. This study shows that the melting of ZIF structures is likely enabled by the scission and renewal of these Zn-N bonds. Though the observed short-range order through PDF appears to be unchanged during vitrification (21). Subsequent simulation work has expanded on the scission and renewal hypothesis, by linking the coordination bond strength to melting ability (114). By extension, introducing metal nodes or ligands that affect these bond strengths are believed to correlate directly with the melting temperature (114). Through simulation work of MOFs provides a strong foundation for our understanding of MOFs, simulations are still limited by the quality of the models used. As an example, the current models using Lindemann's criterion for melting are known to be imprecise for determining $T_m$ (132).

Following up on the computational work, Gómez et al. (105) produced a series of 3-linker ZIF-62/TIF-4 crystals called ZIF-UC-1 [$Zn_1$ $(Im)_{2-x-y}$ $(bIm)_x$ $(mbIm)_y$] (mbIm = 5-methylbenzimidazole). The melting- and glass-formation behaviour of these crystals were studied by DSC. The introduction of a third ligand consistently reduces $T_m$ (between 691 and 704 K), while possessing a $T_g$ higher than ZIF-4 but lower than ZIF-62 and TIF-4 (between 578 and 589 K). They proposed a statistical model for the distribution of the different linkers and connected these to the glass transition. Bumstead et al. (104), further expanded on this idea, by modifying ZIF-62 in three different steps: 1) introducing a chlorine functional group onto the benzimidazole unit. 2) preparing a ZIF-62 with both benzimidazolate and chlorobenzimidazolate. 3) using the triple linker ZIF template, with partial substitution of cobalt for zinc. They propose that the disorder introduced by adding several different metal nodes and linkers causes a direct destabilisation of the crystal, causing a lowering of $T_m$. Hou et al. (102), synthesised a series of modified ZIF-62 crystals, exchanging benzimidazolate with halogenated benzimidazolate units. They found that the inductive effect of the halogen functional groups correlated well with the observed decreases in $T_m$. They further argue that the dispersive effects of having bulkier ligands, as well as a higher density structure, stabilise dissociated ligands, which in turn lowers $T_m$.

## 2.5. SUMMARY AND RESEARCH GAPS

Through this short literature review, it is clear that there is a great incentive for producing new MOF glasses, as these materials possess several properties that have great potential applications. The current state-of-the-art research and knowledge are, however, predominantly covering crystalline MOF materials. This is the case in terms of understanding the structure and properties. Given that most metal-organic framework decomposes readily before reaching $T_m$. More efforts in elucidating the melting mechanism are necessary. The primary limitation is that MOFs generally decompose prior to melting, as such the ability of the MOF to melt is low. In this thesis, this ability to melt is named the meltability and is defined as MA = 1 – ($T_m$/$T_d$) in this work. Hence, a MOF can be melted and quenched into a glass, if the MA is above 0. What is more, MA directly describes the fraction of the stable region which is in the liquid state. The combination of GFA and MA enables further points for discussion of the glass forming quality (GFQ) of a MOF, i.e., the ability of the MOF to produce homogenous glasses.

Based on the simulation work it is suggested that the melting of ZIFs is driven by the breaking of the metal-to-nitrogen bonds, however, there is little experimental evidence that shows the short-range structural disorder that would be expected (21). While there has been made several advances in our experimental understanding of the melting mechanism. There is still no definitive model for predicting the melting temperature, which means any discovery of new MOF glasses is based on a trial-and-error approach. Therefore, more efforts should be put into relating structural characteristics to the melting- and glass-forming behaviour of MOFs.

Because of the recent advancement in NMR (nuclear magnetic resonance spectroscopy) technology, there are now 35.2-tesla hybrid magnets available (133). Such a powerful magnet would be able to provide significant insight into the otherwise hard-to-analyse $^{67}$Zn-isotope. $^{67}$Zn is a quadrupolar isotope with low natural abundance, low gyromagnetic ratio and large quadrupole moment ($Q$) (134). The reason solid-state NMR analysis of $^{67}$Zn would be of interest is that using this on crystalline and glassy ZIF-4 and ZIF-62 would provide structural information on the chemical structure, as well as the spatial disorder through the electrical field gradient (EFG) (135). The EFG is a second-rank tensor, which responds to positional and orientational structure at distances of nearest and next nearest neighbour (i.e., Zn-N bonds and Zn-N-C bonds). The EFG is encoded into the coupling constant $C_Q$ and the asymmetry parameter $\eta_Q$ of the system (135). Given the complications associated with the $^{67}$Zn-isotope, previous $^{67}$Zn-NMR studies have focused on crystalline samples, some of which include crystalline MOFs (135–140). The absence of studying amorphous Zn-materials may in part be ascribed to the poor signal quality and peak broadening that would be characteristic of weaker magnetic fields.

The inductive effect of functional groups as well as the dispersive stabilisation effects should be further investigated. It is currently unclear if the dispersive effect outlined in the work of Hou et al. (102) is the main contributing factor for ZIF-UC-3 being the sample with the lowest $T_m$. As the crystal structure contains significant quantities of DMF in the pores, which potentially skews the density to be higher. The effects of introducing cobalt outlined in the work of Bumstead (104) were only for a single Co/Zn ratio. Therefore a systematic approach should be conducted to reveal the effect of mixing multiple metal nodes on $T_m$ and $T_g$. The ultimate goal is the separation of the inductive and dispersive effects. The importance of systematic composition is to reveal any non-linear, non-monotonic effects, e.g. mixed modifier and mixed alkali effects seen in oxide glass (141,142). The use of powder refinements can be used to determine changes in lattice volume caused by bulky functional groups added to linkers (143,144). The potential steric effects of bulkier linkers will be discussed, in relation to their inductive and dispersive effects (145).

The subsequent chapters of this thesis present published and unpublished experimental work, which seeks to bridge the gaps in knowledge outlined in this chapter. With particular interest, the inductive and steric effects of adding functional groups onto the ligands. Inductive effects from substituting metal nodes in known ZIF glasses will be investigated. And finally, the short-range structure evolution during glass formation will be studied.

# 3. SENSITIVITY OF THE GLASS TRANSITION AND MELTING IN A METAL-ORGANIC FRAMEWORK TO LIGAND CHEMISTRY

This chapter includes a scientific paper titled “Sensitivity of the glass transition and melting in a metal-organic framework to ligand chemistry” (DOI: 10.1039/D1CC03541J) published in Royal Society of Chemistry Chemical Communications volume 58, issue 6, 2022, page 823-826 (146). Both the main article and supplementary information have been included in this chapter. Note that the paper is written as a standalone text. This means that the figure, table references and citations do not adhere to the citation format of the thesis, however, the citations have been added to the bibliography of the thesis.

This chapter elucidates the effect of systematic variation of lattice parameters in a modified ZIF-62 crystal, by substituting 5,6-dimethylbenzimidazole (dmbIm) for benzimidazole. Both $T_m$ and $T_g$ increase as the lattice volume is increased by the introduction of dmbIm. The electron-donating methyl groups increase the Zn-N bond strength, which, in conjunction with increased topological constraints by the bulky methyl groups, causes both $T_m$ and $T_g$ to increase. The findings of this work suggest that the metal-to-nitrogen coordination bond is paramount to the melting and glass formation of MOF glasses, as in accordance with the computational work of Coudert et *al.* (114). Further, the increase in $T_g$ and $T_m$ contradicts the findings of Bumstead and Gómez (104,105). The introduction of the dmbIm linker appears to have a stabilizing effect on the framework rather than reducing the energy barrier for melting.

**Acknowledgement:** Reproduced from Chemical Communication with permission from the Royal Society of Chemistry.

**Citations used exclusively in published paper (first appearance):** (147)

# SENSITIVITY OF THE GLASS TRANSITION AND MELTING IN A METAL-ORGANIC FRAMEWORK TO LIGAND CHEMISTRY

Rasmus S. K. Madsen [a], Sounak Sarkar [b], Bo Brummerstedt Iversen [b] and Yuanzheng Yue *[a]
[a]Department of Chemistry and Bioscience, Aalbrog University, 9220 Aalborg, Denmark. E-mail: yy@bio.aau.dk
[b]Department of Chemistry, Aarhus University, 8000 Aarhus, Denmark

Received 1st July 2021, Accepted 7th December 2021

First published on 10th December 2021

## 3.1. ABSTRACT

The effect of substituting linkers with electron-donating moieties for part of the conventional ones on the melting and glass transition behaviours of ZIF-62 was investigated by calorimetry and X-ray diffraction. Specifically, substituting 5,6-dimethylbenzimidazole for benzimidazole in ZIF-62 increases both $T_m$ and $T_g$. The structural origin of this effect was explained.

Metal-organic frameworks (MOFs) are compounds consisting of metal nodes and organic ligands in permanently porous 2D and 3D structures[1]. MOFs have received intense interest from numerous fields of research for their varied chemistry and porosity, e.g., membranes[2], photonics[3], sensoring[4], and so on. However, the conventional synthesis leads to the formation of fine crystalline MOF powder, but cannot create bulk MOF pieces. The MOF powders cause grain boundaries, which inhibit their use in separation processes. The emergence of melt-quenched (MQ) glasses of MOFs has broadened the potential applications by enabling the fabrication of monolithic pieces of MOFs[2,5,6]. Most of the known MOFs thermally decompose prior to melting, but only a handful of MOFs are known to melt to date, most of which are their subsets, namely, zeolitic imidazolate frameworks (ZIFs) and coordination polymers [5,7–10]. ZIFs are structurally similar to zeolites, with tetrahedral transition metal nodes (e.g. $Zn^{2+}$) substituting for $Si^{4+}$ and imidazole-based ligands replace bridging oxygen, meaning their structures are analogous, as depicted in Fig. 1[11].

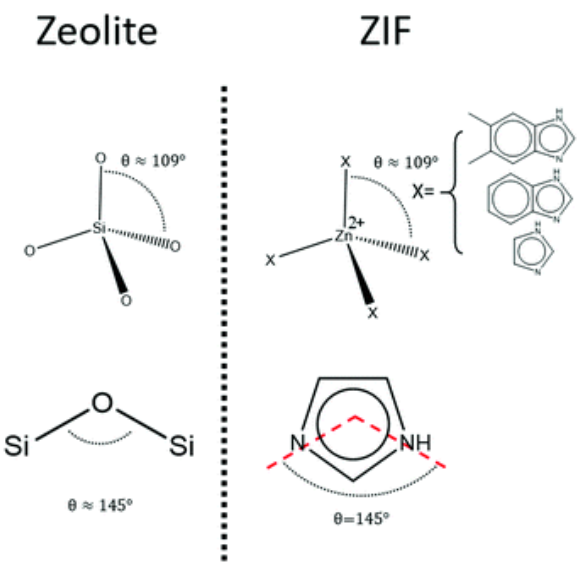


**Fig. 1** Graphical illustration of the structural similarity between zeolites and ZIFs: the tetrahedral Zn substitutes for Si, with a x–Zn–x bond angle of approximately 109°, and imidazole-based ligands substitutes for bridging oxygen with an angle of approximately 145°. X represents the imidazole-based ligands used in this work.

As MOF-glasses are a new family of melt-quenched glasses, which were discovered in 2015[5], the MOF melting and glass formation are still far from a thorough understanding. A study by Gaillac et al. showed in silico that the melting mechanism of MOFs is driven by a scission and renewal process of the organic linkers[12]. This was supported by Madsen et al. [13], who revealed through ultrahigh magnetic field solid-state $^{67}$Zn-NMR that the melting and glass formation of ZIFs causes the tetrahedral Zn sites to lose short-range (sub 7 Å) structural order, i.e., the structure becomes significantly disordered around the Zn sites upon melting-vitrification.

The prototypical ZIF network former, ZIF-4 [Zn $Im_2$] (where Im is imidazolate ($[C_3H_3N_2]^-$)), shows several intriguing thermodynamic behaviors, e.g. polyamorphic transitions prior to crystallization and melting, as well as indicating slight densification upon heating above their glass transition temperature ($T_g$)[5,14]. By partially substituting bIm (benzimidazolate, $[C_7H_5N_2]^-$) for Im, ZIF-62 [Zn $Im_{2-x}$ $bIm_x$] is generated. The thermodynamic and kinetic responses of ZIF-62 to heating are significantly different from that of ZIF-4, with the loss of polyamorphic transitions before melting, an increased melt stability range ($T_d$–$T_m$, where $T_d$ and $T_m$ are thermal decomposition temperature and melting point, respectively), and an ultrahigh glass forming ability[8].

Despite their huge difference in thermodynamic properties, ZIF-4 and ZIF-62 glasses possess a similar local structural environment, i.e., the highly disordered tetrahedral units as probed by $^{67}$Zn-MAS-NMR[12], suggesting that they still undergo similar melting processes. Zhou et al. studied the permanently porous MOF glasses[7]. In their study they revealed that substituting moieties from an electron withdrawing group to an electron donating group increases the stability of the MOF structure, as described by Hou et al.[15], who modified ZIF-62 based networks with halogenated benzimidazole units.

The present work attempts to give new insight into the MOF melting and glass formation by investigating the change in thermodynamic values (such as $T_m$, the heat of fusion, $\Delta H_f$, and change in isobaric heat capacity during the glass transition $\Delta C_p$) and the glass transition temperature ($T_g$) with gradual substitution of dmbIm (5,6 dimethylbenzimidazolate $[C_9H_{10}N_2]^-$) for bIm in the ZIF-62 network. In contrast to previous studies, we investigate the ability to tune the glass forming characteristics as well as the lattice parameters of the ZIF network structure by varying the fractions of three different linkers, Im, bIm, and dmbIm. By performing Differential Scanning Calorimetry (DSC), we found that both the glass transition and melting of ZIF-62 are very sensitive to substitution of the third component (dmbIm) for part of bIm, while the high glass forming ability is maintained. This finding is crucial for tuning of the thermodynamic and dynamic properties of MOF glasses by varying linker chemistry.

All ZIF samples were prepared by a modified solvothermal synthesis approach reported elsewhere[8], gradually substituting dmbIm for bIm. Full Synthesis parameters are given in the ESI (S1). The crystalline nature of the samples were verified by X-ray powder diffraction (XRPD). Further, structureless profile fitting based on Le bail method[16] was employed to these powder patterns to confirm the bulk phase purity of the samples. The crystalline structure of the samples was verified by X-ray powder diffraction (XRPD)(S2, ESI) and were refined by Le Bail fitting as stated in the ESI (Fig. S1–S7). The as-synthesised crystals were subjected to DSC upscans to determine the melting point ($T_m$) and heat of fusion of the crystals ($\Delta H_f$). The crystals were heated in the DSC to a temperature above $T_m$ and then quenched to the glass state. The $T_m$ and $\Delta H_f$ values are determined from the first DSC upscan curves, while the $T_g$ value is obtained from the second upscan curve. The details of the DSC measurements are given in ESI (Fig. S4, S8 and S9), and described in a review article[17]. Liquid NMR analysis was done to determine the chemical composition of the synthesised ZIFs as seen in the ESI (Fig. S5, S10 and S11).

Fig. 2A shows a comparison in the diffraction patterns between the crystalline samples and the simulated ZIF-62 data found in literature.[18] It is seen that there is a good agreement between them, indicating that the samples possess the long–range structure of ZIF-62 crystals. However, as dmbIm is fully substituted for bIm, some of the diffraction peaks change concerning their shape, though the diffraction pattern overall agrees with the reference. In detail, the two peaks at diffraction angles $2\theta \approx 14.0$ and 17.2° appear and minor peak shape differences are apparent for 0.24-ZIF-62 at scattering angles 18–22°. Le Bail fittings of each XRD diffractogram (Fig. S1–S4, ESI) revealed that all samples agree well with the Pbca space group of ZIF-62. The fittings were based on the initial cell parameters Henke's group provided in a published study [18].

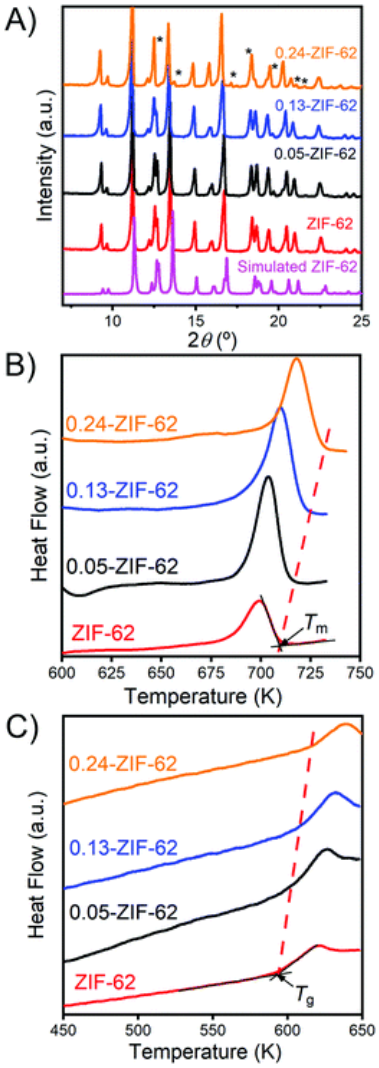


**Fig. 2** (A) XRPD patterns of Simulated ZIF-62[18] (magenta), ZIF-62 sample (red), 0.05 ZIF-62 (black), 0.13 ZIF-62 (blue), 0.24 ZIF-62 (orange). Asterisks (*) marks the peak differences observed between the simulated ZIF-62 and the pure dmbIm ZIF-62 crystal sample. (B) DSC upscan 1, $T_m$versus composition. (C) DSC upscan 2, $T_g$ versus composition.

The Le Bail fittings reveals that the unit cell parameters increase almost linearly as the bulkier dmbIm unit is incorporated into the structure as seen Fig. 3 and the ESI (Fig. S5–S7). This adherence to Vegard's law[19] is an expected effect of the inclusion of the methyl groups, causing the linkers to increase in size. The ability to tune the lattice parameters is an important aspect of crystal engineering and materials science.

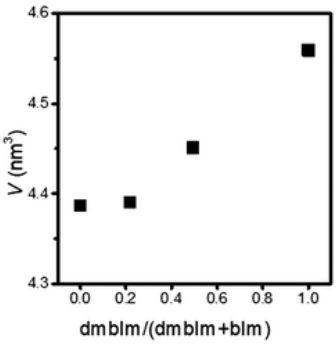


**Fig. 3** Increase in unit cell volume with substitution of dmbIm for bIm.

Each of the designations is based on the dmbIm content within the crystal structure, as verified by liquid $^{1}$H-NMR, as detailed in Table 1 with the integrated area derived from the peaks associated with each linker, as seen in ESI (Fig. S10 and S11). The ZIF crystals possess linker molar ratios that are close to the designed ones, i.e., the Zn : Im : bIm : dmbIm ratios: 1 : 1.74 : 0.26, 1 : 1.75 : 0.19 : 0.05, 1 : 1.74 : 0.13 : 0.13, and 1 : 1.76 : 0.24. For convenience, the samples will be named x-ZIF-62, (e.g. 0.13-ZIF-62), where x is the dmbIm molar content, while the sample without dmbIm substitution will be referred to as ZIF-62. Fig. 2B and C demonstrate the DSC signals for both the crystalline samples and the glassy ones, respectively. It is clearly seen that all the crystalline samples undergo the melting process during the first upscan and the glass samples are subjected to glass transition during the second upscan.

**Table 1** Comparison between the designed reaction molar ratio for the linkers and the actual ratios obtained from the integrated areas of $^{1}$H-NMR peaks associated with each linker

| **Reaction ratio [Im : bIm : dmbIm]** | **Integrated area [Im : bIm : dmbIm]** | **Relative ratio [Im : bIm : dmbIm]** |
|---:|:---:|:---:|
| 13.5 : 1.5 : 0 | 1 : 0.15 : 0 | 1.74 : 0.26 : 0 |
| 13.5 : 1 : 0.5 | 1 : 0.11 : 0.030 | 1.75 : 0.19 : 0.05 |
| 13.5 : 0.5 : 1 | 1 : 0.075 : 0.073 | 1.74 : 0.13 : 0.13 |
| 13.5 : 0 : 1.5 | 1 : 0 : 0.134 | 1.76 : 0 : 0.24 |
| **Note: Zn is set as 1.00.** | | |

In addition, all the crystalline samples show the desolvation event during heating (Fig. S8, ESI) and no mass loss during melting. The melt-quenched samples are transparent, implying their glassy nature. Fig. 4A reveals how the glass transition temperature increases from 596 to 609 K, as dmbIm is introduced. This is explained by the electron-donating effect of the methyl-groups partially offsetting the destabilising effects of introducing a larger ligand into the structure, as reported by Qiao et al.[7] and Bennett and Horike [20]. $T_g$ is linked to the size of organic ligands, i.e., increasing the ligand size results in an increase in $T_g$. Fig. 4B exhibits an increase in $T_m$ of the modified ZIF-62 from 720 K to 734 K, as dmbIm gradually substitutes bIm, indicating that the presence of two methyl groups in the benzimidazole unit stabilises the framework structure. This effect is in line with the consequence of adding two electron-donating groups to the linker, i.e., the stabilisation of the coordination bonds[15], and hence, of the crystal structure. Both $T_g$ and $T_m$ increase as more dmbIm is introduced regardless of the Im to bIm + dmbIm ratio.

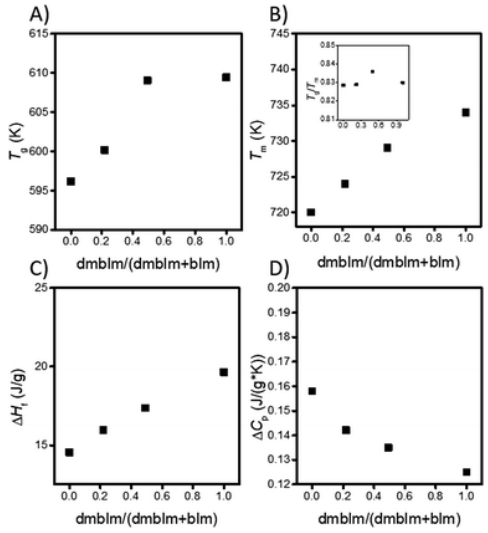


**Fig. 4** Dynamic and thermodynamic properties of ZIFs as functions of dmbIm content. (A) $T_g$; (B) $T_m$, Inset: $T_g/T_m$; (C) heat of fusion ($\Delta H_f$). (D) Jump of the isobaric heat capacity during glass-liquid transition ($\Delta C_p$).

This is in contrast to the finding of Henke et al.[21] according to which the glass transition and melting point of unmodified ZIF-62 are greatly affected by the bIm content. The $T_g/T_m$ values of all the modified ZIF-62 systems are in the range of 0.82–0.84 (insert of Fig. 4B, being similar to the findings of Qiao et al.[8]), implying that these systems have ultrahigh glass forming ability since $T_g/T_m$ is a measure of the glass forming ability. Interestingly, this trend is independent of the bIm content in the crystals. Therefore, the increase of both $T_m$ and $T_g$ is attributed to the structurally stabilizing effect of dmbIm. The stabilising effect of the electron-donating groups is also observed in Fig. 4C, where the heat of fusion ($\Delta H_f$) is depicted as a function of dmbIm

content. $\Delta H_f$ is observed to increase from 14.6 to 19.6 J $g^{-1}$ as dmbIm is introduced into the structure. This approximately linear increase in melting enthalpy remains if the heat of fusion is converted to a molar unit instead, meaning that the substitution correlates well with the observed change in the heat of fusion. Fig. 4D shows that the compositional effect on the isobaric heat capacity change ($\Delta C_p$) during the glass transition, that is, $\Delta C_p$ decreases with substituting dmbIm for bIm. This indicates that the glasses with higher dmbIm content are located higher in the potential energy landscape, compared to that of conventional ZIF-62 glass. The decreasing trend of $\Delta C_p$ is consistent for both weight- and molar-based units. This agrees fairly well with the notion that the linkers cause the diffusion of partially uncoordinated linkers to be more sluggish, and hence the configuational arrangements and the degree of disorder in the glass can be expected to be close to those of the supercooled liquid state.

The explanations about the origin of the change in the measured properties (Fig. 4) are supported by the Le Bail fittings that reveals the increasing trend of the unit cell size with the substitution of dmbIm for bIm (Fig. 3). It is known that $T_g$ increases with a decrease in the topological degree of atomic freedom[22]. The increase of the unit cell size implies that the structural units become bigger, leading to the increased steric hindrance, and hence, the increased barriers for structural rearrangement. Specifically, the ligand substitution lowers the atomic freedom, and makes translational and rotational motion, as well as configurational rearrangement more difficult. This explains why both $T_g$ and $T_m$ increase with the linker substitution (Fig. 4).

By gradual chemical modification of ZIF-62 crystals, we have discovered that the incorporation of bulky electron-donating methyl-groups into ZIF-62 structures makes possible to tune the melting behaviour, as well as the glass transition, without lowering the glass forming ability of the precursor crystals.

This work confirms that it is feasible to introduce additional linkers into the ZIF-62 framework by changing the conventional synthesis parameters. The outcome of this work is useful for designing new MOF glasses for applications, where these properties need to be optimized. The dynamic and thermodynamic properties can be modified without changing the overall crystal structure or the glass forming ability. This work has broaden the current understanding of the melting behavior and the glass formation of MOFs. In addition, the effects of the third linker on the porosity, pore structure, and properties of ZIF glasses should be explored in future, using the approaches described elsewhere[7,23–25].

RSKM performed conceptualisation, data curation, formal analysis, investigation, methodology, writing the original draft, visualisation, validation as well as most software used. YZY did funding acquisition, project administration, supervision, investigation, validation, review and editing, providing resources as wells as partaking in the conceptualisation. SS performed formal analysis, validation of data, methodology for parts of the analysis, as well as review and editing. BBI conducted supervision, discussion, the resource acquisition, validation, review and editing.

## 3.2. CONFLICTS OF INTEREST

There are no conflicts to declare.

## 3.3. REFERENCES


1 O. M. Yaghi, M. O'Keeffe, N. W. Ockwig, H. K. Chae, M. Eddaoudi and Jaheon Kim, Nature, 2003, 423, 705–714.

2 Y. Wang, H. Jin, Q. Ma, K. Mo, H. Mao, A. Feldhoff, X. Cao, Y. Li, F. Pan and Z. Jiang, Angewandte Chemie - International Edition, 2020, 51, 4365–4369.

3 A. Qiao, H. Tao, M. P. Carson, S. W. Aldrich, L. M. Thirion, T. D. Bennett, J. C. Mauro and Y. Yue, Opt Lett, 2019, 44, 1623.

4 M. Safaei, M. M. Foroughi, N. Ebrahimpoor, S. Jahani, A. Omidi and M. Khatami, TrAC - Trends in Analytical Chemistry, 2019, 118, 401–425.

5 T. D. Bennett, J. C. Tan, Y. Yue, E. Baxter, C. Ducati, N. J. Terrill, H. H. M. Yeung, Z. Zhou, W. Chen, S. Henke, A. K. Cheetham and G. N. Greaves, Nat Commun, 2015, 6, 1–7.

6 M. Stepniewska, M. B. Østergaard, C. Zhou and Y. Yue, J Non Cryst Solids, 2020, 530, 119806.

7 C. Zhou, L. Longley, A. Krajnc, G. J. Smales, A. Qiao, I. Erucar, C. M. Doherty, A. W. Thornton, A. J. Hill, C. W. Ashling, O. T. Qazvini, S. J. Lee, P. A. Chater, N. J. Terrill, A. J. Smith, Y. Yue, G. Mali, D. A. Keen, S. G. Telfer and T. D. Bennett, Nat Commun, 2018, 9, 1–9.

8 A. Qiao, T. D. Bennett, H. Tao, A. Krajnc, G. Mali, C. M. Doherty, A. W. Thornton, J. C. Mauro, G. N. Greaves and Y. Yue, Sci Adv, 2018, 4, DOI:10.1126/sciadv.aao6827.

9 T. D. Bennett, Y. Yue, P. Li, A. Qiao, H. Tao, N. G. Greaves, T. Richards, G. I. Lampronti, S. A. T. Redfern, F. Blanc, O. K. Farha, J. T. Hupp, A. K. Cheetham and D. A. Keen, J Am Chem Soc, 2016, 138, 3484–3492.

10 D. Umeyama, S. Horike, M. Inukai, T. Itakura and S. Kitagawa, J Am Chem Soc, 2015, 137, 864–870.

11 K. S. Park, Z. Ni, A. P. Côté, J. Y. Choi, R. Huang, F. J. Uribe-Romo, H. K. Chae, M. O'Keeffe and O. M. Yaghi, Proc Natl Acad Sci U S A, 2006, 103, 10186–10191.

12 R. Gaillac, P. Pullumbi, K. A. Beyer, K. Chapman, D. A. Keen, T. D. Bennett and F. X. Coudert, Nat Mater, 2017, 16, 1149–1155.

13 R. S. K. Madsen, A. Qiao, J. Sen, I. Hung, K. Chen, Z. Gan, S. Sen and Y. Yue, Science (1979), 2020, 367, 1473–1476.

14 J. Zhang, L. Longley, H. Liu, C. W. Ashling, P. A. Chater, K. A. Beyer, K. W. Chapman, H. Tao, D. A. Keen, T. D. Bennett and Y. Yue, Chemical Communications, 2019, 55, 2521–2524.

15 J. Hou, M. L. Ríos Gómez, A. Krajnc, A. McCaul, S. Li, A. M. Bumstead, A. F. Sapnik, Z. Deng, R. Lin, P. A. Chater, D. S. Keeble, D.

A. Keen, D. Appadoo, B. Chan, V. Chen, G. Mali and T. D. Bennett, J Am Chem Soc, 2020, 142, 3880–3890.

16 le Bail A., Duroy H. and FourQuet J. L., Mat. Res. Bull., 1988, 23, 447–452.

17 Q. Zheng, Y. Zhang, M. Montazerian, O. Gulbiten, J. C. Mauro, E. D. Zanotto and Y. Yue, Chem Rev, 2019, 119, 7848–7939.

18 L. Frentzel-Beyme, M. Kloß, R. Pallach, S. Salamon, H. Moldenhauer, J. Landers, H. Wende, J. Debus and S. Henke, J Mater Chem A Mater, 2019, 7, 985–990.

19 Denton A. R. and Ashcroft N. W., Phys Rev A (Coll Park), 1991, 43, 3161–3164.

20 T. D. Bennett and S. Horike, Nat Rev Mater, 2018, 3, 431–440.

21 L. Frentzel-Beyme, M. Kloß, P. Kolodzeiski, R. Pallach and S. Henke, J Am Chem Soc, 2019, 141, 12362–12371.

22 M. M. Smedskjaer, J. C. Mauro, R. E. Youngman, C. L. Hogue, M. Potuzak and Y. Yue, Journal of Physical Chemistry B, 2011, 115, 12930–12946.

23 S. Horike, N. Ma, Z. Fan, S. Kosasang and M. M. Smedskjaer, Nano Lett, , DOI:10.1021/acs.nanolett.1c01594.

24 J. Fonseca, T. Gong, L. Jiao and H. L. Jiang, J Mater Chem A Mater, 2021, 9, 10562–10611.

25 M. Stepniewska, K. Januchta, C. Zhou, A. Qiao, M. M. Smedskjaer and Y. Yue, , DOI:10.1073/pnas.2000916117.

Supporting Information

# Sensitivity of the Glass Transition and Melting in a Metal-Organic Framework to Ligand Chemistry

Rasmus S.K. Madsen[a], Sounak Sarkar[b], Bo Brummerstedt Iversen[b], and Yuanzheng Yue*[a]

[a]: Department of Chemistry and Bioscience, Aalborg University, 9220 Aalborg, Denmark. E-mail:

[b]: Department of Chemistry, Aarhus University, 8000 Aarhus, Denmark

## SI-1: Synthesis approach for ZIF-62 and dmbIm-modified ZIF-62

All chemicals in this approach were used from the supplier without further purification. $Zn(NO_3)_2 \cdot 6H_2O$ (≥99.0 %), imidazole (99.5 %), benzimidazole (98%), 5,6 dimethylbenzimidazole (≥99 %) Were all acquired from Sigma-Aldrich. Lastly, Dimethylformamide (DMF) (99.9 %) and Dichloromethane (≥99.8%) was purchased from VWR chemicals.

Each sample was prepared by weighing the appropriate mass (Table S1) of zinc nitrate hexahydrate, imidazole, benzimidazole, and 5,6-dimethylbenzimidazole and add them into a beaker in the sequence mentioned, followed by the addition of 50 mL DMF. The solutions were stirred for 30 minutes before being transferred into 100 mL Teflon-lined autoclaves and sealed tightly. The autoclaves were placed in an oven at 130 ºC for 96 hours. The autoclaves were left in the oven to cool naturally to ambient temperature overnight. The synthesised crystals were recovered and washed three times with approximately 40 mL DMF, followed by a single wash using ~40 mL of dichloromethane. The washed crystals were placed in an oven at 110 ºC to dry overnight.

*Table S5 Mass of reactants used for the synthesis of ZIF-62, 0.05-ZIF-62, 0.13-ZIF-62, and 0.24-ZIF-62.*

| ZIF composition | $Zn(No_3)_2 \cdot 6H_2O$ [g] | Imidazole [g] | Benzimidazole [g] | 5,6-dimethylbenzimidazole [g] |
|---|---|---|---|---|
| **ZIF-62** | 1.7460 | 5.3282 | 1.6268 | 0 |
| **0.05-ZIF-62** | 1.7544 | 5.3639 | 0.6912 | 0.4392 |
| **0.13-ZIF-62** | 1.7452 | 5.3224 | 0.3337 | 0.8514 |
| **0.24-ZIF-62** | 1.7571 | 5.3206 | 0 | 1.2738 |

## SI-2: X-ray powder diffraction of modified ZIF-62

All powder samples were initially desolvated at 350 ºC in a protected argon atmosphere to remove residual solvent trapped in the pores of the framework. The X-ray powder diffraction (XRPD) experiments were carried out on a Malvern Panalytical Empyrean instrument equipped with a Cu X-ray source and a PIXcel$^{1D}$ detector. A 0.04 Rad soller, 1/8º fixed divergence slit, 1/4º anti-scatter slit, and a 10 mm beam mask was equipped at the incident beam side. On the diffracted beam side, a 7.5 mm anti-scatter slit, a large nickel filter, and a 0.04 Rad soller was equipped. The program was set to scan from 5-45 º with a step size of 0.006565 º, with the sample spinning with a revolution time of 4 seconds and a count time of 58 seconds. The samples were placed on an amorphous Si substrate purchased from Malvern Panalytical.

## SI-3: Le Bail Fitting and Cell Parameters

The Le Bail fittings were done on the collected XRD diffractograms, using the Fullprof Suite software package. The XRD patterns were refined to a Pbca space group with the starting cell parameters being based on the work of Sebastian Henke[1]. The final refinements are depicted in Fig. S1-4. Fig. S5-S7 reveals the resultant cell parameters as a function of the 5,6-dimethylbenzimidazole content.

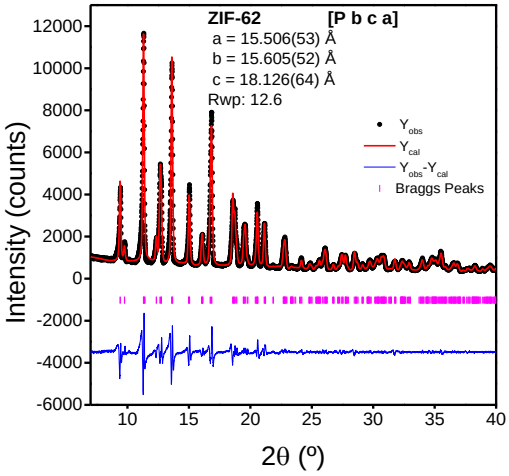


*Fig. 1 Difference plot for the Le Bail fitting of the ZIF-62 sample.*

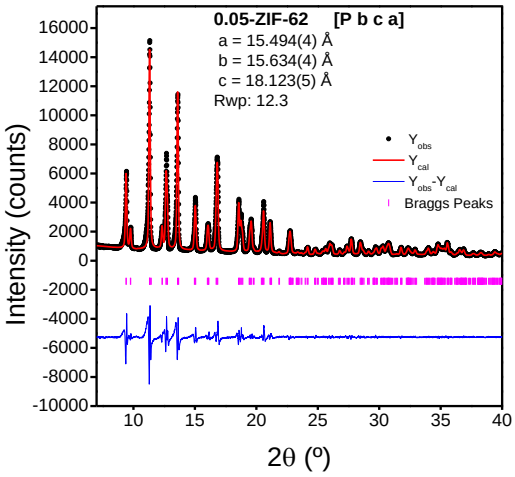


*Fig. 2 Difference plot for the Le Bail fitting of the 0.05-ZIF-62 sample.*

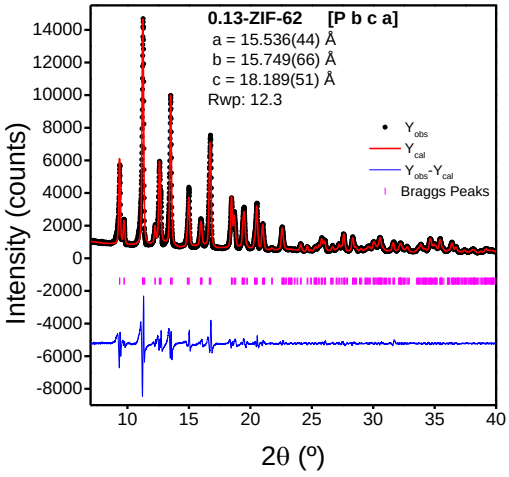


*Fig. 3 Difference plot for the Le Bail fitting of the 0.13-ZIF-62 sample.*

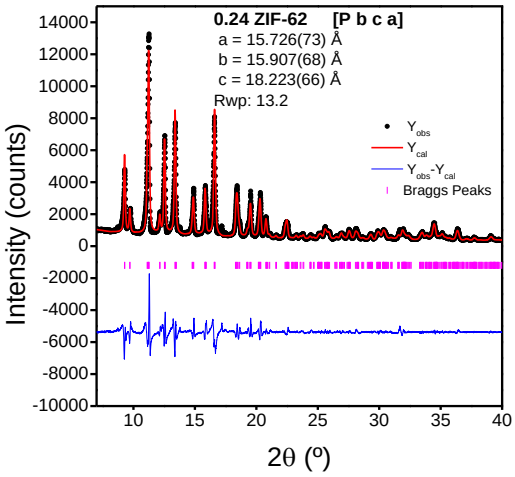


*Fig. 4 Difference plot for the Le Bail fitting of the0.24- ZIF-62 sample.*

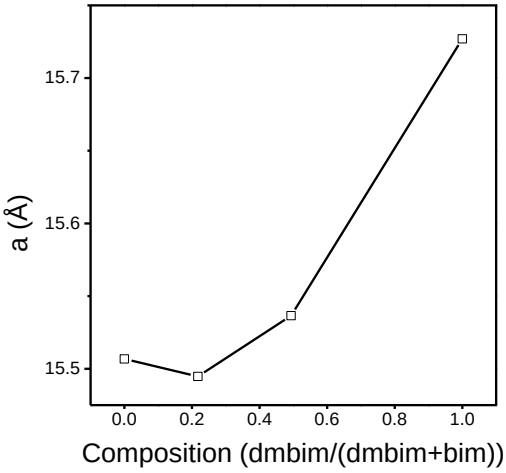


*Fig. 5 Cell parameter a, as a function of the 5,6-dimethylbenzimidazole substitution degree. The substitution reveals to cause an increase in a.*

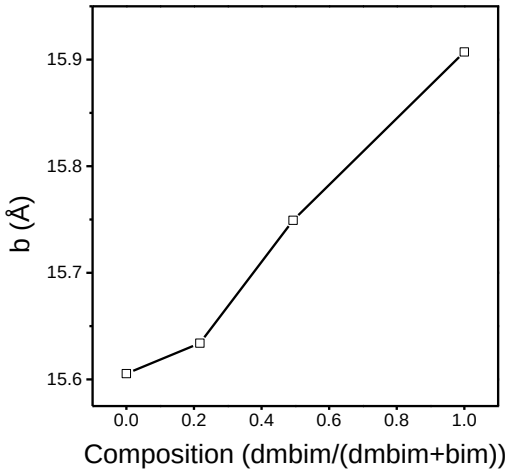


*Fig. 6 Cell parameter b as a function of the 5,6-dimethylbenzimidazole substitution degree. The substitution reveals to cause an increase in b.*

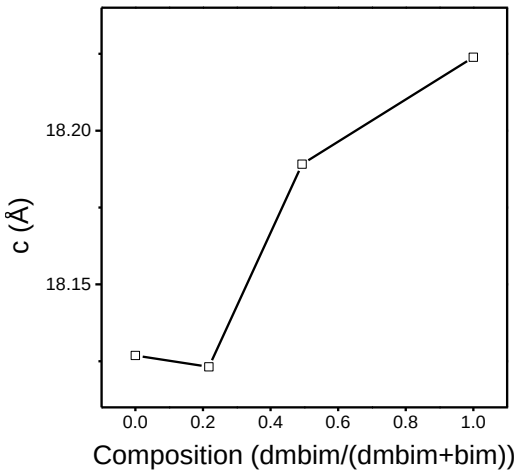


*Fig. 7 Cell parameter c as a function of the 5,6-dimethylbenzimidazole substitution degree. The substitution reveals to cause an increase in c.*

## SI-4: Simultaneous thermal analysis of modified ZIF-62

All as-synthesised ZIF samples were initially tested for melting behaviour using a DSC program outlined in Table S2. A Netzsch STA 449 F1 was used for all measurements. The change of isobaric heat capacity was measured by a separate program (Table S3) using sapphire as the reference. Both set of measurements were done using Pt crucibles, with a blank run serving as the background. Argon was used as both the purge gas (50 mL $min^{-1}$ flow) and protective gas (20 mL $min^{-1}$ flow) during the measurements.

*Table S6 DSC/TGA program used for initial analysis of the ZIF-62, 0.05-ZIF-62, 0.13-ZIF-62, and 0.24-ZIF-62 samples.*

| **Type** | **Temperature [K]** | **Rate [K $min^{-1}$]** |
|---|---|---|
| **Dynamic** | 746 | 10 |
| **Dynamic** | 353 | 10 |
| **Dynamic** | 746 | 10 |
| **Dynamic** | 473 | 10 |
| **End** | - | - |

*Table S7 DSC/TGA program used for sapphire-calibrated heat capacity measurements of the ZIF-62, 0.05-ZIF-62, 0.13-ZIF-62, and 0.24-ZIF-62 samples.*

| **Type** | **Temperature [K]** | **Rate [K $min^{-1}$]** | **Isotherm [min]** |
|---|---|---|---|
| **Dynamic** | 743 | 30 | - |
| **Isothermal** | 743 | - | 5 |
| **Dynamic** | 423 | 10 | - |
| **Isothermal** | 423 | - | 5 |
| **Dynamic** | 693 | 10 | - |
| **Dynamic** | 423 | 40 | - |
| **End** | - | - | - |

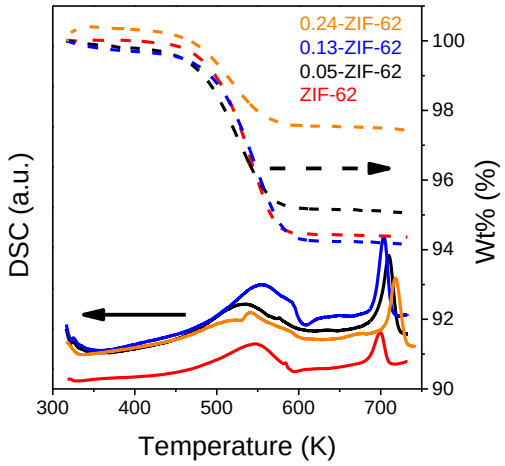


*Fig. 8 DSC/TGA 1st-upscan of ZIF-62 (red), 0.05-ZIF-62 (black), 0.13-ZIF-62 (blue), and 0.24-ZIF-62 (orange). The solid lines are the DSC signal, while the dashed lines are the measured Wt.% remaining. The measurement done here was in accordance with Table S3. The measurement reveals a decrease in solvent released as approximately 550 K as dmbIm content is increased.*

*Fig. 9 Optical images of the four ZIF samples tested. left to right, ZIF-62, 0.05-ZIF-62, 0.13-ZIF-62, and 0.24-ZIF-62 are displayed to reveal their transparency.*

## SI-5: Liquid Nuclear Magnetic Resonance Spectroscopy Measurements

A Bruker Avance III 600 MHz spectrometer was used for the liquid NMR measurements. All samples were digested using a 1:5 (by volume) mixture of deuterated Dimethyl Sulfoxide (DMSO) (VWR, 99.80% $^{2}H$) and hydrochloric acid (Aldrich, 35% conc., 99% $^{2}H$). 200 µL were transferred to 3 mm NMR tubes. 1D $^{1}H$ NMR spectra were collected at 308.1 K. The NMR measurements were conducted using the following pulse sequence: a 1D experiment with composite pulses was used based on the work of Bax [2]. Water suppression was achieved by a 5s continuous-wave irradiation of $\gamma \cdot B_1/2\pi = 50$ Hz. The total recycle delay was 28s. Fig. S9 depicts the $^{1}H$-NMR spectra of each of the ZIF samples.

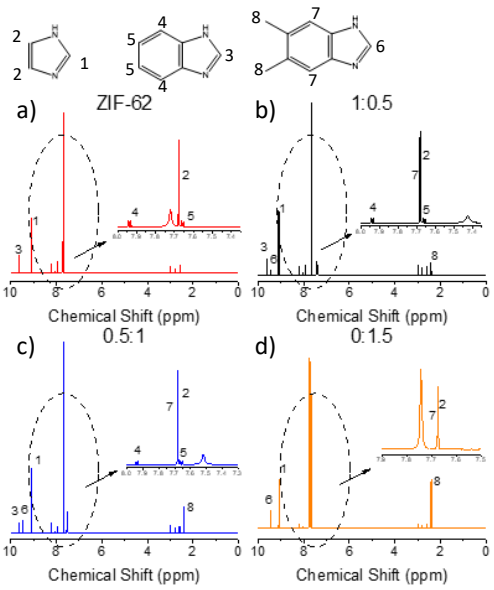


*Fig. 10 [1]H-NMR spectrum of a) ZIF-62, b) 0.05-ZIF-62, c) 0.13-ZIF-62, d) and 0.24-ZIF-62. The peaks used for identification and quantification of the individual linkers (Imidazole, benzimidazole, and 5,6-dimethylbenzimidazole) are labelled 1-6 in the structure schematic above.*

## Bibliography


1 L. Frentzel-Beyme, M. Kloß, R. Pallach, S. Salamon, H. Moldenhauer, J. Landers, H. Wende, J. Debus and S. Henke, J. Mater. Chem. A, 2019, 7, 985–990.

2 A. Bax, J. Magn. Reson., 1985, 65, 142–145.

# 4. MIXED METAL NODE EFFECT IN IMIDAZOLATE FRAMEWORKS

This chapter is the scientific paper titled “Mixed metal node effect in zeolitic imidazolate frameworks” (DOI: 10.1039/D2RA00744D) published in Royal Society of Chemistry Advances volume 12, issue 17, 2022, page 10815-10824 (148). Both the main article and supplementary information have been included in this chapter. Note that the paper is written as a standalone text. This means that the figure, table references and citations do not adhere to the citation format of the thesis, however, the citations have been added to the bibliography of the thesis.

Chapter 3 dealt with the effect of long-range structural characteristics on the thermodynamic responses, by modification of the organic linkers. This chapter deals with the effect of metal nodes on the thermodynamic responses and focuses more on the local bonding environment of the metal nodes and the effects changes to this will have. In this paper, two series of bimetallic (Co/Zn) zeolitic imidazolate frameworks were synthesised. It is discovered that introducing cobalt into the crystal structure of ZIF-62 and related structures non-monotonic, non-linear responses on $T_m$ and $T_g$ as cobalt substitutes for zinc. This effect is similar to the mixed modifier effect in oxide glasses and is hence called the mixed metal node effect. The origin of this effect is explained by two effects: one, the structural difference between zinc ions and cobalt ions. Two, the difference in electronic configuration, enhances atomic vibrations.

**Acknowledgement:** Reproduced from RSC Advances with permission from the Royal Society of Chemistry.

**Citations used exclusively in published papers (first appearance):** (149–161)

DOI: 10.1039/D2RA00744D (Paper) RSC Adv., 2022, **12**, 10815-10824

# MIXED METAL NODE EFFECT IN ZEOLITIC IMIDAZOLATE FRAMEWORKS

Rasmus S. K. Madsen‡ [a], Malwina Stepniewska‡[a], Yongjian Yang‡[b], Ang Qiao[c], Wessel M. W. Winters[a], Chao Zhou[a], Jakob König[d], John C. Mauro*[b] and Yuanzheng Yue*[a]

[a]Department of Chemistry and Bioscience, Aalborg University, Aalborg, DK9220, Denmark. E-mail: yy@bio.aau.dk

[b]Department of Materials Science and Engineering, The Pennsylvania State University, USA. E-mail: jcm426@psu.edu

[c]Wuhan University of Technology, Wuhan, 430070, China

[d]Advanced Materials Department, Jožef Stefan Institute, Ljubljana, 1000, Slovenia

Received 3rd February 2022, Accepted 26th March 2022

First published on 7th April 2022

## 4.1. ABSTRACT

We synthesized two series of bimetallic (zinc and cobalt) zeolitic imidazolate frameworks (ZIF-62) under different solvothermal conditions. It is found that the structure of the derived ZIF crystals is highly sensitive to synthesis conditions. One series possesses the standard ZIF-62 structure, whereas the other has a mixed structure composed of both the standard structure and an unknown one. The standard series exhibits a slight negative deviation from linearity of melting temperature ($T_m$) and glass transition temperature ($T_g$) with the substitution of Co for Zn. In contrast, the new series displays a stronger negative deviation. These negative deviations from linearity indicate the mixed metal node effect in bimetallic ZIF-62 due to the structural mismatch between $Co^{2+}$ and $Zn^{2+}$ and to the difference in their electronic configurations. The new series involves both cobalt-rich and zinc-rich phases, whereas the standard one shows one homogeneous phase. Density functional theory calculations predict that the substitution of Co for Zn increases the bulk modulus of the ZIF crystals. This work indicates that the structure, melting behaviour, and mechanical properties of ZIFs can be tuned by metal node substitution and by varying the synthetic conditions. Both series of ZIFs have higher glass forming abilities due to their higher $T_g/T_m$ ratios (0.77–0.84) compared to most good glass formers.

Electronic supplementary information (ESI) available: Optical images, SEM images, EDX elemental mapping, XRD patterns, $^1$H-NMR spectra, ATR FT-IR spectra, ICP-OES ratio, DSC scans, TGA data, and DTA-MS analysis. See DOI: 10.1039/d2ra00744d

‡ These authors equally contributed to this work.

## 4.2. INTRODUCTION

Metal-organic frameworks (MOFs) are a class of compounds consisting of metal nodes interconnected by organic ligands to form a 2D or 3D porous structure.[1–4] MOFs have received intense interest from chemists and materials scientists since their tunable composition and structure enable potential applications such as catalysis, gas storage, gas separation, and sensors.[5,6] Conventional synthesis approaches of MOFs enabled the formation of fine crystalline powders with the fabrication of large monolithic pieces that were difficult to be obtained.[7] The fine powder of MOFs results in interface interactions and grain boundaries, which are two major engineering challenges in gas or liquid separation.[8–10] It is known that some zeolitic imidazolate frameworks (ZIFs) (a subset of MOFs), which contain imidazole-based ligands that coordinate tetrahedrally to metal ions, forming zeolite crystal topologies, can be melted and then quenched to bulk glass.[2,11–13] MOF glasses are a new family of melt-quenched glasses, which differ from other families such as inorganic, organic, and metallic glasses in terms of chemical bonds, chemical composition, and topological structure. MOF glasses have shown a range of superior properties, e.g., ZIF-62 (Zn $Im_{2-x}$ $bIm_x$, Im: imidazolate; bIm: benzimidazolate) possesses an ultrahigh glass forming ability ($T_g/T_m$ > 0.84, where $T_g$ is the glass transition temperature, and $T_m$ is the melting point), and high resistance to crystallisation[12]. While other ZIF glasses like ZIF-76 (Zn $Im_{2-x}$ 5-$CbIm_x$, 5-CbIm: 5-chlorobenzimidazole) high porosity.[13] Solid-state $^{67}$Zn nuclear magnetic resonance (NMR) spectroscopy revealed that the melting and glass formation of ZIFs led to a high degree of structural disorder.[14] Wang et al.[8] recently developed the first glassy MOF membrane, in which ZIF-62 glass was used as the active membrane material on an alumina support. Bulk ZIF-62 glass shows high light transmittance (90%) in the visible range,[15] and possesses anomalous mechanical properties.[16,17] Henke et al.[18] revealed that substituting cobalt for zinc in ZIF-62 results in a meltable Co-ZIF-62 phase of the same space group as conventional ZIF-62, i.e., Pbca. Bimetallic ZIFs could be produced by introducing two types of metal nodes.[19–21] Most research has focused on bimetallic ZIF-8/ZIF-67 [Zn/$Co_1$ $MeIm_2$], (MeIm = 2-methyl imidazole), within the realm of catalysis.[19–21] A recent study by Bumstead et al.[22] investigated the effect of structural disorder within a ZIF-62-type network. They found that the $T_m$ decreased as they introduced cobalt into the zinc network. Zn/Co-ZIF-62 exhibits super-broadband mid-infrared (Mid-IR) luminescence,[23] which is important for photonic applications. Recently, the computational modelling of ZIFs (and MOFs)[24,25] through density functional theory (DFT)[26–29] and molecular modelling[30–36] has been conducted to understand the effect of both nodes and linkers[37] on the ZIF structure.

In this work, we report a systematic study on the effect of metal substitution on thermodynamic, kinetic, and mechanical properties in Co/Zn-ZIF-62 series. Two series of Co/Zn ZIF crystals were synthesized via a solvothermal method. The first series was Co/Zn-ZIF-62 (Pbca space group) based on the work of Henke et al.[18] The second series was synthesized by the experimental procedures described elsewhere,[17] which

is a biphasic Co/Zn-ZIF-new series, i.e., a series containing both a Zn-rich phase and a Co-rich phase. The two series of crystals were structurally characterized through powder X-ray diffraction (PXRD), scanning electron microscopy (SEM), as well as energy-dispersive X-ray spectroscopy (EDX), and chemically via $^{1}$H solution nuclear magnetic resonance (S-NMR). The Co/Zn-ZIF-62 series showed structural features similar to those known in the literature, whereas the Co/Zn-ZIF-new series featured both a different crystal structure and an unexpected molecular structure of the organic ligands. The Co/Zn-ZIF-new series was also analyzed via infrared spectroscopy (FT-IR) and inductively coupled plasma optical emission spectroscopy (ICP-OES) to investigate the nature of its structure. Both series were analyzed via differential scanning calorimetry (DSC) to investigate how $T_m$ and $T_g$ vary with the substitution of Co for Zn. In this work, we also conducted DFT and classical force field (FF) calculations on the crystalline phase of the bimetallic ZIF-62 systems, in order to predict the change in mechanical properties of the crystals, and how bond lengths and bond strength increase when substituting cobalt for zinc.

## 4.3. EXPERIMENTAL

### 4.3.1. SYNTHESIS OF ZIF CRYSTALS

Standard Co/Zn ZIF-62 synthesis. Solvothermal synthesis of Co/Zn-ZIF-62 was carried out in accordance with Table 1 and based on a method reported by Henke et al.[18] For brevity, the samples are named according to the reaction fraction of cobalt, e.g., a reaction batch of $Zn_{0.9}Co_{0.1}$-ZIF-62 is called 0.1-ZIF-62. The stock solutions for synthesis contain 0.14 M zinc nitrate hexahydrate ($Zn(NO_3)_2{\cdot}6H_2O$), 0.14 M cobalt nitrate hexahydrate ($Co(NO_3)_2{\cdot}6H_2O$), 0.40 M imidazole ($C_3H_4N_2$, Im), 0.06 M benzimidazole ($C_7H_6N_2$, bIm), and N,N-dimethylformamide (DMF). The volume of each reactant for each sample is given in Table 1. The solutions were mixed by stirring for 30 minutes, and then they were transferred to a 100 mL Teflon-lined steel autoclave and placed in an oven at 130 °C for 168 hours. The oven was turned off, and the autoclaves were cooled under ambient pressure overnight to room temperature. The crystals were collected from the autoclave and washed three times with DMF. The samples were centrifuged at 4500 rpm for 5 minutes between each wash. After the last wash, the samples were dried overnight at 110 °C.

**Table 1** Volume concentration of the stock solutions used to synthesize bimetallic ZIF-62 samples

| Sample | 0.14 M $Zn(NO_3)_2 \cdot 6H_2O$ (mL) | 0.14 M $Co(NO_3)_2 \cdot 6H_2O$ (mL) | 0.40 M Im (mL) | 0.06 M bIm (mL) |
|---|---|---|---|---|
| 0.0-ZIF-62 | 25 | — | 25 | 25 |
| 0.1-ZIF-62 | 22.5 | 2.5 | 25 | 25 |
| 0.2-ZIF-62 | 20 | 5 | 25 | 25 |
| 0.4-ZIF-62 | 15 | 10 | 25 | 25 |
| 0.6-ZIF-62 | 10 | 15 | 25 | 25 |
| 0.8-ZIF-62 | 5 | 20 | 25 | 25 |
| 0.9-ZIF-62 | 2.5 | 22.5 | 25 | 25 |
| 1.0-ZIF-62 | — | 25 | 25 | 25 |

Biphasic Co/Zn-ZIF-new synthesis. A different synthesis route was used to synthesize the biphasic Co/Zn-ZIF-new series. Zinc nitrate hexahydrate, cobalt nitrate hexahydrate, imidazole, benzimidazole, and DMF solvent were used, as shown in Table 2. The solutions were mixed for 30 minutes, transferred to the same type of autoclaves as used for the synthesis of Co/Zn-ZIF-62, and heated at 120 °C for 48 hours, in contrast to 130 °C and 168 hours in the standard synthesis. The recovered crystals were washed three times with DMF and centrifuged at 4500 rpm for 5 minutes between each wash, followed by drying at 110 °C overnight. These samples are also named according to the ratio of cobalt content to the total metal content, i.e., $Zn_{0.9}Co_{0.1}$-ZIF-new is called 0.1-ZIF-new, where 'new' refers to the change in structure compared to the standard ZIF-62.

**Table 2** Volume concentration of the stock solutions used for the biphasic Co/Zn-ZIF-new synthesis

| Sample | 0.6 M $Zn(NO_3)_2 \cdot 6H_2O$ (mL) | 0.6 M $Co(NO_3)_2 \cdot 6H_2O$ (mL) | 4 M Im (mL) | 0.5 M bIm (mL) | DMF (mL) |
|---|---|---|---|---|---|
| 0.0-ZIF-new | 17.45 | — | 33.82 | 21.82 | 1.91 |
| 0.1-ZIF-new | 15.71 | 1.75 | 33.82 | 21.82 | 1.91 |
| 0.2-ZIF-new | 13.96 | 3.49 | 33.82 | 21.82 | 1.91 |
| 0.4-ZIF-new | 10.47 | 6.98 | 33.82 | 21.82 | 1.91 |
| 0.6-ZIF-new | 6.98 | 10.47 | 33.82 | 21.82 | 1.91 |
| 0.8-ZIF-new | 3.49 | 13.96 | 33.82 | 21.82 | 1.91 |
| 1.0-ZIF-new | — | 17.45 | 33.82 | 21.82 | 1.91 |

### 4.3.2. STRUCTURAL ANALYSIS

A PANalytical Empyrean equipped with a Cu X-ray source ($\lambda = 1.54098$ Å) was used to collect powder X-ray diffraction (PXRD) patterns. The crystalline powders were loaded onto an amorphous silicon sample holder (PANalytical) and measured using a Ni-filter, 0.04 rad soller, 1/8° divergence slit, and 1/4° anti-scatter slit on the incident side and a 7.5 mm anti-scatter slit and a 0.04 rad soller on the diffracted side. The diffraction spectra were collected with $2\theta = [5.009583°, 79.995010°]$ using a step-size of 0.006565°. The samples were dried at 350 °C in an argon atmosphere before the measurements.

Solution $^{1}$H-NMR (Bruker Avance III 600 MHz spectrometer) was used to determine the composition of organic linkers in each crystalline sample. All samples were digested using 200 μL of a 1 : 5 DCl (35% conc., 99% 2H, Aldrich) : dimethyl sulfoxide (DMSO) (VWR, 99.80% 2H) solution. The pulse sequence used was a 1D experiment with composite pulses.[38] A 5 seconds continuous-wave irradiation of $\gamma B_1/2\pi = 50$ Hz was used to suppress the water signal. The total recycle delay was 28 s. A Zeiss 1540 XB was used to conduct both scanning electron microscopy (SEM) and energy-dispersive X-ray spectroscopy (EDX) to characterise the crystalline samples. EDX data acquisition and analysis were carried out, using the NSS3 X-ray microanalysis software (Thermo Fischer Scientific Inc.). The accelerating voltage of the electron beam is 10 kV. Fourier-transform infrared spectroscopy (FT-IR) measurements were performed on Co/Zn-ZIF-new samples in a wavenumber range 4000–400 $cm^{-1}$ in absorbance mode using Bruker Tensor II equipped with platinum attenuated total reflectance (ATR).

### 4.3.3. THERMAL ANALYSIS

The melting, glass transition, and mass change of the samples were studied using a Netzsch STA 449 F1 instrument that combines differential scanning calorimetry (DSC) and thermal gravimetric analysis (TGA). The samples were placed in a platinum crucible situated on a sample holder of the STA at room temperature. The samples were held for 5 min at an initial temperature of 343 K, then heated at 10 K $min^{-1}$ to 733 K, and then cooled back to 393 K at 10 K $min^{-1}$, thus forming the standard glass. Subsequently, the second upscan was conducted from 393 K to 643 K at 10 K $min^{-1}$. To determine the isobaric heat capacity of the samples, both the baseline (blank) and the reference sample (sapphire) were measured.

In order to identify the decomposition gases, additional TGA were performed using a Jupiter 449 simultaneous thermal analysis (STA) instrument coupled with a 403 C Aëolos mass spectrometer (MS) (Netzch, Selb, Germany). The measurements were performed with a heating rate of 10 K $min^{-1}$ in an argon atmosphere. A small amount of powder (11–14 mg) was inserted into an uncovered alumina crucible. The ionised species of the gases released from the heat-treated sample were detected by the MS and compared to the gas ionic spectra data from the NIST Standard Reference Database.[39]

### 4.3.4. SIMULATIONS OF ZIF-62 BASED SAMPLES

The atomic configuration for crystalline Zn-ZIF-62 was obtained from the Cambridge Structural Database (CSD, CCDC number 671070). The original structure does not contain cobalt atoms. To create $Zn_{(1-x)}Co_x$-ZIF-62, an increasing number of zinc atoms were substituted by cobalt atoms. Because the distance between the nodes (zinc and cobalt atoms) in ZIF-62 is relatively large (>6 Å) with direct substitution of zinc atoms with cobalt atoms, the interaction between the cobalt sites can be ignored. Both the DFT calculation and the force field calculation were attempted. While the DFT calculation gives more accurate results, the force field calculation is much faster because it uses a classical force field and requires less computational resources.

For the DFT calculation, the crystal Zn-ZIF-62 structure was relaxed using the projector augmented-wave PAW method as implemented in the Vienna ab initio simulation package (VASP). An energy cut-off of 650 eV was applied for the plane-wave basis set. Perdew–Burke–Ernzerhof (PBE) functional was used to evaluate the electronic exchange and correlation with a D3 van der Waals correction by Grimme.[40] The Brillouin zone was sampled at the Γ-point, which is considered sufficient for the ZIF-62 unit cell dimension of 296 atoms. For the structural relaxation, we set the EDIFF to be $10^{-3}$–$10^{-4}$ eV. The ionic relaxation stops when all forces are converged to less than 0.005 eV $Å^{-1}$. In order to calculate the bulk modulus, the ZIF-62 structures of different Co concentrations had been relaxed with a series of volume changes from −4% to 2%. The Birch–Murnaghan equation of state[41] was used to extract the bulk modulus from the energy curve at different volumes.

In the classical FF calculations, the bimetallic $Zn_{(1-x)}Co_x$-ZIF-62 structures from the above DFT calculations are first subjected to energy minimisation using the conjugate gradient algorithm as implemented in LAMMPS41 (ref.[42]) with an energy tolerance the force tolerance of $4.3 \times 10^{-17}$ eV and $7 \times 10^{-16}$ nN, respectively, for the minimisation. For the interactions between atoms, the classical Universal Force Field for Metal–Organic Frameworks (UFF4MOF) force field[43,44] is used. UFF4MOF is based on the universal force field[45] and has been extended for MOF chemistries. UFF4MOF contains transition metals, including zinc and cobalt, which are commonly found in ZIFs. It has been shown that the UFF4MOF force field can accurately reproduce the structural characteristics and the bulk modulus for many different types of MOFs that

have been verified experimentally.[31,44,46] To calculate the bulk modulus, the ZIF-62 structure is relaxed with a series of volume changes from −3% to 3% around the equilibrium volume. The bulk modulus is obtained by fitting the equation of state using the Birch–Murnaghan equation.[41]

To calculate the Young's modulus, the ZIF-62 sample is stretched or compressed in one Cartesian direction up to ~5%, while the external pressure in the two other Cartesian directions is kept around zero. The Young's modulus at 0 K is extracted from the stress–strain curve.

## 4.4. RESULTS AND DISCUSSION

### 4.4.1. MODELLING AND CHARACTERISATION OF STANDARD CO/ZN-ZIF-62

DFT and classical FF calculations were carried out using the Zn-ZIF-62 structure as an initial configuration. Fig. 1 shows the FF results for Zn-ZIF-62, *viz*., the unit cell volume, bulk modulus, and Young's modulus. Densities of crystalline Zn-ZIF-62 phase determined from DFT and FF methods are close to the published density data[47] and the values obtained from the present experiment (Table S1). As shown in Fig. 1b, the unit cell volumes from both DFT and FF calculations differ by ~0.5%, and the volume of the cobalt substituted sample decreases up to 1% when the substitution of cobalt for zinc atoms reaches 62.5%. This decrease can be partially attributed to the shorter Co–N bond compared to Zn–N bond according to the DFT calculation by Krokidas et al.[19,48] The decrease in bond length is hypothesised to stem from the different electronic configurations of the metal ions ($3d^{10}$ for $Zn^{2+}$ and $3d^{7}$ for $Co^{2+}$). The unfilled $3d^{7}$ orbital is able to interact with electrons from the imidazolate linkers, which strengthens the interaction between cobalt and the linkers, resulting in the decrease in bond length. It has been experimentally observed that cobalt ZIFs have a smaller unit cell volume than their zinc counterparts.[49]

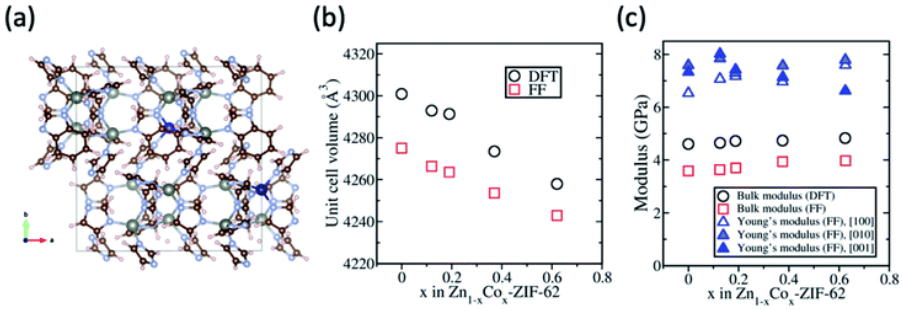


**Fig. 1** (a) Crystal structure of $Zn_{1-x}Co_x$-ZIF-62 with x = 0.125. The blue atoms are cobalt, and the large grey atoms are zinc. (b) Unit cell volume of crystalline ZIF-62 as a function of increasing substitution with cobalt. (c) Moduli of crystalline ZIF-62 as a function of increasing substitution with cobalt.

For the powder samples (see Fig. S1), the crystals are too small to measure the mechanical properties experimentally, and thus, only theoretical determination of bulk modulus and Young's modulus is reported here to show the effect of substitution of cobalt for zinc on the Zn-ZIF-62 structure. The bulk and uniaxial Young's moduli of the crystalline ZIF-62 are shown in Fig. 1c DFT and FF calculations yield an average bulk modulus of 3.8 ± 0.2 GPa and 4.7 ± 0.2 GPa for all samples. With increasing cobalt content, there is a moderate increase in the bulk modulus. The Young's modulus has a different trend with increasing substitution, depending on the crystal orientation, i.e., it increases in the [100] direction, decreases in the [001] direction, and remains roughly the same in the [010] direction. The finding that the unit cell volume decreases with increasing cobalt content agrees well with the finding of bulk modulus slightly increasing, as it has been found previously in the literature that the bond length is inversely proportional to the bulk modulus.[50,51]

The computational results predict that both zinc and cobalt ions are compatible with the ZIF-62 crystal structure. The random substitution of zinc ions with cobalt ions in the cag topology does not negatively impact the calculated mechanical strength of the crystal. Characterisation of the synthesized crystals was performed to confirm that there is no change in the space group, while the bond strength increases slightly, when substituting cobalt for zinc in ZIF-62.

An image of the eight standard Co/Zn-ZIF-62 samples can be seen in Fig. S1, revealing a color gradient as cobalt is substituted for zinc. The color gradient agrees with the relative cobalt content, as revealed by UV-Vis in Fig. S2. Fig. 2a presents the XRD patterns of the bimetallic Co/Zn-ZIF-62 crystals synthesized by the standard approach.[18]The patterns of all Co/Zn-ZIF-62 samples agree well with the reference crystallographic information files (CIF) (Cambridge Crystallographic Data Centre (CCDC)[52] (ZIF-62: CCDC number 671070)) used to generate the XRD patterns. The decrease in the signal-to-noise ratio for the samples containing predominantly cobalt

is due to the fluorescence caused by cobalt having its X-ray absorption edge close to the energy level of Cu-radiation.[53] Fig. 2b and c confirm that the benzimidazole to imidazole ratio does not change noticeably when substituting cobalt for zinc in the Co/Zn-ZIF-62 samples. Thus, we can infer that the changes in both the mechanical properties (Fig. 1) and the thermal behaviours (shown below) are a consequence of metal substitution. Additionally, SEM and EDX reveal that cobalt is evenly distributed in the crystal of all the Co/Zn-ZIF-62 samples, as seen in Fig. S3–S10. The shape of the crystals deviates from the octahedral morphology reported in the literature.[8] This deviation can be explained by the removal of DMF from the pores during heat-treatment at 350 °C.

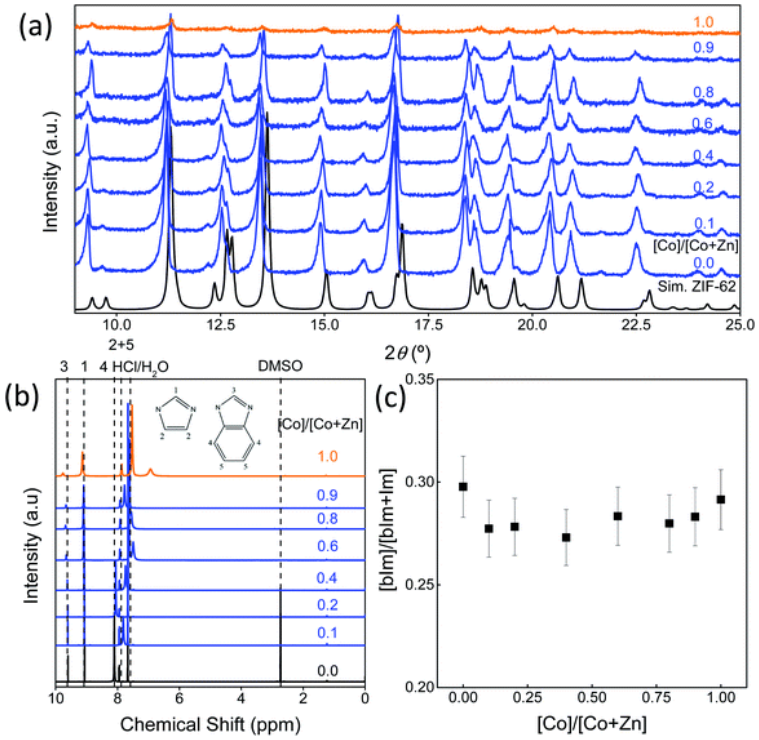


**Fig. 2** (a) XRD patterns of the standard ZIF-62 series with varying the ratio of cobalt content to the total metal content ([Co]/([Co + Zn])). (b) Liquid $^{1}$H-NMR spectra of Co/Zn-ZIF-62 samples. Dashed lines: the typical peaks associated with imidazole, benzimidazole, and solvents. (c) Fraction of benzimidazole content in the total linker content for each cobalt modified ZIF-62, with a margin of error of 5%.

The structural characterisation of the standard series agrees well with the computational results, suggesting that zinc and cobalt ions can co-exist in the same bimetallic crystal structure without phase separation. Based on the computational results shown

earlier, as well as previous experimental results for Co-ZIF-62,[18] it is expected that $T_m$ would linearly increase as cobalt is substituted for zinc in the ZIF-62 crystal structure due to stronger bonding between the cobalt nodes and the linkers. Fig. 3a and b show the thermal responses of the Co/Zn-ZIF-62 samples for the first and second upscans, respectively. The first upscan curve reveals two distinct endothermic responses. The first is attributed to the removal of DMF from the pores, while the second is ascribed to the melting process, with $T_m$ defined as the offset of the melting peak. The second upscan curves in Fig. 3b for all the Co/Zn-ZIF-62 samples show clear glass transition peaks, strongly confirming the glassy nature of melt-quenched samples. Fig. 3c displays the $T_m$ of the standard Co/Zn-ZIF-62 structures, which agrees well with that of the as-synthesized crystals in Henke group's work.[18] $T_m$ is seen to anomalously decrease as cobalt is introduced (0.1-ZIF-62), and then non-linearly increases with a gradual substitution of cobalt for zinc. This effect is rather unexpected, when looking at the simulation work of Fig. 1b and c. Fig. 3d demonstrates that $T_g$ also has a similar drop, followed by an increase as the degree of cobalt substitution increases. Fig. 3c and d shows that both $T_m$ and $T_g$ follow a similar trend when substituting cobalt for zinc. $T_m$ drops slightly from 707 K to 700 K and then non-linearly increases to a maximum of 712 K, slightly higher than reported previously. Similarly, $T_g$ has a small drop from 599 K to 591 K and then increases to 597 K when all zinc nodes are substituted with cobalt. For the standard Co/Zn-ZIF-62 series, there is only one homogeneous crystalline phase, and the minima of both $T_m$ and $T_g$ are found at the composition of Co/(Co + Zn) = ∼0.1. The observed minimum in $T_m$ could be a consequence of the mixed metal node effect that has the same fashion as the mixed modifier effect in oxide glasses.[54,55] The mixed modifier effect in oxide glasses refers to a non-additive change of some transport properties when one type of modifier (e.g., sodium ion) is substituted by another (e.g., potassium), i.e., a positive or negative deviation from the linear trend of a property with the modifier substitution. [54,55] In the studied standard Co/Zn-ZIF-62, the partial substitution of cobalt for zinc (and vice versa) causes an increase in structural instability, possibly due to structural mismatch effects caused by the difference in bond length and strength between Co–N and Zn–N bonds. This bond difference arises from the difference in electron configurations between the two types of metal ions ($d^7$ for $Co^{2+}$ and $d^{10}$ for $Zn^{2+}$). The structural instability enhances the atomic vibrations, and hence, the Lindemann criterion for melting would be more easily fulfilled.[56] However, the pure Co-ZIF-62 exhibits higher $T_m$ than its counterpart – pure Zn-ZIF-62. The higher $T_m$ of pure Co-ZIF-62 can be attributed to the stronger interaction between the linkers and cobalt ions, as predicted from the DFT and FF calculations, and also from the experimental data reported by other authors.[18]

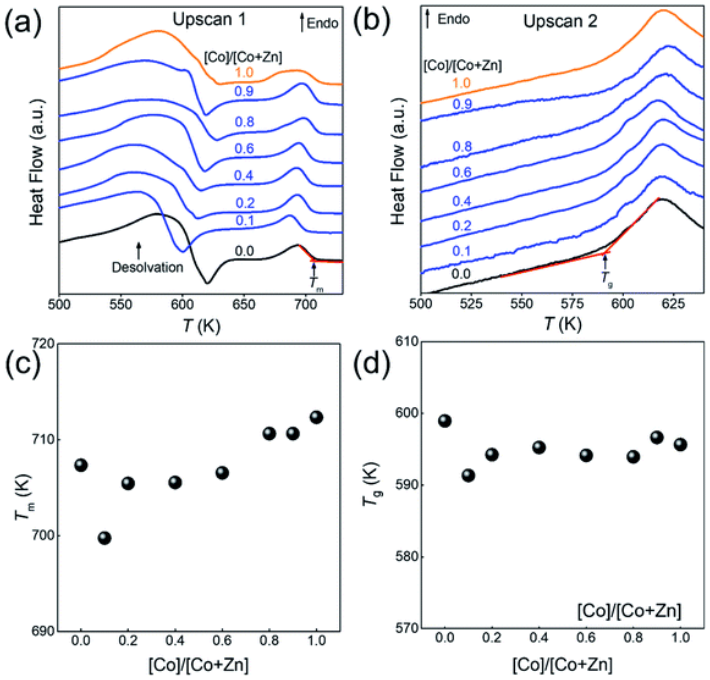


**Fig. 3** (a) The first upscan (10 K $min^{-1}$) shows two endothermic peaks, assigned to desolvation followed by melting. (b) Glass transition behaviour during the second upscan (10 K $min^{-1}$). (c) $T_m$ of Co/Zn-ZIF-62 with increasing substitution with cobalt. (d) $T_g$ of Co/Zn-ZIF-62 with increasing substitution with cobalt. Inset: $T_g/T_m$ ratio for the same series.

### 4.4.2. IMPACT OF SYNTHESIS CONDITION ON CO/ZN-ZIF-62 STRUCTURE

Fig. S11 shows the optical image of the seven ZIF samples. A clear relationship is seen between the intensity of the purple color of the sample and the amount of cobalt added during the synthesis. These samples were analyzed via X-ray diffraction to identify the crystal structure (Fig. S12). When sufficient cobalt nitrate is used in the solvothermal synthesis, an additional phase is observed for the resulting crystals, with the peaks marked with asterisks (*). In Fig. 4a, the diffraction pattern of 1.0-ZIF-new is compared to that of 1.0-ZIF-62. A different XRD pattern is observed, confirming that 1.0-ZIF-new has a different structure from the standard 1.0-ZIF-62. This new type of ZIF crystal shows fewer peaks in the XRD pattern than the standard 1.0-ZIF-62. This suggests that the new structure is likely of higher symmetry than that of the standard sample, as fewer peaks (i.e., fewer unique d-spacings) are present. The absence of diffraction peaks at higher angles suggests that the structure is indeed a Co-based metal-organic framework. It is assumed that the formation of this structure is a result of the high reactant concentrations used during the solvothermal synthesis.

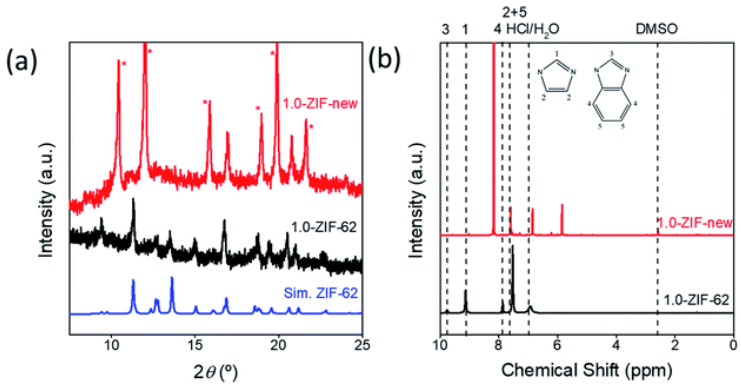


**Fig. 4** (a) X-ray diffraction pattern of simulated ZIF-62 (blue), 1.0-ZIF-62 (black), and 1.0-ZIF-new. (*) highlights the new peaks emerging from the new ZIF structure. (b) $^{1}$H-NMR of 1.0-ZIF-62 (black) and 1.0-ZIF-new (red). The 1.0-ZIF-new sample clearly shows the disappearance of the hydrogen peaks marked as 1 and 3, while two new peaks appear.

S-NMR spectroscopy was employed to verify the presence of the organic linkers in the biphasic frameworks and the differences in linker composition between 1.0-ZIF-62 and 1.0-ZIF-new (Fig. 4b). Fig. S13 plots the NMR spectra, where the signals of 0.0-ZIF-new agree with those of the standard 0.0-ZIF-62 spectra. However, as cobalt nitrate is substituted for zinc nitrate during the synthesis, the imidazole and benzimidazole signals decrease in intensity for the resulting crystals. Two new peaks at ~5.84 and 6.83 ppm (Fig. 4b) appear and increase in intensity with increasing the cobalt

nitrate content. It was assumed that the high concentration of nitrate ions in the presence of cobalt would catalyze the nitration of imidazole to 4-nitroimidazole. The NMR spectrum of 4-nitroimidazole, dissolved in the same NMR solvent, can be found in the ESI (Fig. S14). The spectrum shows no peaks in the 5–7 ppm range, thus excluding the possibility that the emerging signal arises from nitrated imidazole. To determine the distribution of zinc and cobalt in the two crystal phases, SEM and EDX analyses were performed on the 0.6-ZIF-new sample, as seen in Fig. 5. Two crystal particles with different morphologies are observed, i.e., octahedral and spherical shapes in column 1 of Fig. 5. The SEM image in Fig. S15a shows the sample containing only Zn, i.e., 0.0-ZIF-new, which contains crushed ZIF-62 particles, where some of the flat surfaces of the standard ZIF-62 morphology remain. The SEM image in Fig. S15b illustrates the sample containing only Co, i.e., 1.0-ZIF-new, where only spherical particles are present. The SEM images indicate that there is a difference in the crystal morphologies between the standard ZIF-62 structure (i.e., the standard phase) and the new structure (i.e., the new phase). The EDX elemental mapping in Fig. 5 (see columns 2 and 3) reveals that both morphologies contain zinc and cobalt, which confirms that both metal nodes are incorporated into the two crystal structures. EDX elemental analysis in Fig. S16 confirms that the octahedral ZIF-62 crystals contain zinc predominantly, while the new spherical crystal structure contains more cobalt. The metallic heterogeneity in the new series of ZIFs could be ascribed to the preferential incorporation of cobalt into the new phase.

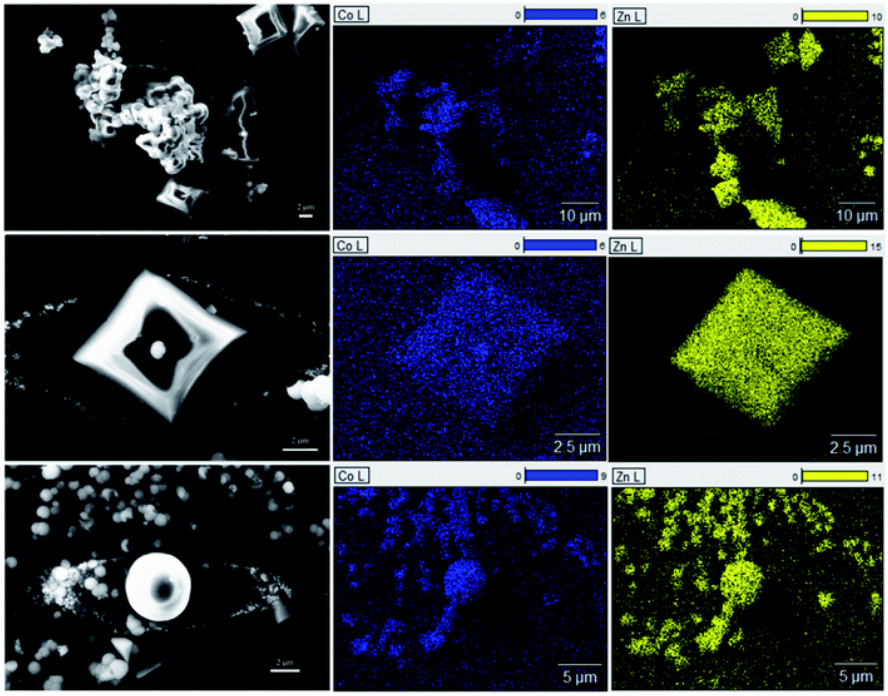


**Fig. 5** Left column is the SEM image of the area detected for EDX elemental mapping for cobalt (middle column) and zinc (right column).

ATR FT-IR was employed to detect the changes of the chemical bonds in the Co/ZIF-new samples (Fig. S17). Several changes in the signal can be observed. First, the peaks at 1677 and 1384 $cm^{-1}$, which are assigned to the DMF,[18,57,58] disappear with increasing the cobalt content, being attributed to the new phase with a denser structure. Second, some of the peaks around 1150–1300 $cm^{-1}$ (assigned to C–N and C–C stretching) change in shape as cobalt is substituted for zinc. Simultaneously, the double peak at ~1480 $cm^{-1}$, which is assigned to aromatic ring stretching, varies in line shape with increasing the cobalt content. The FT-IR results (Fig. S17) indicate that signals corresponding to imidazole and benzimidazole rings are still present. In combination with the S-NMR findings in Fig. S13, it is evident that the imidazole and benzimidazole structures have changed, while the exact chemical structure of the linkers remains unknown. It is reasonable to infer that the formation of the unknown linker is caused by cobalt nitrate, and hence, cobalt preferentially stays in the new phase. The absolute Co/(Co + Zn) ratio of these samples was analysed via ICP-OES. Fig. S18 reveals that there is a non-linear relationship between the Co/(Co + Zn) ratio used during the synthesis and the ratio detected in the resulting ZIF samples. This is explained by the phase separation exhibited in Fig. S19, where a portion of the new phase with higher cobalt content could have been lost during the washing and collecting process.

Fig. 6a and b shows the changes of both $T_m$ and $T_g$ values with the substitution of cobalt for zinc for two series of ZIFs. The data points are acquired from the first and second DSC scans shown in Fig. 3a, b and S20. It is seen in Fig. 6a and b that both $T_m$ and $T_g$ show negative deviations from linearity with substitution of cobalt for zinc, which could be caused by two factors. The first is the mixed metal node effect as the two crystal phases both contain zinc-ions and cobalt-ions. The second is a eutectic effect caused by the presence of two discrete phases resulting in a drop in $T_m$. Given that 0.1-ZIF-new in Fig. S12 reveals no detectable quantity of the new phase, the mixed metal effect is likely to have a greater effect at lower Co/(Co + Zn) ratios on $T_m$ and $T_g$. The deviations in both $T_m$ and $T_g$ are much larger for the new ZIF series than that of Co/Zn-ZIF-62. Due to the absence of the new phase at low cobalt content, it is reasonable to infer that the effect on $T_m$ and $T_g$ is initially driven by the mixed metal node effect, but at higher cobalt concentrations, multiple effects e.g., the effect of two discrete phases could cause the changing trend in $T_m$ and $T_g$. These results imply that the atomic vibration in the new series of ZIF more easily meets Lindemann's criterion for melting. Moreover, it is seen in Fig. S21 that the Co/Zn-ZIF-new series undergoes a noticeable loss of mass during the melting process. The origin of the mass loss is investigated by a thermogravimetric analyzer coupled with mass spectrometry (TGA-MS) (Fig. S22). The TGA-MS analysis shows that mainly $NH_3$ and NO gases are released during melting, suggesting that the linkers in the new series are more unstable than those in the standard series. The 0.0-ZIF-new sample has a $T_m$ at 706 K and a $T_g$ at 588 K, which correspond to the values for standard Zn-ZIF-62. 1.0-ZIF-new has a higher $T_m$ at 724 K and a lower $T_g$ at 573 K. The higher $T_m$ might be due to a denser structure, as indicated by the lack of DMF signals from the FT-IR results.

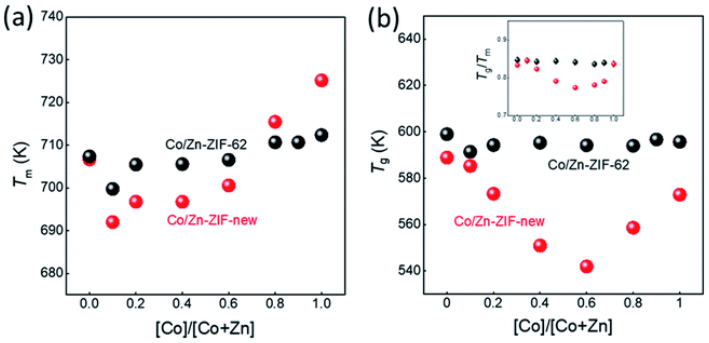


**Fig. 6** (a) $T_m$ of Co/Zn-ZIF-62 series (black) and Co/Zn-ZIF-new series (red). (b) $T_g$ of Co/Zn-ZIF-62 series (black) and Co/Zn-ZIF-new series (red). Inset: $T_g/T_m$ ratios for both Co/Zn-ZIF-62 series and Co/Zn-ZIF-new series.

The inset of Fig. 6b shows the dependence of $T_g/T_m$ ratios for the two studied ZIF series on the Co–Zn substitution. As is known, $T_g/T_m$ is a measure of the glass forming ability (GFA) of a glass former, i.e., the higher the $T_g/T_m$ ratio of a glass former is, the higher its GFA is. It is seen that both series show higher GFA since their $T_g/T_m$ ratios (0.77–0.84) are significantly higher than that of most good glass formers ($T_g/T_m$ = 0.67).[12] Interestingly, there is no change in $T_g/T_m$ with metal node substitution in the standard series, indicating that the GFA remains the same. However, in contrast to the standard series, the new series exhibits smaller $T_g/T_m$ ratios, suggesting that the GFA of the latter is relatively lower. In addition, the $T_g/T_m$ ratio shows a non-monotonic trend with substituting cobalt for zinc, i.e., there is a minimum $T_g/T_m$ ratio at Co/(Co + Zn) = 0.6. This composition shows a pronounced phase separation, as shown in Fig. 5. This fact agrees with the general notion that a glass former with stronger phase separation tendency features a lower GFA.

## 4.5. CONCLUSIONS

We synthesized two series of bimetallic cobalt/zinc zeolitic imidazolate frameworks based on ZIF-62. It was found that the structure of the derived ZIF crystals strongly depended on synthesis conditions. One series of ZIF crystals were obtained by using the standard synthesis condition reported in the literature, which possessed the standard ZIF-62 structure. In contrast, the other series, which was produced at a lower temperature (120 °C) for a shorter duration (48 hours), had a mixed structure composed of both the standard structure and a new one. We predicted the mechanical properties of the standard series of Zn/Co-ZIF-62 through DFT and FF calculations.

An interesting mixed metal node effect was observed in bimetallic ZIF-62 samples, i.e., negative deviations from linearity of $T_m$ and $T_g$ for both series of bimetallic ZIF-62 with substitution of Co for Zn. Notably, the new series displayed a stronger mixed metal node effect at lower Co substitution. This mixed metal node effect was attributed to the structural mismatch between $Co^{2+}$ and $Zn^{2+}$, and to the difference in their electronic configurations. The network became destabilised by introducing the dissimilar cobalt-ion into the ZIF crystal. Some of the samples in the new series contained both cobalt-rich and zinc-rich phases, whereas the standard one showed only one homogeneous phase. It was found that during melting, the Co/Zn-ZIF-new samples underwent a partial decomposition of an unknown species, suggesting that the new phase had a lower thermal stability than the standard phase. The above findings are instrumental to the understanding of the structure and thermodynamic properties of MOF glasses and to the design of novel MOF glass formers. Concerning the strong mixed metal node effect of the Co/Zn-ZIF-new series, the chemistry and structure of this series should be further investigated to reveal the melting mechanism of MOFs and to design new MOF glass formers.

Both series of ZIFs have higher GFA due to their higher $T_g/T_m$ ratios (0.77–0.84) compared to most of the good glass formers. $T_g/T_m$ remains the same with metal node substitution in the standard series, and hence there is no change in GFA. However, the new series exhibits smaller $T_g/T_m$ ratios, i.e., lower GFA, than the standard series. In addition, the new series shows a minimum $T_g/T_m$ ratio at Co/(Co + Zn) = 0.6.

## 4.6. CONFLICTS OF INTEREST

The authors declare no competing financial interest.

## 4.7. ACKNOWLEDGEMENTS

The authors thank Villum Fonden (grant no. 13253) for the support. A. Q. acknowledges the National Natural Science Foundation of China (no. 22175135) and the Fundamental Research Funds for the Central Universities (WUT: 2021IVA099, 2021III018JC) for their support. Y. Y. thank the Independent Research Fund Denmark for the support (1026-00318B).

## 4.8. REFERENCES

1 K. S. Park, Z. Ni, A. P. Côté, J. Y. Choi, R. Huang, F. J. Uribe-Romo, H. K. Chae, M. O'Keeffe and O. M. Yaghi, Proc Natl Acad Sci U S A, 2006, 103, 10186–10191.

2 T. D. Bennett and S. Horike, Nat Rev Mater, 2018, 3, 431–440.

3 B. Chen, Z. Yang, Y. Zhu and Y. Xia, J Mater Chem A Mater, 2014, 2, 16811–16831.

4 B. R. Pimentel, A. Parulkar, E. K. Zhou, N. A. Brunelli and R. P. Lively, ChemSusChem, 2014, 7, 3202–3240.

5 H. Furukawa, K. E. Cordova, M. O'Keeffe and O. M. Yaghi, Science (2013), 341, DOI:10.1126/science.1230444.

6 M. Safaei, M. M. Foroughi, N. Ebrahimpoor, S. Jahani, A. Omidi and M. Khatami, TrAC - Trends in Analytical Chemistry, 2019, 118, 401–425.

7 M. I. Nandasiri, S. R. Jambovane, B. P. McGrail, H. T. Schaef and S. K. Nune, Coord Chem Rev, 2016, 311, 38–52.

8 Y. Wang, H. Jin, Q. Ma, K. Mo, H. Mao, A. Feldhoff, X. Cao, Y. Li, F. Pan and Z. Jiang, Angewandte Chemie - International Edition, 2020, 51, 4365–4369.

9 A. Kertik, L. H. Wee, K. Sentosun, J. A. R. Navarro, S. Bals, J. A. Martens and I. F. J. Vankelecom, ACS Appl Mater Interfaces, 2020, 12, 2952–2961.

10 H. T. Kwon and H. K. Jeong, J Am Chem Soc, 2013, 135, 10763–10768.

11 T. D. Bennett, J. C. Tan, Y. Yue, E. Baxter, C. Ducati, N. J. Terrill, H. H. M. Yeung, Z. Zhou, W. Chen, S. Henke, A. K. Cheetham and G. N. Greaves, Nat Commun, 2015, 6, 1–7.

12 A. Qiao, T. D. Bennett, H. Tao, A. Krajnc, G. Mali, C. M. Doherty, A. W. Thornton, J. C. Mauro, G. N. Greaves and Y. Yue, Sci Adv, 2018, 4, DOI:10.1126/sciadv.aao6827.

13 C. Zhou, L. Longley, A. Krajnc, G. J. Smales, A. Qiao, I. Erucar, C. M. Doherty, A. W. Thornton, A. J. Hill, C. W. Ashling, O. T. Qazvini, S. J. Lee, P. A. Chater, N. J. Terrill, A. J. Smith, Y. Yue, G. Mali, D. A. Keen, S. G. Telfer and T. D. Bennett, Nat Commun, 2018, 9, 1–9.

14 R. S. K. Madsen, A. Qiao, J. Sen, I. Hung, K. Chen, Z. Gan, S. Sen and Y. Yue, Science (1979), 2020, 367, 1473–1476.

15 A. Qiao, H. Tao, M. P. Carson, S. W. Aldrich, L. M. Thirion, T. D. Bennett, J. C. Mauro and Y. Yue, Opt Lett, 2019, 44, 1623.

16 T. To, S. S. Sørensen, M. Stepniewska, A. Qiao, L. R. Jensen, M. Bauchy, Y. Yue and M. M. Smedskjaer, Nat Commun, 2020, 11, 1–9.

17 M. Stepniewska, K. Januchta, C. Zhou, A. Qiao, M. M. Smedskjaer and Y. Yue, PNAS, 2020, DOI:10.1073/pnas.2000916117.

18 L. Frentzel-Beyme, M. Kloß, R. Pallach, S. Salamon, H. Moldenhauer, J. Landers, H. Wende, J. Debus and S. Henke, J Mater Chem A Mater, 2019, 7, 985–990.

19 P. Krokidas, S. Moncho, E. N. Brothers, M. Castier and I. G. Economou, Physical Chemistry Chemical Physics, 2018, 20, 4879–4892.

20 R. R. Kuruppathparambil, R. Babu, H. M. Jeong, G. Y. Hwang, G. S. Jeong, M. il Kim, D. W. Kim and D. W. Park, Green Chemistry, 2016, 18, 6349–6356.

21 G. Kaur, R. K. Rai, D. Tyagi, X. Yao, P. Z. Li, X. C. Yang, Y. Zhao, Q. Xu and S. K. Singh, J Mater Chem A Mater, 2016, 4, 14932–14938.

22 A. M. Bumstead, M. F. Thorne and T. D. Bennett, Faraday Discuss, 2021, 225, 210–225.

23 Mohamed. A. Ali, J. Ren, T. Zhao, X. Liu, Y. Hua, Y. Yue and J. Qiu, ACS Omega, 2019, 4, 12081–12087.

24 F.-X. Coudert and A. H. Fuchs, Coord Chem Rev, 2016, 307, 211–236.

25 R. B. Getman, Y.-S. Bae, C. E. Wilmer and R. Q. Snurr, Chem Rev, 2011, 112, 703–723.

26 J. C. Tan, B. Civalleri, C. C. Lin, L. Valenzano, R. Galvelis, P. F. Chen, T. D. Bennett, C. Mellot-Draznieks, C. M. Zicovich-Wilson and A. K. Cheetham, Phys Rev Lett, 2012, 108, 095502.

27 A. U. Ortiz, A. Boutin, A. H. Fuchs and F.-X. Coudert, Phys Rev Lett, 2012, 109, 195502.

28 J. C. Tan, T. D. Bennett and A. K. Cheetham, Proc Natl Acad Sci U S A, 2010, 107, 9938–9943.
29 A. M. Walker, B. Civalleri, B. Slater, C. Mellot-Draznieks, F. Corà, C. M. Zicovich-Wilson, G. Román-Pérez, J. M. Soler and J. D. Gale, Angewandte Chemie International Edition, 2010, 49, 7501–7503.
30 M. Gao, A. J. Misquitta, L. H. Rimmer and M. T. Dove, Dalton Transactions, 2016, 45, 4289–4302.
31 P. G. Boyd, S. M. Moosavi, M. Witman and B. Smit, J Phys Chem Lett, 2017, 8, 357–363.
32 R. Gaillac, P. Pullumbi, K. A. Beyer, K. Chapman, D. A. Keen, T. D. Bennett and F. X. Coudert, Nat Mater, 2017, 16, 1149–1155.
33 L. Zhang, Z. Hu and J. Jiang, J Am Chem Soc, 2013, 135, 3722–3728.
34 Z. Hu, Y. Chen and J. Jiang, J Chem Phys, 2011, 134, 134705.
35 Y. Yang, Y. K. Shin, S. Li, T. D. Bennett, A. C. van Duin and J. C. Mauro, J Phys Chem B, 2018, 122, 9616–9624.
36 Y. Yang, C. J. Wilkinson, K. H. Lee, K. Doss, T. D. Bennett, Y. K. Shin, A. C. T. van Duin and J. C. Mauro, Journal of Physical Chemistry Letters, 2018, 9, 6985–6990.
37 D. Dubbeldam, K. S. Walton, D. E. Ellis and R. Q. Snurr, Angewandte Chemie - International Edition, 2007, 46, 4496–4499.
38 A. Bax, Journal of Magnetic Resonance (1969), 1985, 65, 142–145.
39 P. J. Linstrom and W. G. Mallard, NIST Chemistry WebBook National Institute of Standards and Technology, Gaithersburg MD.
40 S. Grimme, J. Antony, S. Ehrlich and H. Krieg, Journal of Chemical Physics, 2010, 132, DOI:10.1063/1.3382344.
41 F. Birch, Physical review, 1947, 71, 809.
42 S. Plimpton, J Comput Phys, 1995, 117, 1–19.
43 M. A. Addicoat, N. Vankova, I. F. Akter and T. Heine, J Chem Theory Comput, 2014, 10, 880–891.
44 D. E. Coupry, M. A. Addicoat and T. Heine, J Chem Theory Comput, 2016, 12, 5215–5225.
45 A. K. Rappé, C. J. Casewit, K. Colwell, W. Goddard Iii and W. Skiff, J Am Chem Soc, 1992, 114, 10024–10035.
46 L. Vanduyfhuys, S. Vandenbrande, J. Wieme, M. Waroquier, T. Verstraelen and V. van Speybroeck, J Comput Chem, 2018, 39, 999–1011.
47 T. D. Bennett, Y. Yue, P. Li, A. Qiao, H. Tao, N. G. Greaves, T. Richards, G. I. Lampronti, S. A. T. Redfern, B. Frédéric, O. K. Farha, J. T. Hupp, A. K. Cheetham and D. A. Keen, J Am Chem Soc, 2016, 138, 3484–3492.
48 P. Krokidas, M. Castier, S. Moncho, E. Brothers and I. G. Economou, The Journal of Physical Chemistry C, 2015, 119, 27028–27037.

49 S. Henke, M. T. Wharmby, G. Kieslich, I. Hante, A. Schneemann, Y. Wu, D. Daisenberger and A. K. Cheetham, Chem Sci, 2018, 9, 1654–1660.

50 K. Li, Z. Ding and D. Xue, Functional Materials Letters, 2010, 3, 241–244.

51 I. D. Brown, P. Klages and A. Skowron, Acta Crystallogr B, 2003, 59, 439–448.

52 P. Z. Moghadam, A. Li, S. B. Wiggin, A. Tao, A. G. P. Maloney, P. A. Wood, S. C. Ward and D. Fairen-jimenez, , DOI:10.1021/acs.chemmater.7b00441.

53 L. Chen, T. Mashimo, C. Iwamoto, H. Okudera, E. Omurzak, H. S. Ganapathy, H. Ihara, J. Zhang, Z. Abdullaeva, S. Takebe and A. Yoshiasa, Nanotechnology, 2013, 24, DOI:10.1088/0957-4484/24/4/045602.

54 J. Kjeldsen, M. M. Smedskjaer, J. C. Mauro and Y. Yue, J Non Cryst Solids, 2014, 406, 22–26.

55 J. Kjeldsen, M. M. Smedskjaer, J. C. Mauro and Y. Yue, Appl Phys Lett, 2014, 104, 051913.

56 F. A. Lindemann, "The calculation of molecular vibration frequencies," *Physik. Z*, vol. 11, pp. 609–612, 1910.

57 D. Radhakrishnan and C. Narayana, Journal of Chemical Physics, 2015, 143, DOI:10.1063/1.4937763.

58 G. Khandelwal, N. P. Maria Joseph Raj and S. J. Kim, J Mater Chem A Mater, 2020, 8, 17817–17825.


## 4.9. SUPPORTING INFORMATION

**Mixed metallic node effect in zeolitic imidazolate frameworks**

**Table S1.** Densities (g/cm$^3$) of Zn-ZIF-62 from experiments and density functional theory (DFT) and classical force field (FF) calculations. The solvent content was taken from the literature[1] and added to the density calculation for the DFT and FF results.

| | Zn-ZIF-62 crystal |
|---|---|
| Exp.[59] | 1.494 |
| Current Exp. | 1.467 |
| DFT (PBE-D3) | 1.537 |
| FF | 1.546 |


**Fig. S1.** Image of Co/Zn-ZIF-62 samples (from the left 0.0, 0.1, 0.2, 0.4, 0.6, 0.8, 0.9, 1.0) revealing the change in the intensity of the purple colour with increasing cobalt content.

**UV-VIS Absorption analysis of Co/Zn-ZIF-62**

UV-VIS was carried out to verify that the intensity of purple colour of the bimetallic ZIF-62 crystals correlates with the cobalt content. Calibration curve was used by dissolving 0.0482 grams of 1.0-ZIF-62 using 10 mL 1 M HCl. The solution was used for a full UV-VIS absorption spectrum using a Varian Cary 50 Bio UV-Visible Spectrophotometer. The result showed a peak absorption at 510 nm (green), which has red as its complimentary colour. The solution was then diluted, using 1 M HCl with the following solution:HCl ratios: 9:1, 8:2, 7:3, and 6:4. The samples were then measured on a thermo spectronic helios epsilon spectrophotometer at 510 nm to measure the absorption. The data was used to make a calibration curve, using a linear fit with $R^2$ = 0.999. For each Co and Zn-containing ZIF-62 sample, a weighed amount was dissolved, using 1 M HCl and their absorption were measured at 510 nm. A theoretical absorption for a pure Co-ZIF-62 was calculated for each sample to reveal the [Co]/[Co+Zn] rat io.Fig S2. displays the observed relative Co content against the fraction of Co used in the synthesis. The figure displays a fairly good agreement between synthesis condition and the content of cobalt in the sample.

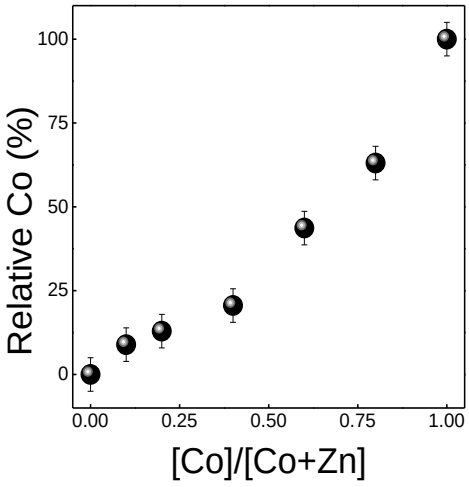


**Fig S2**. Observed cobalt content plotted against the ratio used during synthesis of Co/Zn-ZIF-62.

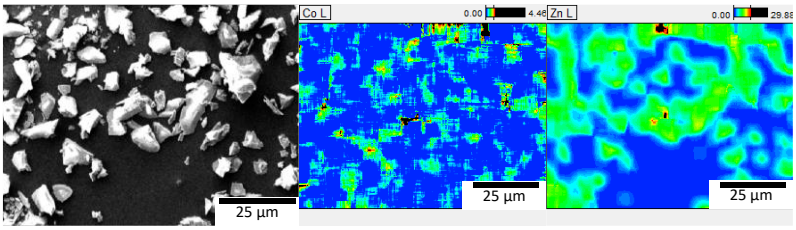


***Fig S3.*** *SEM image (left) of the area detected by EDX for 0.0-ZIF-62 sample, and the EDX elemental mapping for the cobalt (middle column) and zinc (right column), using a contoured color gradient.*

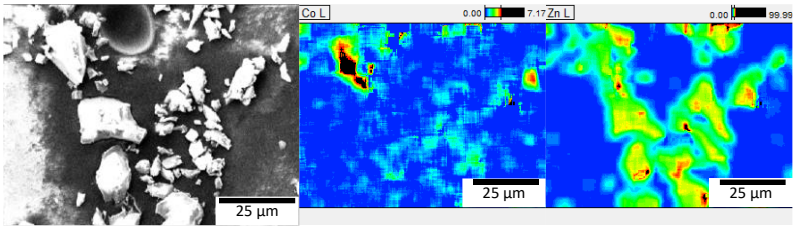


***Fig. S4.*** *SEM image (left) of the area detected by EDX for 0.1-ZIF-62 sample, and the EDX elemental mapping for the cobalt (middle column) and zinc (right column), using a contoured color gradient.*

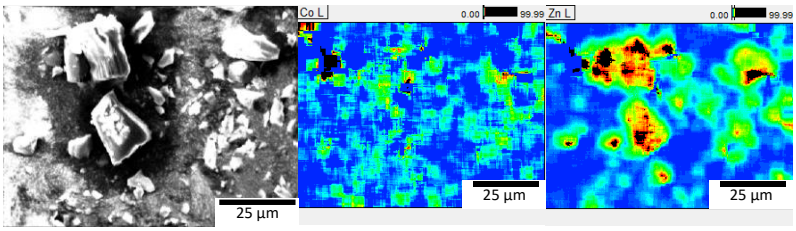


***Fig. S5.*** *SEM image (left) of the area detected by EDX for 0.2-ZIF-62 sample, and the EDX elemental mapping for the cobalt (middle column) and zinc (right column), using a contoured color gradient.*

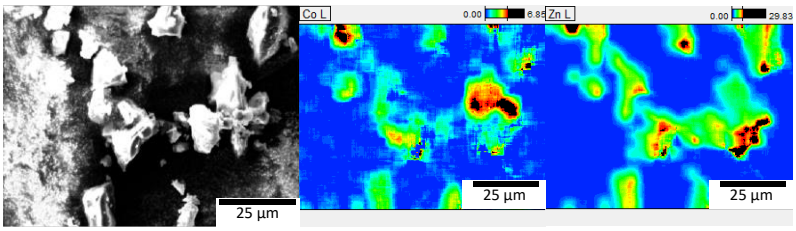


***Fig. S6.*** *SEM image (left) of the area detected by EDX for 0.4-ZIF-62 sample, and the EDX elemental mapping for the cobalt (middle column) and zinc (right column), using a contoured color gradient.*

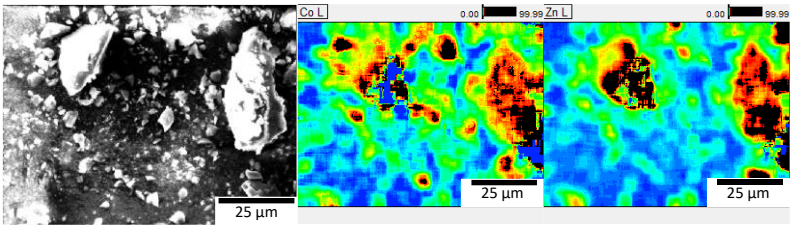


***Fig. S7.*** *SEM image (left) of the area detected by EDX for 0.6-ZIF-62 sample, and the EDX elemental mapping for the cobalt (middle column) and zinc (right column), using a contoured color gradient.*

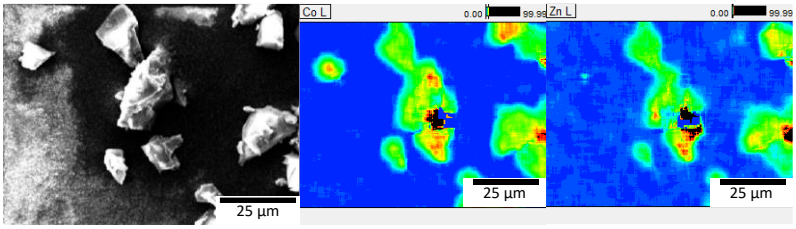


***Fig. S8.*** *SEM image (left) of the area detected by EDX for 0.8-ZIF-62 sample, and the EDX elemental mapping for the cobalt (middle column) and zinc (right column), using a contoured color gradient.*

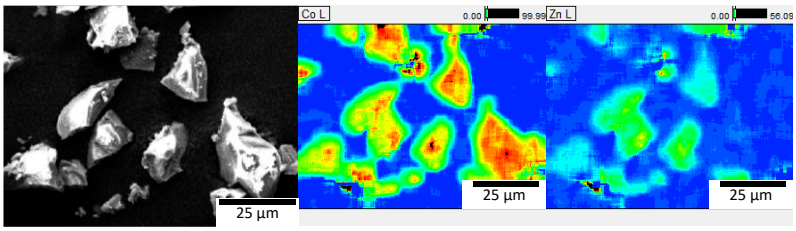


***Fig. S9.*** *SEM image (left) of the area detected by EDX for 0.9-ZIF-62 sample, and the EDX elemental mapping for the cobalt (middle column) and zinc (right column), using a contoured color gradient.*

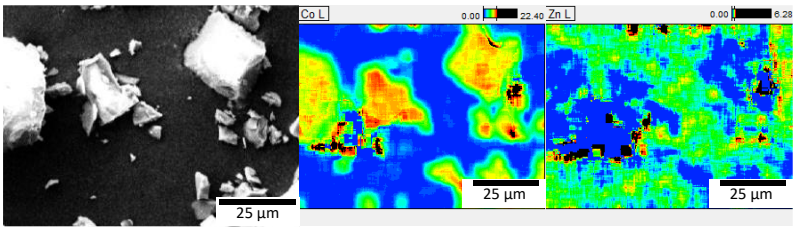


***Fig. S10.*** *SEM image (left) of the area detected by EDX for 1.0-ZIF-62 sample, and the EDX elemental mapping for the cobalt (middle column) and zinc (right column), using a contoured color gradient.*

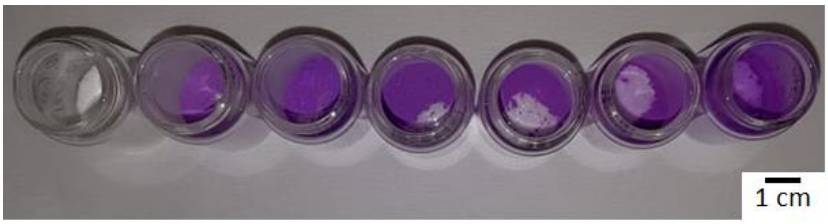


***Fig. S11.*** *Image of Co/Zn-ZIF-new samples (from the left 0.0, 0.1, 0.2, 0.4, 0.6, 0.8, 1.0), revealing the change in the intensity of the purple colour with increasing cobalt content.*

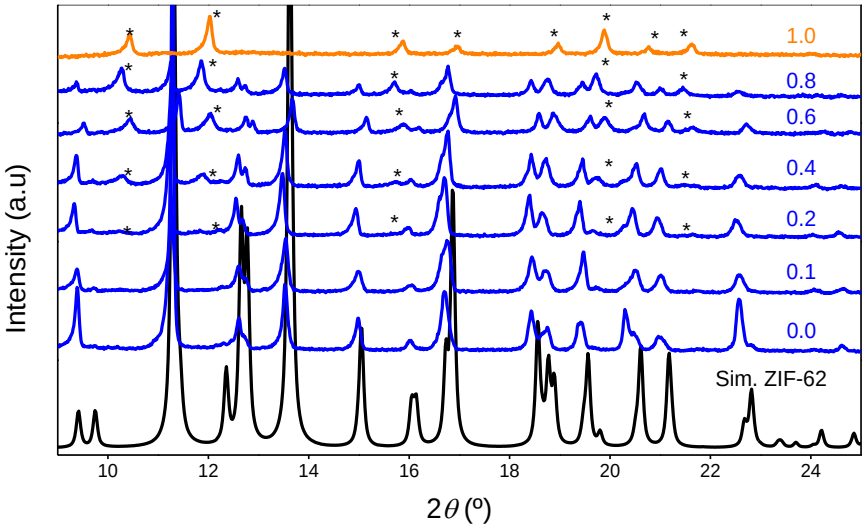


***Fig. S12****. X-ray diffraction patterns of Co/Zn-ZIF-new, showing the emergence of a new crystalline phase, as Co substitutes for Zn. Emerging new peaks are designated with *.*

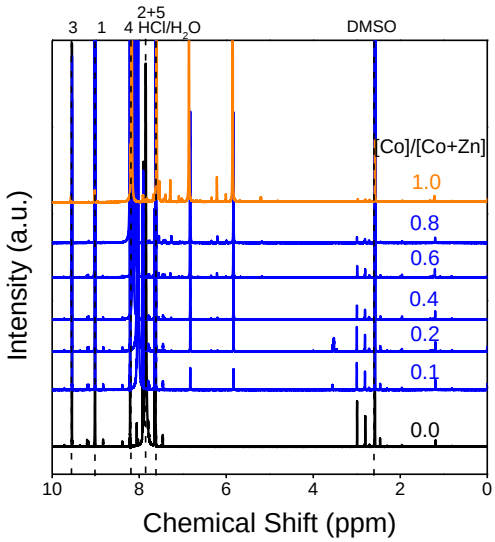


***Fig. S13.*** *Liquid $^{1}$H-NMR spectra of Co/Zn-ZIF-new samples. The emergence of two new peaks as cobalt substitutes for zinc reveals the formation of a new organic linker during the synthesis.*

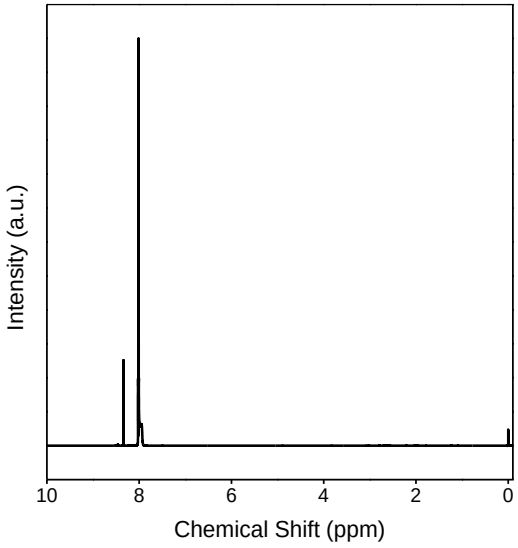


***Fig. S14.*** *Liquid $^{1}$H-NMR spectrum of 4-nitroimidazole purchased from Sigma Aldrich (97%).*

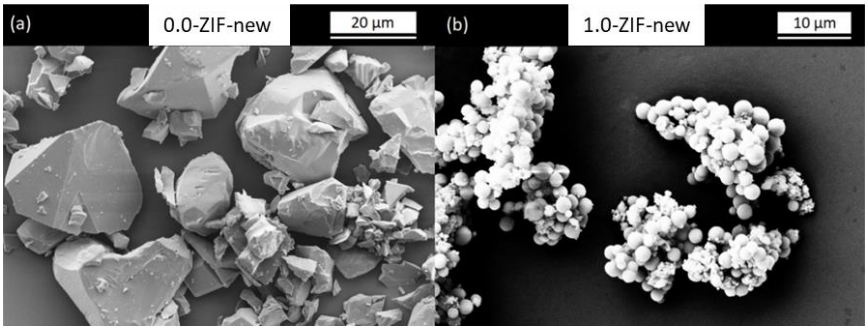


***Fig. S15***. *SEM images of crystalline ZIF-new samples. (a) 0.0-ZIF-new. (b) 1.0-ZIF-new*

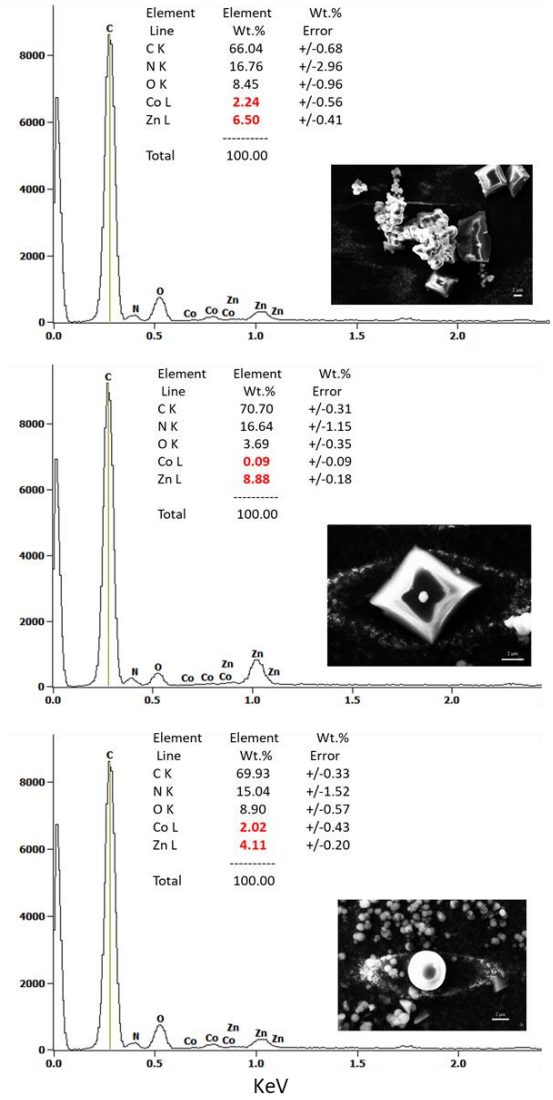


***Fig. S16***. *EDX elemental analysis of different particles belonging to the 0.6-ZIF-new sample, showing chemical heterogeneity in the sample.*

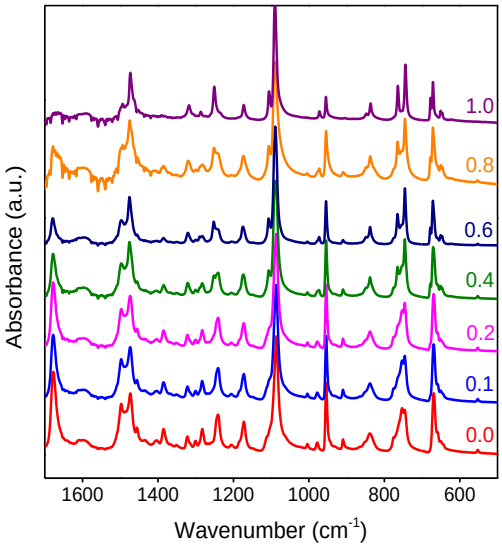


***Figure S17.*** *ATR FT-IR spectrum of Co/Zn-ZIF-new samples.*

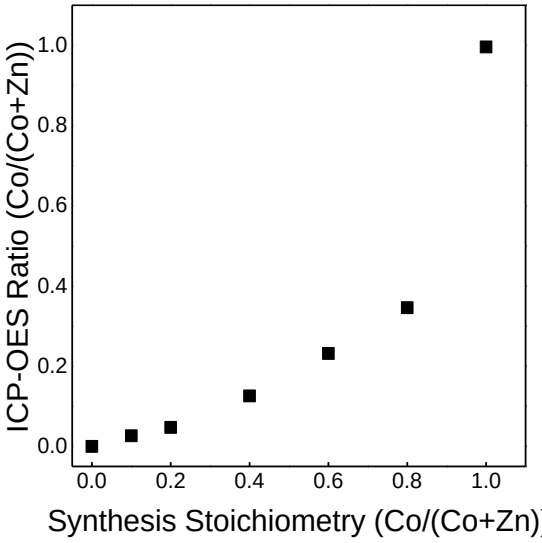


**Fig. S18.** Measured Co/(Co+Zn) ratio vs. synthesis stoichiometry for Co/Zn-ZIF-new samples. Inductively coupled plasma – optical emission spectroscopy (ICP-OES) (Prodigy 7, Teledyne Leeman Labs) analysis was used to quantify the zinc to cobalt ratio. The standard calibration solutions used contains 1 µg $mL^{-1}$ Zn, Ni Cr and 0.5 µg $mL^{-1}$ Ba, Mn, Cu in 3% $HNO_3$ (National Institute of Metrology, China). Sample solutions were prepared by dissolving a precisely weighed amount of ZIF sample into 2 mL of an $HNO_3$ solution. The primary solutions were transferred to 50 mL volumetric flasks readied for measurements. For quantitative analysis of Zn and Co, the wavelengths 206.200 nm and 228.615 nm were used, respectively.


***Fig. S19.*** *Image of 0.4-ZIF-new, revealing a rich purple phase and a lighter phase being separated during the drying process.*

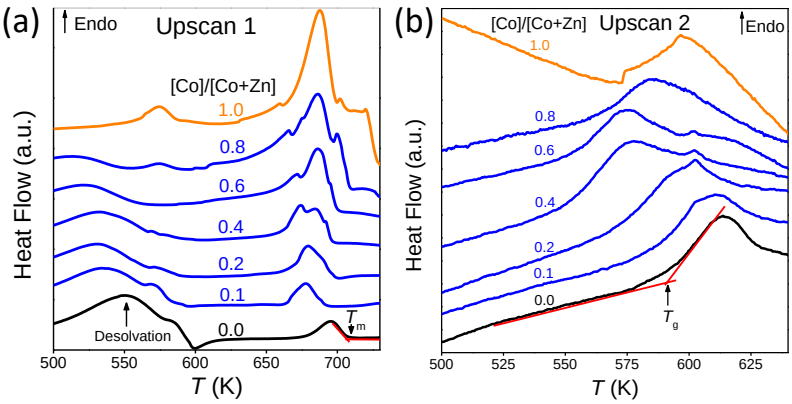


***Fig. S20***. *DSC analysis of Co/Zn-ZIF-new. (a) first upscan (heating rate of 10 K min$^{-1}$) revealing the endothermic solvent release and melting point and partial decomposition. (b) second upscan (10 K min$^{-1}$) revealing the glass transition peak onset.*

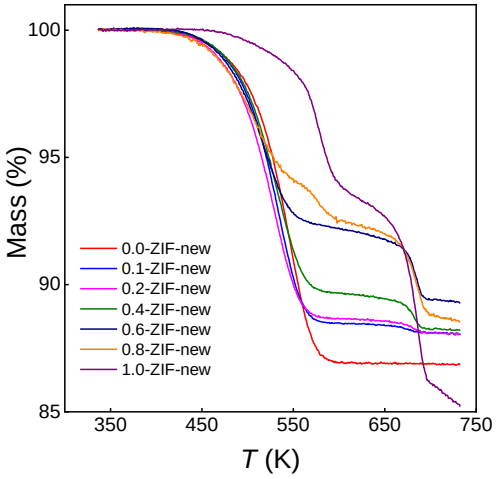


***Figure S21.*** *TGA data of synthesized Co/Zn-ZIF-new crystals during the first upscan.*

## Biphasic Decomposition Gas Analysis

Thermal gravimetric analyses (TGA) were performed using a Jupiter 449 simultaneous thermal analysis instrument (Netzch, Selb, Germany) coupled with a 403C Aëoloss mass spectrometer (MS), with a heating rate of 10 °C $min^{-1}$ in an argon atmosphere. The ionized species of the gases released from the heat-treated sample were detected by the MS. The MS data were compared to the gas ionic spectra of the relevant gases from the NIST Standard Reference Database[2]. The gases we identified based on the m/z numbers and their relative intensity. The signals from MS are not quantitative.

The mass loss for the sample 0.0-ZIF-new is related to the release of $N_2$ and/or CO (m/z=28), $H_2O$ (m/z=18), NO (m/z=30), DMF (m/z=73, 44, 42, 29), and $NH_3$ (m/z=17, 16). The ionic spectra for the first mass loss of the sample 1.0-ZIF-new indicate release of $H_2O$, $N_2$ and/or CO, NO, and $NH_3$, while the spectra for the second mass at >370 °C indicate release of $NH_3$, NO, and small amounts of $CH_4$ (m/z=15) and $CO_2$. These data show that the organic constituents (e.g., DMF) in great part degrade to smaller molecules (e.g., $N_2$, NO, $NH_3$) when leaving the analyzed sample.

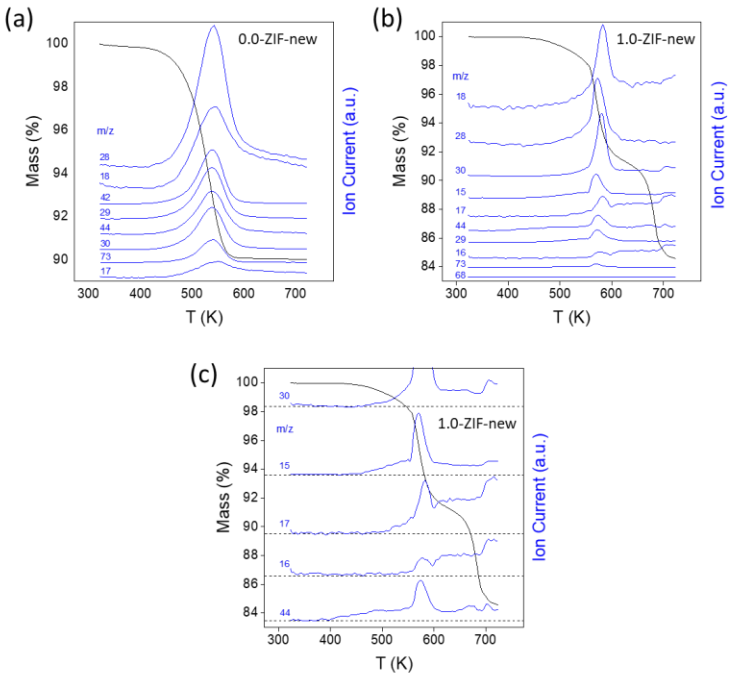


**Fig. S22.** DTA-MS spectra of the samples (a) 0.0-ZIF-new and (b,c) sample 1.0-ZIF-new. (c) focuses on the second mass at >370 °C and shows the ionic signals of the gases that remain high above their baselines (thin dotted lines).

## References


1 T. D. Bennett, Y. Yue, P. Li, A. Qiao, H. Tao, N. G. Greaves, T. Richards, G. I. Lampronti, S. A. T. Redfern, F. Blanc, O. K. Farha, J. T. Hupp, A. K. Cheetham and D. A. Keen, Journal of the American Chemical Society, 2016, 138, 3484–3492.

2 P. J. Linstrom and W. G. Mallard, NIST Chemistry WebBook National Institute of Standards and Technology, Gaithersburg MD.

# 5. ULTRAHIGH-FIELD $^{67}$ZN NMR REVEALS SHORT-RANGE DISORDER IN ZEOLITIC IMIDAZOLATE FRAMEWORK GLASSES

This chapter is the scientific paper titled “Ultrahigh-field 67Zn NMR reveals short-range disorder in zeolitic imidazolate framework glasses” (DOI: 10.1126/science.aaz0251) published in Science volume 367, issue 6485, 2020, page 1473-1476 (17). Both the main article and supplementary information have been included in this chapter. Note that the paper is written as a standalone text. This means that the figure, table references and citations do not adhere to the citation format of the thesis, however, the citations have been added to the bibliography of the thesis. The conceptual idea of this publication is ascribed to Yuanzheng Yue and Sabyasachi Sen, while synthesis, calorimetric work, and initial writing were carried out by the author of this thesis.

Chapters 3 and 4 dealt with the effects of long-range as well as local structural characteristics and their effect on the melting and glass-formation mechanism in ZIFs. The findings pointed towards the metal-nitrogen coordination bond is paramount for the melting of ZIFs. This paper focuses on the $^{67}$Zn solid-state nuclear magnetic resonance spectroscopy study of crystalline ZIF glass-formers and their vitrified state. The quadrupolar $^{67}$Zn-isotope offers the ability to gain insight into the spatial order surrounding the Zn atoms, through the quadrupolar coupling constant and the asymmetry parameter. The major finding of this work is that the NMR data of the crystalline materials can be described well with two subequal Zn sites, as in accordance with the two crystallographic sites in ZIF-4, ZIF-zni and ZIF-62 crystals. However, glass-formation causes the peaks to collapse to singular broad peaks described by a continuous distribution of coupling constants. This proves that the coordination environment around the Zn sites gets significantly distorted, and is thus the first experimental proof of short-range disorder consistent with the bond breaking and reforming mechanism described by Coudert (114).

**Acknowledgement:** Reproduced from Science with permission from the Science AAAS. Link to the original paper: https://www.science.org/doi/full/10.1126/science.aaz0251

**Citations used exclusively in published papers (first appearance):** (162–167)

# ULTRAHIGH-FIELD $^{67}$ZN NMR REVEALS SHORT-RANGE DISORDER IN ZEOLITIC IMIDAZOLATE FRAMEWORK GLASSES

Rasmus S. K. Madsen, Ang Qiao, Jishnu Sen, Ivan Hung, Kuizhi Chen, Zhehong Gan, Sabyasachi Sen and Yuanzheng Yue

Authors Info & Affiliations

Science 27 Mar 2020 Vol 367, Issue 6485 pp. 1473-1476 DOI: 10.1126/science.aaz0251

## ABSTRACT

The structure of melt-quenched zeolitic imidazole framework (ZIF) glasses can provide insights into their glass-formation mechanism. We directly detected short-range disorder in ZIF glasses using ultrahigh-field zinc-67 solid-state nuclear magnetic resonance spectroscopy. Two distinct Zn sites characteristic of the parent crystals transformed upon melting into a single tetrahedral site with a broad distribution of structural parameters. Moreover, the ligand chemistry in ZIFs appeared to have no controlling effect on the short-range disorder, although the former affected their phase-transition behavior. These findings reveal structure-property relations and could help design metal-organic framework glasses.

Glasses can be obtained through a variety of synthesis and processing routes (*1*, *2*), but rapid cooling of the liquids remains the predominant approach. Melt-quenched (MQ) glasses can be broadly classified as inorganic, organic, and metallic and containing ionic-covalent, covalent, and metallic bonds, respectively. Recently, a fourth family of MQ glasses based on metal-organic frameworks (MOFs) have been reported that have coordination bonds (*3*–*7*). The MQ-MOF glasses are primarily represented by the subset of MOFs called the zeolitic imidazolate frameworks (ZIFs). Their extended tetrahedral network is analogous to silica and zeolites (*8*): Metal ion nodes (such as $Zn^{2+}$ and $Co^{2+}$) substitute for silicon, and imidazole ($C_3N_2H_3$)–based ligands substitute for oxygen as the bridging unit. A number of ZIF glasses have porosity, which has potential applications in gas capture and storage, and ZIF-62 glass exhibits high transparency and broad mid-infrared luminescence, which have potential photonic applications (*7*, *9*–*13*).

Recent studies have found ZIF-4 ($Zn[Im]_2$) and ZIF-62 ($Zn[Im_{2-x}bIm_x]$)—where Im and bIm are imidazole and benzimidazole, respectively—to be rather stable against crystallization during heat treatment, and that the parent liquids have a higher glass-

forming ability compared with most of the network glass-forming liquids (*14*, *15*). The glass-forming ability of ZIF-62 is greater than that of ZIF-4 because its mixed linkers, consisting of imidazole and benzimidazole in some tetrahedra, create greater steric hindrance (*14*). Previous studies explored the structural origin of this high glass-forming ability in both ZIF systems using systematic heat treatments, differential scanning calorimetry (DSC), and x-ray pair distribution function (PDF) analyses (*3*, *14*, *15*). The PDF analyses provided no clear evidence of the appearance of any medium- or long-range order in these glasses after a calorimetric scan, despite the appearance of an exothermic peak immediately before melting (*15*). The enthalpy release was attributed to the densification of the structural network, but the nature and the length scale of the structural changes associated with the decrease of the potential energy remain unclear to date. In addition, although ZIF-4 is chemically simpler than ZIF-62, the former exhibits several features in its temperature-induced phase transitions, including the transition from a low-density amorphous phase (LDA) to a high-density amorphous phase (HDA), as well as the formation and melting of ZIF-zni (which is denser than ZIF-4).

The origin of these multiple transitions remains elusive given the limitations of the analytical techniques available for determining short- and intermediate-range structure in glasses. Raman spectroscopy, $^{13}C/^{1}H$ nuclear magnetic resonance (NMR) spectroscopy, along with x-ray PDFs have been used in the past to study the short-range and medium-range structure of ZIF glasses. Although these studies provided some structural information, no substantial structural difference in the short-range order between the ZIF crystals and corresponding glasses could be identified (*14*). Previous studies showed that the organic ligands in ZIFs remained intact during melt-quenching, implying that the chemical integrity was retained after glass formation (*3*, *5*, *14*). Molecular dynamics simulations indicated that upon melting, the imidazolate-based linkers dissociate and reassociate with Zn ions through the scission and renewal of Zn–N coordination bonds (*14*, *16*). The Zn[ligand]$_4$ tetrahedral units remain intact in the ZIF glass state after the melt is quenched, and long-range structural disorder is believed to be primarily induced by the distortion of the Zn[ligand]$_4$ intertetrahedral connections (*14*, *16*).

By contrast, the short-range structural order at the scale of the Zn[ligand]$_4$ tetrahedra in MOF glasses remains unknown. Because $^{67}Zn$ is a quadrupolar nuclide, its NMR spectra can provide not only the information on the chemical shift that is characteristic of the tetrahedral environment of Zn in the ZIFs but also on the electric-field gradient (EFG) at the site of this nuclide in the structure, as encoded in its quadrupolar coupling constant $C_Q$ and asymmetry parameter $\eta_Q$. The EFG is a second-rank tensor quantity sensitive to the degree of positional and orientational order at length scales corresponding to the nearest and next-nearest neighbor distances, and possibly to even longer distances (*17*).

Only a few $^{67}Zn$ NMR spectroscopic studies have been reported that analyzed crystalline structures in zinc-based compounds, including Zn-based crystalline MOFs

(*18*–*23*), because the $^{67}$Zn nuclide has a low gyromagnetic ratio, large quadrupole moment *Q*, as well as a low natural abundance (*18*). These issues, in combination with the low atomic density of MOFs, necessitated $^{67}$Zn NMR spectral data collection at ultrahigh magnetic fields that are ~20 T or higher. We report a comparative structural study of select crystalline ZIFs and their glassy counterparts derived by means of melt-quenching, using ultrahigh-field $^{67}$Zn magic-angle-spinning (MAS) NMR spectroscopy at 19.5 and 35.2 T at the National High Magnetic Field Laboratory.

The DSC traces of ZIF-4 and ZIF-62 samples (Fig. 1A) measured the temperature-driven enthalpic responses to the chemical reactions and phase transitions. During the first upscan (from 323 to 863 K), the as-synthesized ZIF-4 crystal underwent solvent release, amorphization, polymorphic transformation to ZIF-zni crystal, and last, melting. Subsequent quenching of the ZIF-zni melt resulted in the formation of a ZIF-4 glass with a glass transition temperature ($T_g$) of 570 K during the second upscan. By contrast, during upscan 1, the as-synthesized standard ZIF-62 crystal displays the enthalpy responses only to the solvent release and the subsequent melting. After melt-quenching, the second upscan of ZIF-62 glass showed a glass transition with a $T_g$ of 593 K.

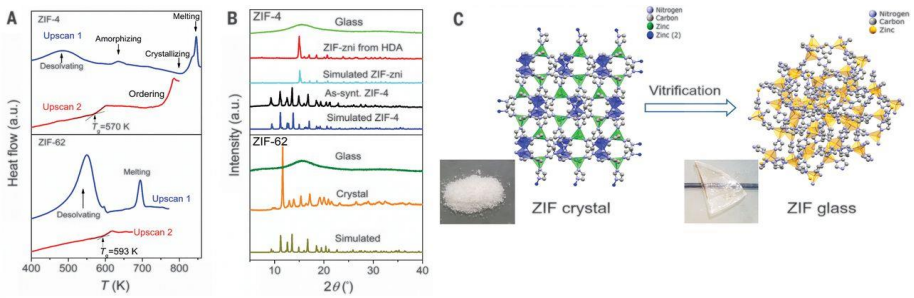


**Fig. 1 Phase transitions, glass formation, and glass transition for ZIFs.** (A) First and second DSC upscans for both (top) ZIF-4 and (bottom) ZIF-62. (B) XRD patterns of as-prepared ZIF-4 crystals, ZIF-zni crystals, ZIF-4 glass, ZIF-62 crystals, and ZIF-62 glass. (C) Schematic representation of the structural change from crystalline ZIF (powder sample) to its glassy state (transparent bulk sample) during melt-quenching.

To explore the effect of the linker chemistry (the Im/bIm ratio) on the short-range structure, we prepared a ZIF-62 crystal with a higher bIm content (denoted as ZIF-62b) (table S1). Its x-ray diffraction (XRD) patterns confirmed that ZIF-62 and ZIF-62b had the same crystalline structure (fig. S2). The final chemical compositions of ZIF-62 and ZIF-62b were $Zn(Im)_{1.75}(bIm)_{0.25}$ and $Zn(Im)_{1.68}(bIm)_{0.32}$, as determined from $^1$H liquid NMR measurements (fig. S3). Additionally, we prepared a ZIF-62b glass sample by melt-quenching, which was also subjected to two DSC scans. The increase of bIm in ZIF-62 framework led to an increase of both melting temperature ($T_m$) and $T_g$ (fig. S4), which is consistent with a previous study (*14*). The XRD patterns

of both crystal and glass samples for ZIF-4, -zni, and -62 (Fig. 1B) show the presence of long-range order in crystalline ZIFs and its absence in their glassy counterparts. The vitrification of these ZIF crystals is schematically demonstrated in Fig. 1C.

The $^{67}$Zn MAS NMR spectra of the three crystalline ZIFs (ZIF-4, ZIF-62, and ZIF-zni) were obtained at two different magnetic fields, 19.5 and 35.2 T (Fig. 2). Each of these crystals contained two crystallographically distinct Zn sites at a 1:1 ratio, one of which is a more distorted Zn[ligand]$_4$ tetrahedron (*18*). The $^{67}$Zn MAS NMR line shapes also necessitated simulation with at least two sites with subequal (within ±5%) relative fractions (Fig. 2); we used the software Dmfit (*24*). For each composition, the spectra collected at both magnetic fields were fitted simultaneously with the same set of NMR parameters: isotropic chemical shift $\delta_{iso}$, the quadrupolar coupling constant $C_Q$, and asymmetry parameter $\eta_Q$. These parameters are listed in Table 1, and the $C_Q$ values for ZIF-4 are in good agreement with those reported in a recent study (*18*).

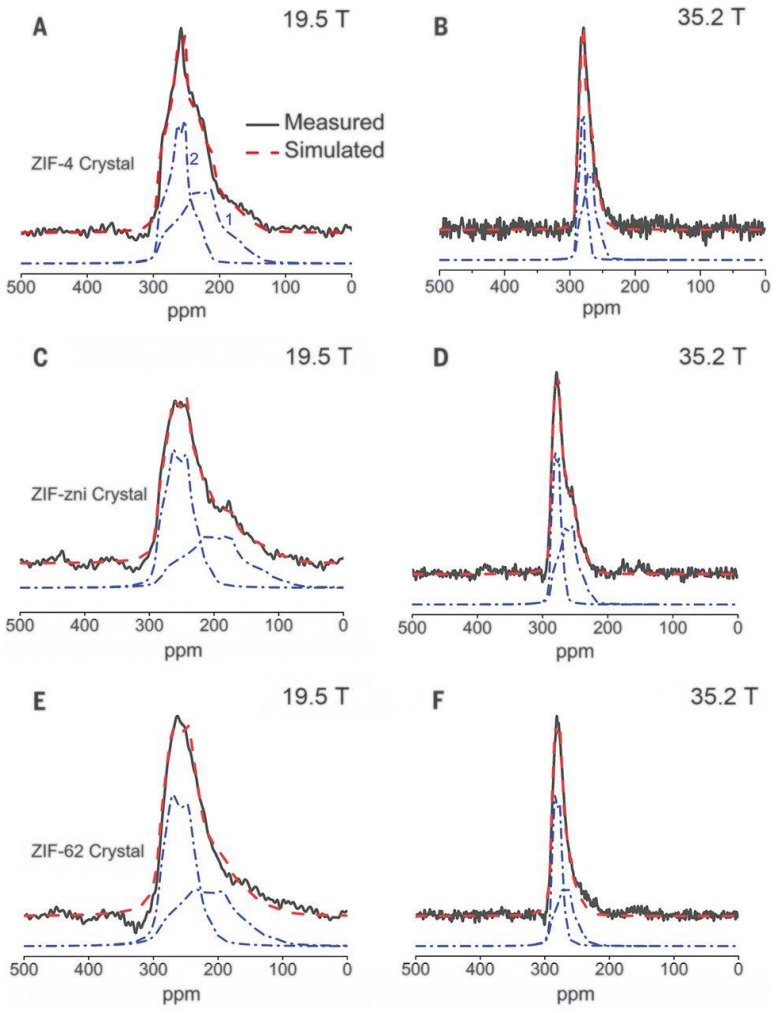


**Fig. 2 Short-range order of crystalline ZIFs.** (**A** to **F**) Experimental (solid black line) and simulated (dashed red line) $^{67}$Zn MAS NMR spectra of [(A) and (B)] crystalline ZIF-4, [(C) and (D)] ZIF-zni, and [(E) and (F)] ZIF-62 collected at 19.5 and 35.2 T. Individual simulation components (dot-dashed blue lines) are vertically offset for clarity.

**Table 1 $^{67}$Zn NMR parameters.**
$^{67}$Zn MAS NMR line shape simulation parameters for crystalline and glassy MOFs.*Lattice sites correspond to those designated in structural refinements of ZIF-4, ZIF-62, and ZIF-zni, as reported in (*8*, *28*, *29*). †These values represent the root mean square quadrupolar product $\sqrt{\langle C_{Q\eta}^2 \rangle}$.

| MOF | Lattice site* | $\delta_{iso}$ (ppm) | $C_Q$ (±0.2 MHz) | $\eta_Q$ (±0.05) | Relative fraction (±5%) |
|---|---|---|---|---|---|
| **ZIF-4 crystal** | Zn1 | 296 | 5.1 | 0.6 | 46 |
| **Zn2** | 295 | 3.7 | 0.6 | 54 | |
| **ZIF-62 crystal** | Zn1 | 297 | 5.8 | 0.5 | 48 |
| **Zn2** | 296 | 4.0 | 0.4 | 52 | |
| **ZIF-zni crystal** | Zn1 | 288 | 6.0 | 0.6 | 46 |
| **Zn2** | 290 | 4.0 | 0.5 | 54 | |
| **ZIF-4 glass** | Zn | 277 | 6.9† | N/A | 100 |
| **ZIF-62 glass** | Zn | 278 | 6.5† | N/A | 100 |
| **ZIF-62b glass** | Zn | 277 | 6.8† | N/A | 100 |

The data in Table 1 indicated that the $\delta_{iso}$ for all Zn sites in all materials varied over a rather narrow range, from ~277 to 297 parts per million (ppm). However, for each crystalline ZIF, the less distorted Zn sites (Zn2) had a smaller $C_Q$ of ~4.0 MHz compared with the more distorted ones (Zn1) characterized by a larger $C_Q$ of ~5 to 6 MHz. These assignments followed the density functional theory–based calculations by Sutrisno *et al*. (*18*). Intriguingly, in spite of having the same composition, the $^{67}$Zn $C_Q$ values of the two Zn sites in ZIF-4 crystal are substantially different from those in ZIF-zni crystal. This result may be indicative of the corresponding difference in the topology between these two crystals; ZIF-4 has a *cag* topology and the ZIF-zni has a *zni* topology (*5*). The higher $C_Q$ values of the Zn sites in the ZIF-zni crystal compared with those for the ZIF-4 crystal are also consistent with ZIF-zni possessing a greater variance in the bond angles and lengths for the Zn sites compared with ZIF-4 (tables S2 and S3).

The $^{67}$Zn MAS-NMR spectra of the ZIF-4 and ZIF-62 glasses were obtained at both 19.5 and 35.2 T (Fig. 3, A to D). These spectra had asymmetric line shapes with low-frequency tails that we attributed to a continuous distribution of $C_Q$ characteristic of structural disorder in the glassy state. These $^{67}$Zn MAS NMR line shapes were well simulated with $\delta_{iso}$ (277 to 278 ppm) similar to that observed in corresponding crystals (288 to 297 ppm) (Table 1) and with a Czjzek distribution of the $C_Q$ parameter (*25*), which yields a root-mean-square quadrupolar product $\sqrt{\langle C_{Q\eta}^2 \rangle}$ of ~6.9 MHz for the

ZIF-4 glass and ~6.5 to 6.8 MHz for the two ZIF-62 glasses. When taken together, the results in Table 1 indicate that as the ZIF crystals were melt-quenched into glass, the $C_Q$ values increased and displayed a broader distribution, indicating that the structural disorder of the Zn[ligand]$_4$ tetrahedral environment in the glassy state was higher than that in the parent crystals. The $^{67}$Zn NMR parameters for all three ZIF glasses were similar (Table 1), implying a similar degree of short-range disorder, despite their differences in the Im/bIm ratio in the ligands.

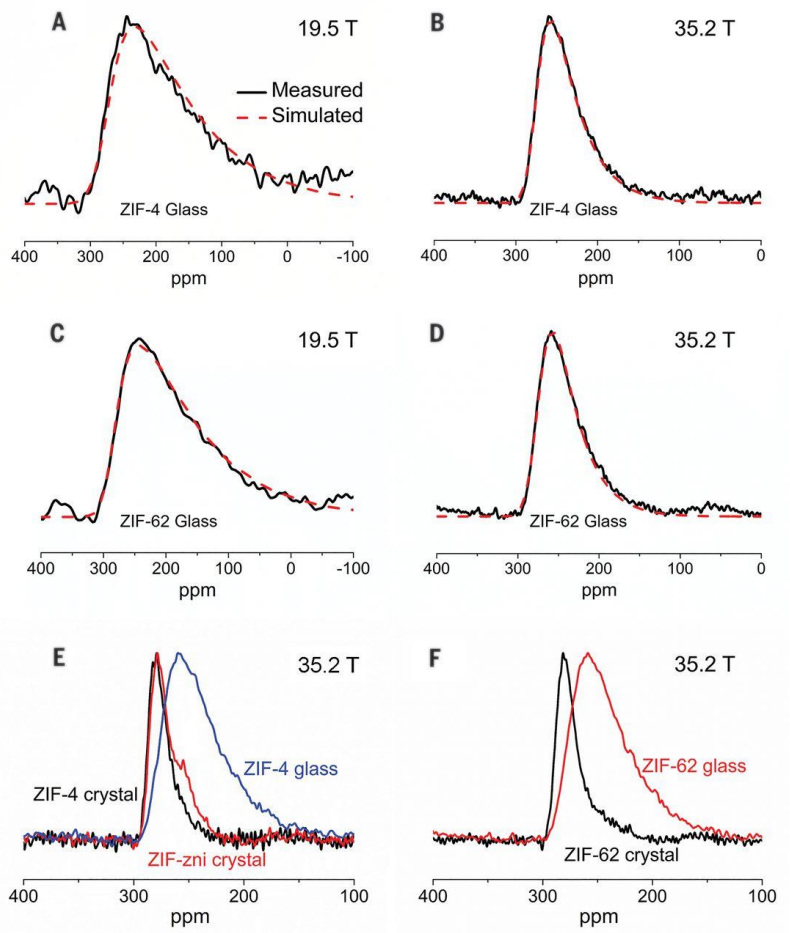


**Fig. 3 Comparison of short-range structure between ZIF glasses and crystals.** (**A** to **D**) Experimental (solid black line) and simulated (dashed red line) $^{67}$Zn MAS NMR spectra for [(A) and (B)] ZIF-4 glass and [(C) and (D)] the standard ZIF-62 glass at different magnetic fields. (**E**) Direct comparison of $^{67}$Zn MAS NMR spectra collected at 35.2 T between ZIF-4 crystal, ZIF-zni crystal, and ZIF-4 glass. (**F**) Direct comparison of spectra collected at 35.2 T of ZIF-62 crystal and glass.

The disappearance of the two distinct Zn sites characteristic of the ZIF crystals upon melting and vitrification indicates that the scission and renewal of the Zn–N bonds upon melting resulted in structural reconstruction (Fig. 1C and fig. S1). With their three-dimensional network of corner-sharing Zn[ligand]$_4$ tetrahedral units, ZIF glasses are structurally analogous to vitreous silica, but the coordination bonds in ZIF glasses were considerably weaker than the covalent-ionic bonds in silica. (26, 27). The silica glass network would be more rigid than ZIF glasses, and the local structure of the former would be more ordered than that of ZIF glasses. The bulky nature of the organic linkers in ZIF glasses could also cause steric hindrance, thus limiting the ability of the linker to return to its equilibrium position—to the ordered structural state with lower potential energy—upon melt-quenching. The comparison in NMR spectra among ZIF-4 and -zni crystals and ZIF-4 glass (Fig. 3E), and between ZIF-62 crystal and glass (Fig. 3F), shows broadening of the glasses compared with the crystals, and the resonance peaks moved to somewhat lower isotropic chemical shift from crystal to glass. Although the increased broadening corresponds to a high degree of structural disorder in glasses at the short-range scale, the lowering of the isotropic chemical shift is suggestive of a more specific change in the local coordination environment of Zn atoms upon vitrification. Previous Zn K-edge x-ray absorption fine structure and PDF measurements (5) indicated that Zn is in tetrahedral coordination with N in both glassy and crystalline ZIFs, and that the Zn–N distance did not change considerably upon vitrification. However, $^{67}$Zn solid-state NMR results of Sutrisno *et al*. (18) showed that the $^{67}$Zn NMR isotropic chemical shift of ZIF-14 (260 ppm) with longer Zn–N distances (2.00 to 2.02 Å) was significantly lower than that of ZIF-8 or ZIF-4 (300 to 315 ppm) characterized by shorter Zn–N distances (1.98 to 1.99 Å). Although further systematic studies are needed to establish this trend, the lower $^{67}$Zn NMR isotropic chemical shift of ZIF glasses compared with their crystalline counterparts as observed in the present study could be an indication of an increase in the average Zn–N distance in the former, which is consistent with the corresponding increase in the molar volume upon vitrification.

**Acknowledgments**

**Funding:** The authors thank the VILLUM FONDEN (13253) and the NSFC (51802263), China, for financial support. S.S. acknowledges support from the National Science Foundation grant NSF-DMR 1855176. The National High Magnetic Field Laboratory (NHMFL) is supported by the National Science Foundation through NSF/DMR-1644779 and the state of Florida. Development of the 36-T series connected hybrid magnet and NMR instrumentation was supported by NSF (DMR-1039938 and DMR-0603042) and NIH (BTRR 1P41 GM122698). **Author contributions:** Y.Y. and S.S. conceived the project; Y.Y., S.S., R.S.K.M., and A.Q. made the outline of the project. I.H., K.C., and Z.G. performed NMR measurements at NHMFL. J.S. performed all NMR spectral data processing and simulation. A.Q., R.S.K.M., and Y.Y. synthesized the samples and conducted DSC and XRD measurements. Y.Y., S.S., R.S.M., and A.Q. wrote the manuscript, with inputs from I.H., K.C., Z.G., and J.S. **Competing interests:** The authors declare that they have no competing interests.

**Data and materials availability:** All data needed to evaluate the conclusions in the paper are present in the paper and/or the supplementary materials. Additional data related to this paper may be requested from the authors.

**References and Notes**


1 C. A. Angell, Formation of glasses from liquids and biopolymers. *Science* **267**, 1924– 1935 (1995).

2 G. N. Greaves, S. Sen, Inorganic glasses, glass-forming liquids and amorphizing solids. *Adv. Phys.* **56**, 1–166 (2007).

3 T. D. Bennett, J.-C. Tan, Y. Yue, E. Baxter, C. Ducati, N. J. Terrill, H. H.-M. Yeung, Z. Zhou, W. Chen, S. Henke, A. K. Cheetham, G. N. Greaves, Hybrid glasses from strong and fragile metal-organic framework liquids. *Nat. Commun.* **6**, 8079 (2015).

4 D. Umeyama, N. P. Funnell, M. J. Cliffe, J. A. Hill, A. L. Goodwin, Y. Hijikata, T. Itakura, T. Okubo, S. Horike, S. Kitagawa, Glass formation via structural fragmentation of a 2D coordination network. *Chem. Commun.* **51**, 12728–12731 (2015).

5 T. D. Bennett, Y. Yue, P. Li, A. Qiao, H. Tao, N. G. Greaves, T. Richards, G. I. Lampronti, S. A. T. Redfern, F. Blanc, O. K. Farha, J. T. Hupp, A. K. Cheetham, D. A. Keen, Melt-quenched glasses of metal-organic frameworks. *J. Am. Chem. Soc.* **138**, 3484–3492 (2016).

6 D. Umeyama, S. Horike, M. Inukai, T. Itakura, S. Kitagawa, Reversible solid-to-liquid phase transition of coordination polymer crystals. *J. Am. Chem. Soc.* **137**, 864–870 (2015).

7 Y. Zhao, S. Y. Lee, N. Becknell, O. M. Yaghi, C. A. Angell, Nanoporous transparent MOF glasses with accessible internal surface. *J. Am. Chem. Soc.* **138**, 10818–10821 (2016).

8 K. S. Park, Z. Ni, A. P. Côté, J. Y. Choi, R. Huang, F. J. Uribe-Romo, H. K. Chae, M. O'Keeffe, O. M. Yaghi, Exceptional chemical and thermal stability of zeolitic imidazolate frameworks. *Proc. Natl. Acad. Sci. U.S.A.* **103**, 10186–10191 (2006).

9 C. Zhou, L. Longley, A. Krajnc, G. J. Smales, A. Qiao, I. Eruçar, C. M. Doherty, A. W. Thornton, A. J. Hill, C. W. Ashling, O. T. Qazvini, S. J. Lee, P. A. Chater, N. J. Terrill, A. J. Smith, Y. Yue, G. Mali, D. A. Keen, S. G. Telfer, T. D. Bennett, Metal-organic framework glasses with permanent accessible porosity. *Nat. Commun.* **9**, 5042 (2018).

10 L. Frentzel-Beyme, M. Kloß, R. Pallach, S. Salamon, H. Moldenhauer, J. Landers, H. Wende, J. Debus, S. Henke, Porous purple glass—A cobalt imidazolate glass with accessible porosity from a meltable cobalt imidazolate framework. *J. Mater. Chem. A Mater. Energy Sustain.* **7**, 985–990 (2019).

11 L. Frentzel-Beyme, M. Kloß, P. Kolodzeiski, R. Pallach, S. Henke, Meltable mixed-linker zeolitic imidazolate frameworks and their microporous glasses—From melting point engineering to selective hydrocarbon sorption. *J. Am. Chem. Soc.* **141**, 12362–12371 (2019).

12 M. A. Ali, J. Ren, T. Zhao, X. Liu, Y. Hua, Y. Yue, J. Qiu, Broad mid-infrared luminescence in a metal-organic framework glass. *ACS Omega* **4**, 12081–12087 (2019).

13 A. Qiao, H. Tao, M. P. Carson, S. W. Aldrich, L. M. Thirion, T. D. Bennett, J. C. Mauro, Y. Yue, Optical properties of a melt-quenched metal-organic framework glass. *Opt. Lett.* **44**, 1623–1625 (2019).

14 A. Qiao, T. D. Bennett, H. Tao, A. Krajnc, G. Mali, C. M. Doherty, A. W. Thornton, J. C. Mauro, G. N. Greaves, Y. Yue, A metal-organic framework with ultrahigh glass-forming ability. *Sci. Adv.* **4**, eaao6827 (2018).

15 J. Zhang, L. Longley, H. Liu, C. W. Ashling, P. A. Chater, K. A. Beyer, K. W. Chapman, H. Tao, D. A. Keen, T. D. Bennett, Y. Yue, Structural evolution in a melt-quenched zeolitic imidazolate framework glass during heat-treatment. *Chem. Commun.* **55**, 2521–2524 (2019).

16 R. Gaillac, P. Pullumbi, K. A. Beyer, K. W. Chapman, D. A. Keen, T. D. Bennett, F.-X. Coudert, Liquid metal-organic frameworks. *Nat. Mater.* **16**, 1149–1154 (2017).

17 A. P. M. Kentgens, A practical guide to solid-state NMR of half-integer quadrupolar nuclei with some applications to disordered systems. *Geoderma* **80**, 271–306 (1997).

18 A. Sutrisno, V. V. Terskikh, Q. Shi, Z. Song, J. Dong, S. Y. Ding, W. Wang, B. R. Provost, T. D. Daff, T. K. Woo, Y. Huang, Characterization of Zn-containing metal-organic frameworks by solid-state $^{67}$Zn NMR spectroscopy and computational modeling. *Chemistry* **18**, 12251–12259 (2012).

19 K. H. Mroué, W. P. Power, High-field solid-state $^{67}$Zn NMR spectroscopy of several zinc-amino acid complexes. *J. Phys. Chem. A* **114**, 324–335 (2010).

20 T. Bastow, NMR in zinc metal. *J. Phys. Condens. Matter* **8**, 11309–11315 (1996).

21 G. Wu, S. Kroeker, R. E. Wasylishen, Multinuclear NMR study of dipotassium tetracyanometalates of the group 12 metals in the solid state. *Inorg. Chem.* **34**, 1595–1598 (1995).

22 F. H. Larsen, A. S. Lipton, H. J. Jakobsen, N. C. Nielsen, P. D. Ellis, $^{67}$Zn QCPMG solid-state NMR studies of zinc complexes as models for metalloproteins. *J. Am. Chem. Soc.* **121**, 3783–3784 (1999).

23 A. S. Lipton, R. W. Heck, P. D. Ellis, Zinc solid-state NMR spectroscopy of human carbonic anhydrase: Implications for the enzymatic mechanism. *J. Am. Chem. Soc.* **126**, 4735–4739 (2004).

24 D. Massiot, F. Fayon, M. Capron, I. King, S. Le Calvé, B. Alonso, J.-O. Durand, B. Bujoli, Z. Gan, G. Hoatson, Modelling one- and two-

dimensional solid-state NMR spectra. *Magn. Reson. Chem.* **40**, 70–76 (2002).

25 J.-B. d'Espinose de Lacaillerie, C. Fretigny, D. Massiot, MAS NMR spectra of quadrupolar nuclei in disordered solids: The Czjzek model. *J. Magn. Reson.* **192**, 244–251 (2008).

26 R. Gaillac, P. Pullumbi, F.-X. Coudert, Melting of zeolitic imidazolate frameworks with different topologies: Insight from first-principles molecular dynamics. *J. Phys. Chem. C* **122**, 6730–6736 (2018).

27 D. C. Clupper, L. L. Hench, Crystallization kinetics of tape cast bioactive glass 45S5. *J. Non-Cryst. Solids* **318**, 43–48 (2003).

28 P. Z. Moghadam, A. Li, S. B. Wiggin, A. Tao, A. G. P. Maloney, P. A. Wood, S. C. Ward, D. Fairen-Jimenez, Development of a cambridge structural database subset: A collection of metal-organic frameworks for past, present, and future. *Chem. Mater.* **29**, 2618–2625 (2017).

29 R. Banerjee, A. Phan, B. Wang, C. Knobler, H. Furukawa, M. O'Keeffe, O. M. Yaghi, High-throughput synthesis of zeolitic imidazolate frameworks and application to $CO_2$ capture. *Science* **319**, 939–943 (2008).

30 Z. Gan, I. Hung, X. Wang, J. Paulino, G. Wu, I. M. Litvak, P. L. Gor'kov, W. W. Brey, P. Lendi, J. L. Schiano, M. D. Bird, I. R. Dixon, J. Toth, G. S. Boebinger, T. A. Cross, NMR spectroscopy up to 35.2T using a series-connected hybrid magnet. *J. Magn. Reson.* **284**, 125–136 (2017).

31 R. Siegel, T. T. Nakashima, R. E. Wasylishen, Sensitivity enhancement of NMR spectra of half-integer spin quadrupolar nuclei in solids using hyperbolic secant pulses. *J. Magn. Reson.* **184**, 85–100 (2007).

32 E. Kupce, R. Freeman, Adiabatic pulses for wideband inversion and broadband decoupling. *J. Magn. Reson.* **115**, 273–276 (1995).

33 R. K. Harris, E. D. Becker, S. M. Cabral de Menezes, R. Goodfellow, P. Granger, NMR nomenclature. Nuclear spin properties and conventions for chemical shifts (IUPAC Recommendations 2001). *Pure Appl. Chem.* **73**, 1795–1818 (2001).

34 D. R. Spearing, ptchg: A FORTRAN program for point-charge calculations of electric field gradients (EFGs). *Comput. Geosci.* **20**, 615–624 (1994).

# SUPPORTING INFORMATION

Science
AAAS

Supplementary Materials for

## Direct Detection of Local Structure in Zeolitic Imidazolate Framework Glasses by Ultra-High Field $^{67}$Zn NMR

Rasmus S.K. Madsen, Ang Qiao, Jishnu Sen, Ivan Hung, Kuizhi Chen, Zhehong Gan,

Sabyasachi Sen,* Yuanzheng Yue*

Correspondence to: sbsen@ucdavis.edu (S.S.), yy@bio.aau.dk (Y.Z.Y.)

**This PDF file includes:**

## 5.1. MATERIALS AND METHODS

### 5.1.1. SYNTHESIS

#### Preparation of ZIF-4 crystals

ZIF-4 crystals were prepared by a modified version of a previously reported approach (3). Stock solutions of $Zn(NO_3)_2 \cdot 6H_2O$ (Sigma, 99.5%) and imidazole (Sigma, 99%) were prepared in N,N-dimethylformamide (DMF) (Sigma, 99%), yielding 0.06 M and 0.18 M solutions respectively. 40 mL of a 1:1 volumetric mixture of the stock solutions was transferred to a 100 mL blue cap bottle and stirred for 30 minutes. The bottle was sealed and solvothermal synthesis was carried out at 383 K for 96 hours. After a complete reaction, the solution was allowed to cool to ambient temperature overnight. The resultant white ZIF-4 crystals were filtered off the precursor solution and washed three times with ∼50 mL of DMF, followed by drying in an oven at 383 K for 12 hours.

#### Preparation of ZIF-62 crystals

Three separate stock-solutions, 0.2 M $Zn(NO_3)_2 \cdot 6H_2O$, 1.5 M imidazole, and 0.2 M benzimidazole (Sigma, 99%), were used to prepare ZIF-62 crystals. The three stock-solutions were mixed in a 100 mL blue cap bottle, corresponding to the molar ratio Zn:Im:bIm=1:13.5:1.5. The mixture was stirred for 30 minutes before the bottle was sealed and the solvothermal process was initiated at 403 K for 96 hours. Upon a complete reaction, the solution was allowed to cool to ambient temperature, before being filtered and washed three times in ∼50 mL DMF. The ZIF-62 crystals were then dried at 373 K for 4 hours. A ZIF-62 crystal with extra bIm was also synthesized using the same procedure above but with the molar ratio Zn:Im:bIm=1:13.5:3.0, we denoted it as ‘ZIF-62b’ sample.

#### Preparation of ZIF-zni crystals

ZIF-zni samples were prepared by heating the as-synthesized ZIF-4 crystals in a simultaneous thermal analyser (Netzsch STA 448 F1) involving both the differential scanning calorimetry (DSC) and thermogravimetry in argon. During heating at 10 K/min, the ZIF-4 crystals were first collapsed to the low-density amorphous phase (LDA), and then the latter was transformed into the high-density amorphous phase (HDA), the HDA recrystallizes to ZIF-zni at 758 K and finally cooled down to room temperature at 10 K/min.

#### Preparation of melt-quenched ZIF glasses

ZIF-4 glass was prepared by heating the ZIF-4 sample in a platinum crucible to 863 K (slightly above the melting point of 853 K) in the DSC in argon at 10 K/min, and then by cooling the melt to room temperature at 10 K/min. Note that ZIF-4 glass was

derived by quenching the melt of ZIF-zni crystals during the DSC upscan. ZIF-62 crystal was melted and quenched to glass state in a tube furnace, using an inert argon atmosphere. The sample was heated to 733 K (above its melting point of about 693 K) at 10 K/min, followed by a 5-minute isothermal soaking, before being naturally cooled to room temperature.

## 5.1.2. CHARACTERIZATIONS

### Calorimetric analysis

During the DSC measurements, the as-synthesized ZIF-4 and -62 samples were held in a Pt crucible at 313 K for 5 minutes, and upscanned at 10 K/min to the targeted temperatures (see Fig. 1A), cooled back to 473 K at 10 K/min, and naturally to RT. A second upscan was performed on the melt-quenched glass sample to determine its glass transition temperature ($T_g$).

### Powder X-ray Diffraction

Powder X-ray diffraction (XRD) patterns were collected using a Panalytical Empyrean X-ray diffractometer operating at 45 kV and 40 mA, with Cu Kα radiation (λ=1.5418Å).

### Liquid $^{1}$H NMR spectroscopy

Solution $^{1}$H NMR spectra of digested samples (in a mixture of DCl (35%)/$D_2O$ (0.1 mL) and DMSO-$d_6$ (0.5 mL)) of desolvated ZIF-62 glasses (about 6 mg) were recorded on a Bruker Avance III 500MHz spectrometer at 293K. Chemical shifts were referenced to the residual protio-solvent signals of DMSO-$d_6$. The spectra were processed with the MestreNova Suite.

### $^{67}$Zn Solid-State MAS NMR

The $^{67}$Zn MAS NMR spectra for all samples were acquired at the NHMFL with 3.2 mm magic-angle spinning probes designed and developed at the NHMFL, and Bruker Avance NEO consoles. Spectra at 35.2 T were acquired using the NHMFL series-connected hybrid (SCH) magnet (30) at a frequency of $\nu_0(^{67}Zn)$ = 93.89 MHz with 10 kHz MAS, 0.1 s recycle delay and a 16.7 kHz rf field throughout. A 'full' spin-echo ($\pi/2$ - $\tau$ - $\pi$ - acq) was acquired with 5 and 10 μs $\pi/2$- and $\pi$-pulses and a six-rotor periods inter-pulse delay $\tau$ = 600 μs. In addition, a ~1.3 ms WURST-80 pulse with an offset of +350 kHz and a sweep width equal to the MAS frequency was applied prior to the spin-echo to saturate the $^{67}$Zn satellite-transitions and enhance the central-transition signal (31,32). Approximately 4000 to 8000 scans were averaged and Fourier transformed to obtain the spectra for the crystals, while for glasses approximately 65000 scans were averaged. Spectra at 19.5 T were acquired on a 31 mm bore superconducting magnet at a frequency of $\nu_0(^{67}Zn)$ = 52.02 MHz with 15.625 kHz MAS, 1 s recycle delay and a 16.7 kHz rf field throughout. The 'full' spin-echo ($\pi/2$ - $\tau$ - $\pi$ -

acq) was acquired with 5 and 10 μs π/2- and π-pulses, and τ = 256 μs. For signal enhancement, a ~2 ms WURST-80 pulse with an offset of +350 kHz and 15.625 kHz sweep width was applied. Approximately 80000 to 85000 scans were averaged and Fourier transformed to obtain the spectra for the crystals, while for glasses approximately 90000 to 150000 scans were averaged. All spectra were indirectly referenced to a saturated $Zn(NO_3)_2$ aqueous solution with $\delta_{iso}$ = 0 ppm by measuring the $^{17}O$ resonance frequency of tap water and using the frequency ratios between $^{17}O$ and $^{67}Zn$ reported in the IUPAC recommendations (33), i.e., $\nu(^{67}Zn, Zn(NO_3)_2) = \nu(^{17}O, H_2O) \times 6.256803/13.556457$.

$^{67}Zn$ being a quadrupolar nuclide, its NMR spectra may provide not only the information on the chemical shift that is characteristic of its tetrahedral environment but also on the electric field gradient (EFG) at the site of this nuclide in the structure, as encoded in its quadrupolar coupling constant $C_Q$ and asymmetry parameter $\eta_Q$. The EFG is a second rank tensor quantity that is known to be sensitive to the degree of positional and orientational order at length scales corresponding to the nearest and next-nearest neighbor distances and possibly somewhat beyond. This sensitivity of the EFG to short- and intermediate-range structural order around the nuclide in question is particularly obvious when one considers the distance dependence of the symmetric second-rank EFG tensor components $V_{ij}$ (i,j= x,y,z) at any location, resulting from a point charge $\eta_e$ at a distance **r** (point-charge approximation), which is given by the relation (34):

$$V_{ij} = -\frac{\zeta e}{4\pi\varepsilon_0}\left(\frac{3r_i r_j - |\mathbf{r}|^2 \partial_{ij}}{|\mathbf{r}|^5}\right) \quad (1)$$

where e and $\eta_0$ are the electronic charge and permittivity constant, respectively, **r** is the radius vector from the point of interest to the ion and $\eta_{ij}$ is the Kronecker delta function. The EFG tensor can be diagonalized to obtain its principal components $|V_{xx}| \leq |V_{yy}| \leq |V_{zz}|$. The NMR parameters $C_Q$ and $\eta_Q$ are then related to these principal components as:

$$C_Q = eQV_{zz}/h \quad (2)$$

$$\eta_Q = (V_{xx} - V_{yy})/V_{zz} \quad (3)$$

where Q is the nuclear quadrupole moment and h is Planck's constant.

## 5.2. SUPPLEMENTARY FIGURES

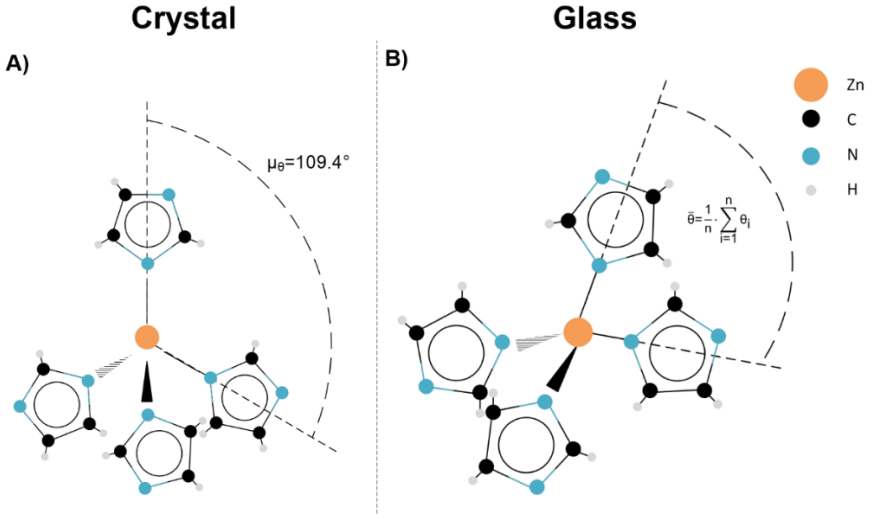


**Figure S1**. **Schematic representation of the change of structural unit from crystalline ZIF to its glassy state**. Structural units of ZIF crystal (A), with a population average N-Zn-N bond angle ($\mu_\theta$) of 109.4° based on the mean of crystals in Table S2, and ZIF glass (B) with a broad distribution of the N-Zn-N bond angle ($\bar{\theta}$).

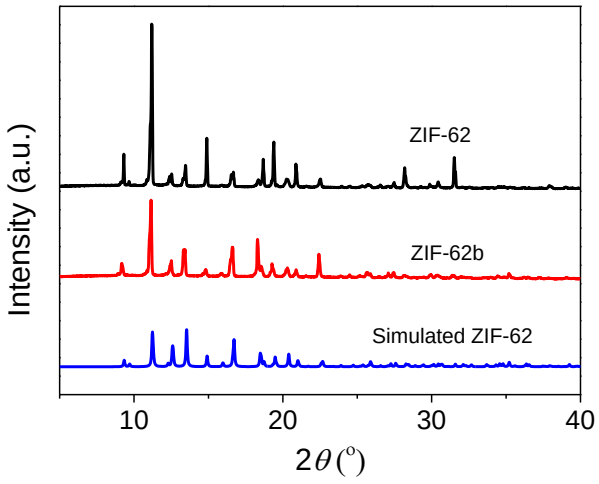


**Figure S2**. XRD patterns of two ZIF-62 samples with different linkers ratios added during synthesis.

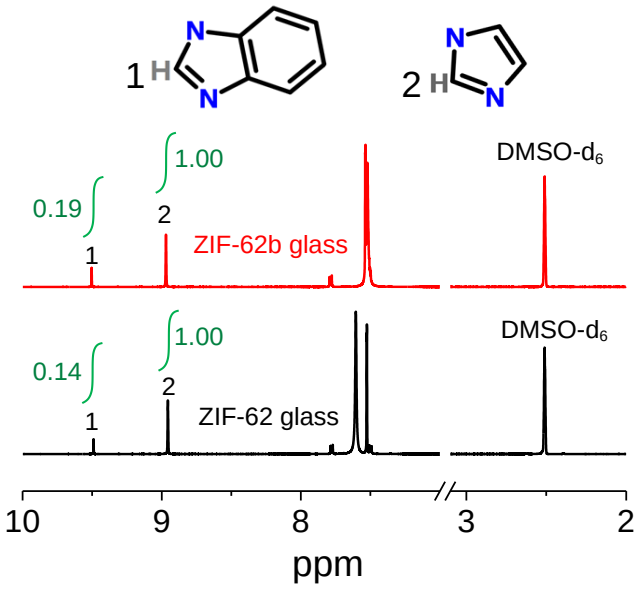


**Figure S3**. **Characterization of linker ratios.** Solution $^{1}$H NMR spectra of two ZIF-62 samples with different linkers ratios added during synthesis. The ratio of linkers (bIm/Im) can be obtained by integrating the characteristic peaks of the bIm (peak 1, NHN in bIm) and Im (peak 2, NHN in Im).

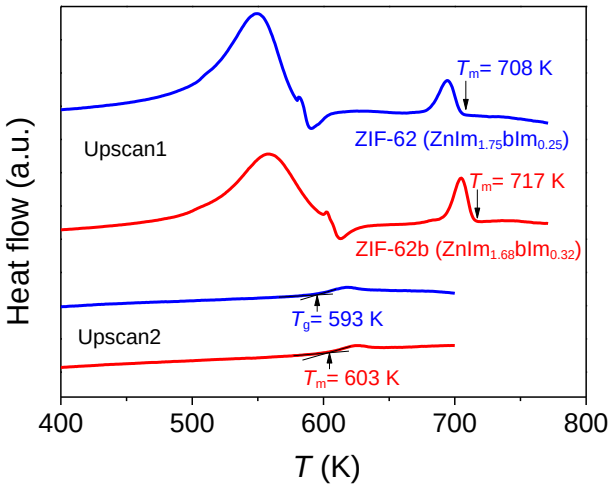


**Figure S4**. **Calorimetry of ZIF-62 samples**. Isobaric heat capacity ($C_p$) curves of standard ZIF-62 sample ($Zn(Im)_{1.75}(bIm)_{0.25}$) and ZIF-62b sample with extra bIm ($Zn(Im)_{1.68}(bIm)_{0.32}$) during the first upscan heated at 10 K/min, showing the desolvation and melting peaks. The second upscans $C_p$ curves of ZIF-62 samples quenched from above $T_m$ exihiting clear glass transition peaks.

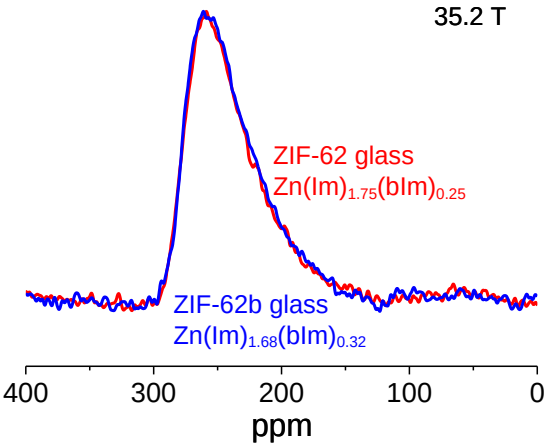


**Figure S5.** $^{67}Zn$ MAS NMR spectra of standard ZIF-62 glass ($Zn(Im)_{1.75}(bIm)_{0.25}$) and ZIF-62b glass with extra bIm ($Zn(Im)_{1.68}(bIm)_{0.32}$) obtained under 35.2 T magnetic field.

**Table S1**. Molar ratios of both the synthesis-added and the measured bIm/(Im+bIm) for ZIF-62 samples with various linkers ratios

| Samples | Added Zn:Im:bIm | Added bIm/(Im+bIm) | Measured bIm/(Im+bIm) | Composition |
|---|---|---|---|---|
| ZIF-62 | 1:13.5:1.5 | 0.1 | 0.125 | $Zn(Im)_{1.75}(bIm)_{0.25}$ |
| ZIF-62b | 1:13.5:3.0 | 0.18 | 0.16 | $Zn(Im)_{1.68}(bIm)_{0.32}$ |

**Table S2**. Distribution of N-Zn-N bond angles in ZIF-4, ZIF-62 and ZIF-zni crystals.

| N-Zn-N bond angles (°) | | | | | | |
|---|---|---|---|---|---|---|
| | ZIF-4 | | ZIF-62 | | ZIF-zni | |
| | Zn1 | Zn2 | Zn1 | Zn2 | Zn1 | Zn2 |
| | 104.07 | 107.77 | 110.5 | 105.6 | 109.3 | 110 |
| | 110.59 | 113.34 | 105.3 | 112.1 | 113.1 | 108.8 |
| | 110.93 | 105.3 | 109.9 | 111.5 | 108.9 | 113.4 |
| | 113.5 | 111.11 | 108 | 107.9 | 104.7 | 112.9 |
| | 109.3 | 110.2 | 109.8 | 110.3 | 102.1 | 108.4 |
| | 107.96 | 108.91 | 113 | 109.5 | 117.8 | 103.9 |
| **Max** | 113.5 | 113.34 | 113 | 112.1 | 117.8 | 113.4 |
| **Min** | 104.07 | 105.3 | 105.3 | 105.6 | 102.1 | 103.9 |
| **Diff** | 9.43 | 8.04 | 7.7 | 6.5 | 15.7 | 9.5 |
| **Average** | 109.39 | 109.44 | 109.42 | 109.48 | 109.32 | 109.57 |
| **STD** | 3.20 | 2.79 | 2.58 | 2.42 | 5.65 | 3.47 |

**Table S3**. Distribution of Zn-N bond lengths in ZIF-4, ZIF-62 and ZIF-zni crystals.

| Zn-N bond lengths (Å) | | | | | | |
|---|---|---|---|---|---|---|
| | ZIF4 | | ZIF-62 | | ZIF-zni | |
| | **Zn1** | **Zn2** | **Zn1** | **Zn2** | **Zn1** | **Zn2** |
| | 1.997 | 1.982 | 1.99 | 1.986 | 1.96 | 2.03 |
| | 1.992 | 1.973 | 1.979 | 1.978 | 2.05 | 1.992 |
| | 1.967 | 1.979 | 1.967 | 1.99 | 1.982 | 1.983 |
| | 1.98 | 1.991 | 1.989 | 1.987 | 1.98 | 1.94 |
| **Max** | 1.99 | 1.99 | 1.99 | 1.99 | 2.05 | 2.03 |
| **Min** | 1.96 | 1.97 | 1.96 | 1.97 | 1.96 | 1.94 |
| **Diff** | 0.03 | 0.02 | 0.02 | 0.01 | 0.09 | 0.09 |
| **Average** | 1.98 | 1.98 | 1.98 | 1.99 | 1.99 | 1.99 |
| **STD** | 0.013 | 0.008 | 0.011 | 0.005 | 0.039 | 0.037 |

## References

30. Z. Gan, I. Hung, X. L. Wang, J. Paulino, G. Wu, I. M. Litvak, P. L. Gor'kov, W. W. Brey, P. Lendi, J. L. Schiano, M. D. Bird, I. R. Dixon, J. Toth, G. S. Boebinger, T. A. Cross, NMR spectroscopy up to 35.2T using a series-connected hybrid magnet. J. Magn. Reson. **284**, 125-136 (2017). doi:10.1016/j.jmr.2017.08.007

31. R. Siegel, T. T. Nakashima, R. E. Wasylishen, Sensitivity enhancement of NMR spectra of half-integer spin quadrupolar nuclei in solids using hyperbolic secant pulses, J. Magn. Reson. **184**, 85-100 (2007). doi:10.1016/j.jmr.2006.09.007

32. E. Kupce, R. Freeman, Adiabatic Pulses for Wideband Inversion and Broadband Decoupling, J. Magn. Reson. **115**, 273-276 (1995). doi:10.1006/jmra.1995.1179

33. R. K. Harris, E. D. Becker, S. M. Cabral de Menezes, R. Goodfellow, P. Granger, NMR nomenclature. Nuclear spin properties and conventions for chemical shifts (IUPAC Recommendations 2001), Pure Appl. Chem. **73**, 1795-1818 (2001). doi:10.1351/pac200173111795

34. D. R. Spearing, ptchg: A FORTRAN program for point-charge calculations of electric field gradients (EFGs), Comput. Geosci. **20**, 615-624 (1994). doi:10.1016/0098-3004(94)90083-3

# 6. BIMETALLIC CU/ZN ZIF-4

Bimetallic Cu/Zn-ZIF-4 crystals were prepared with the specific goal of expanding on the work of chapter 4. In chapter 4, the incorporation of cobalt results in a structural mismatch in the Zn-ZIF-62 structure, resulting in a non-additive change in $T_m$ and $T_g$, i.e. the mixed metal node effect. Low cobalt concentrations produce a characteristic drop in $T_m$ and $T_g$, however, the chapter does not explain why the same drop is not seen between pure cobalt ZIF-62 and low Zn ZIF-62. This chapter seeks to expand on the mixed metal node effect, specifically elucidating the origin of the characteristic drop in $T_m$ at small metal substitution. Copper was chosen for this, as it has potential applications in areas like catalysis, while still arranging in tetrahedral coordination. This chapter outlines the synthesis and analysis of the Cu/Zn-ZIF-4 samples. The melting and glass-forming characteristics of Cu-modified ZIF-4 further shed light on the mixed metal node effect. Small amounts of copper (1 mol%) in the framework significantly decrease the melting temperature of ZIF-4 and have a non-linear non-monotonic effect on $T_m$, similarly to Co/Zn-ZIF-62 in chapter 4. The cause of this observed $T_m$ minima at low copper substitution is ascribed to the inductive effects of $Cu^{2+}$ ions. The presence of copper at low concentrations destabilises the system by pulling on the electron could of the imidazolate unit, causing the electron density of the neighbouring Zn atoms to be weakened. This weakening leads to scission occurring at lower temperatures, which then decreases the network connectivity enabling melting at significantly lower temperatures.

## 6.1. EXPERIMENTAL WORK

**Synthesis:** stock solutions of zinc acetate, copper acetate and imidazole were prepared to make the systematic substitution of Cu for Zn easier. 2.694 grams of zinc acetate dihydrate (sigma) was dissolved in 100 mL DMF. 0.551 grams of copper acetate monohydrate (Merck) was dissolved in 25 mL DMF. 4.999 grams of imidazole was dissolved in 200 mL DMF (N, N-dimethylformamide). The three solutions were mixed in a ratio in accordance with Table 6.1. the solutions were stirred with a magnetic stirrer for 30 minutes before being transferred to closed 100 mL glass vessels and placed at 110 °C for 96 hours and then cooled to ambient temperature after the crystals were formed. The crystals were washed three times with DMF and once with DCM (dichloromethane) before being dried at 110 °C overnight. The sample names are given with the mol fraction of Cu present in the structure, i.e. 0.2-Cu-ZIF-4 was synthesised with 20 mol% Cu.

*Table 6.1 mixing ratio of stock solution for Cu/Zn-ZIF-4 synthesis.*

| Structure | Zn-solution [mL] | Cu-solution [mL] | Imidazole-solution [mL] | DMF [mL] |
|---|---|---|---|---|
| 0.2-Cu-ZIF-4 | 12 | 3 | 15 | 30 |
| 0.1-Cu -ZIF-4 | 13.5 | 1.5 | 15 | 30 |
| 0.05-Cu -ZIF-4 | 14.25 | 0.75 | 15 | 30 |
| 0.01-Cu -ZIF-4 | 14.85 | 0.15 | 15 | 30 |

**PXRD:** The as-synthesised crystals were placed on an amorphous silicon sample holder (PANalytical). A copper radiation source (1.541 Å and 1.544 Å) using a PIXcel$^{1D}$ detector. 0.04 Rad sollers, with 1/8° divergence slits, 1/4° anti-scatter slits, and a 10 mm beam mask equipped on the incident beam side. On the diffracted beam side, a 7.5 anti-scatter slit, with a large nickel filter, and a 0.04 Rad soller was used. A step size of 0.01313° and a range of 3 to 40° was used for the measurement of the mixed metal ZIF-4 samples.

**Simultaneous thermal analysis (STA):** Calorimetric analysis (DSC+TGA) of the synthesised samples was carried out on a NETZSCH f449 F3 STA, equipped with a steel furnace and a type P thermocouple, using argon as the protective atmosphere. The samples were heated to 480 °C, then cooled to 80 °C followed by two heating cycles to 410 °C. All dynamic steps were carried out with a temperature ramp of 10 K min$^{-1}$.

## 6.2. FINDINGS

PXRD revealed that the synthesised crystals have a very similar pattern to a simulated pattern from a CIF file found in the literature (95). When comparing the samples to the reference in Figure 6.1 it is concluded that the synthesised crystals were of a pure *Pbca* space group, with no detectable secondary crystalline phases. The absence of any unpredicted peaks indicates the effective incorporation of copper into the structure. Hence, any deviations in calorimetric characteristics, i.e., melting and glass-forming trends can be ascribed to the effect of copper on the framework, rather than ascribed to the effect of contaminating phases.

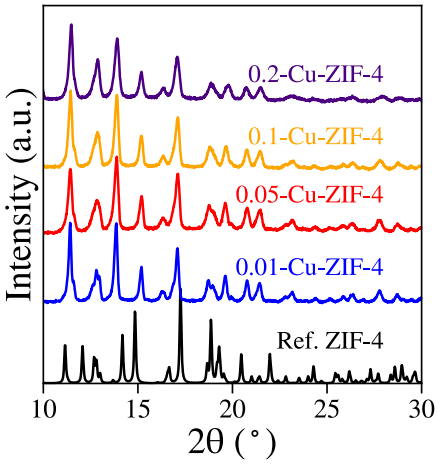


*Figure 6.1 PXRD measurements of Cu-modified ZIF-4.*

The DSC measurements in Figure 6.2 reveals a clear endothermic peak for 0.01-Cu-ZIF-4. Detectable decomposition occurs for the samples with a higher Cu/Zn ratio. The significant mass-loss present (Figure 6.2 b)) is attributed to carbonisation, which is confirmed by visual inspection of the samples in Figure 6.3. Only 0.01-Cu-ZIF-4 presents with a high-quality glass sample, while 0.05- to 0.2-Cu-ZIF-4 are visibility carbonised, indicating that MA is approaching 0. 0.01-Cu-ZIF-4 exhibits a $T_m$ offset of 342.4 °C, which is a difference of almost 248 °C when compared to the conventional melting temperature of ZIF-4 as given in chapter 2 (168). the glass transition temperature varies by 8 °C from the value reported in the literature with a $T_g$ of 284.2 °C. The ability of the 0.01-Cu-ZIF-4 to melt and form a glass contradicts the findings of Stepniewska (169), however, even with 5 mol% Cu being used, GFQ is compromised significantly, as evident by partial carbonisation. The melting point of 0.05-Cu-ZIF-4 is 372.7, a stark increase from that of the 1% Cu ZIF-4 sample. Further increase of copper content to 10 and 20 mol% results in a decrease in $T_m$. The reported $T_m$ of 0.1-Cu-ZIF-4 and 0.2-Cu-ZIF-4 is accompanied by significant carbonisation, as observed with the visible negative slope at the TGA plot above 300 °C as seen in Figure 6.2 b). Because of this decomposition, the exact determination of $T_m$ is difficult. This effect is very similar to the one outlined in chapter 4, where a non-linear and non-monotonic effect on $T_m$ is observed.

The glass transition peak is observed to decrease with increasing $Cu^{2+}$ substitution, which is unlike the findings of Chapter 4, however, due to the thermal instability of the samples with higher copper substitution ratios, this effect is unclear if it is caused by the partial decomposition or another effect. The glass-forming ability ($T_g/T_m$, in kelvin) for each Cu-substituted ZIF-4 is very high, 0.91, 0.86, 0.87, and 0.87 for 0.01-, 0.05-, 0.1, and 0.2-ZIF-4 respectively. The extremely high GFA suggests that the samples, despite their thermal sensitivity, have high resistance against crystallisation. Likely, this increased GFA is partially due to an increase in the entropy of fusion ($\Delta S_{fus}$), as it is known that an increase in possible conformations will yield a higher $\Delta S_{fus}$ (170). Despite this high GFA, the low MA results in these samples having a lower GFQ, when compared to ZIF-62 glasses.

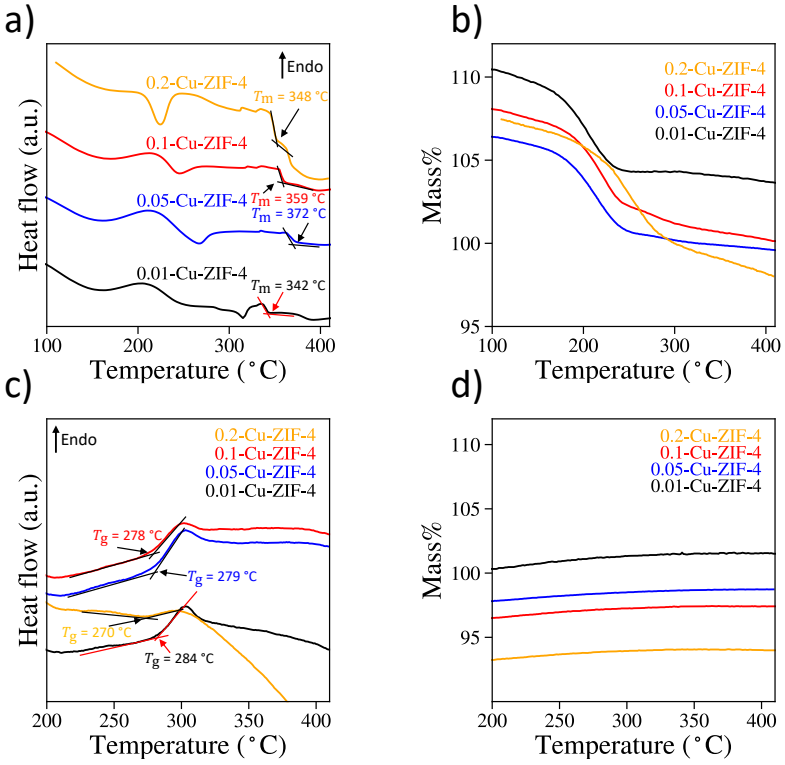


*Figure 6.2 STA measurements of Cu-ZIF-4 crystals a) DSC signal upscan 1 b) TGA signal upscan 1 c) DSC signal upscan 2 d) TGA signal upscan 2.*

Due to the absence of any secondary phases, the strong decrease in $T_m$ has to be ascribed to a strong mixed metal node effect. The addition of a small quantity of copper presents the largest effect, similar to the effects of incorporating bIm in ZIF-62 (24). It should be noted that not all Cu/Zn-ZIF-4 samples were able to be melted and

quenched into glasses without decomposition occurring, which complicates the analysis. Based on the work of Sarkar et *al.* (171), it is likely that this is tightly associated with the nature of the coordination bond itself. Based on their work, it can be inferred that the Cu-N bonds are more covalent in nature when compared to the Zn-N bonds, which is feasible due to the difference in electronegativity between the two metals (Zn=1.65, Cu=1.9 (172)). This ties well in with the notion of a mixed metal node effect (148) and that the scission and renewal of metal to linker coordination bonds is the driving force for the melting mechanism, with the latter being experimentally supported by solid state $^{67}$Zn-NMR (17). The presence of the short-range disorder is contradicting the notion that short-range structure is retained, as is the case with the CRN (continuous random network) model) (5,173–175). However, as the presence of short-range disorder has been proven by solid-state NMR, the current selecting criteria for melting in simulations might not be appropriate.

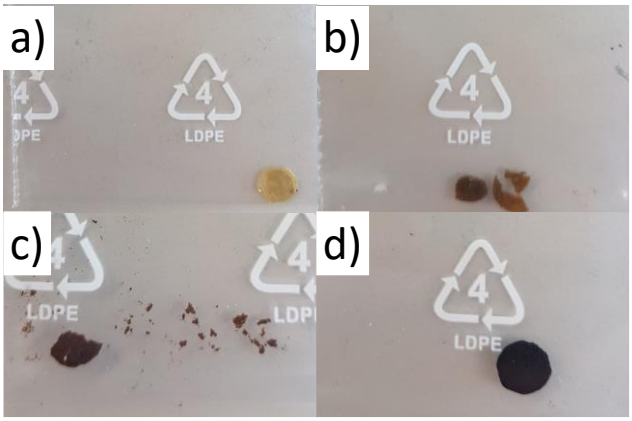


*Figure 6.3 Optical image of Cu/Zn-ZIF-4 glass samples. a) 0.01-Cu-ZIF-4 glass b) 0.05-Cu-ZIF-4 glass c) 0.1-Cu-ZIF-4 glass d) 0.2-Cu-ZIF-4 glass.*

The findings of these Cu-modified ZIF-4 samples provide further evidence of the mixed metal node effect in metal-organic framework glasses. To be able to describe the non-linear, non-monotonic effect observed some alterations to the initial description in the published work in chapter 4 (148) can be made. Based on the observations in chapter 4 and these Cu/Zn-ZIF-4 samples, two separate mechanisms are likely to occur, when substituting one metal node for another.

The first mechanism is the strengthening of the average metal-to-nitrogen coordination bond. This partially explains the reason why pure copper and pure cobalt-based ZIFs generally exhibit lower GFQ. The strengthening is caused by copper possessing a stronger, more covalent, coordination bond with nitrogen, while Zn-N bonds are more ionic.

Second, the strengthening is likely counteracted by copper (or cobalt) drawing more on the electrons compared to zinc: the higher electronegativity leads to the electron density of the aromatic ring increasing at the Cu-N bond and decreasing at the Zn-N bond, as illustrated in Figure 6.4. This effect would further weaken a subset of the Zn-N bond when compared to conventional Zn-ZIF-4. During heating, the Zn-N bonds which are weakened by the presence of Cu ions will then have a greater thermal vibration, which then enables these sites to sever more easily. The severing of the weakened Zn-N bonds then reduces the network connectivity, which allows the material to reach Lindemann's criterion for melting at lower temperatures (114,176,177). Once the Cu content is sufficiently high, the weakening of the Zn-N bonds is offset by the stronger Cu-N bonds. This explains the non-monotonic effect of metal substitution observed during heating.

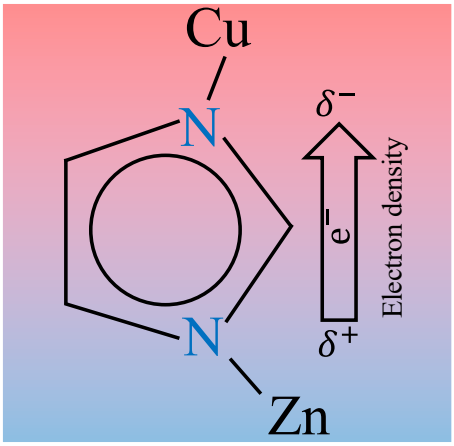


*Figure 6.4 Schematic drawing illustrating the electron drawing effect, causing a weakening of the Zn-N bond.*

The destabilisation appears to not only be caused by a structural mismatch between ionic sizes and electron configurations. Perhaps more importantly, the mixed metal node effect appears to be driven by the nature of the metal-to-linker bond. By having more covalent bonds on average, the MA is decreased. However, the introduction of metal nodes which can promote an uneven electron distribution in the imidazolate-based linker appears to dramatically decrease the melting temperature, by weakening a subset of metal-to-nitrogen bonds. In this case, the Cu ions draw on the electrons, leading the neighbouring Zn ions to form weaker bonds with nitrogen. This appears to be the case for Co/Zn-ZIF-62 as well. However, the calorimetric behaviour of ZIF-new in chapter 4 is less directly applicable.

The unknown chemical structure of ZIF-new complicates the discussion of the importance of the mixed metal node effect for this series of ZIFs for two major reasons. First, the emergence of a secondary phase in ZIF-new makes it much more complex to ascertain the mixed metal node effect. The presence of two distinct phases can cause a significant change in thermal behaviour. The unknown chemical composition complicates and excludes the assessment of chemical bond strength. Without further study, it is not possible to make any inferences on the possible effects of the metal substitution in this crystal phase. Second, the unknown crystal structure excludes assessments of symmetry effects as well as lattice parameter effects. For further knowledge of this novel ZIF structure, knowledge of the chemical composition is required. A possible, but not verified explanation of the change in ligand chemistry could be a Co-catalysed coupling of the aromatic rings. Though the nature of the coupling would have to result in a lowering in the electron density of the aromatic system, as to allow the $^{1}H$ to shift to a higher field (178). The validity of this theory is questioned by limited publications demonstrating the coupling of non-functionalized aromatic rings, whereas organotin or boron (Stille and Suzuki coupling) are commonly used for coupling aromatic compounds (179–181). However, if the nature of the *in-situ* linker modification is elucidated, then this will provide a significant contribution to the understanding of the mixed metal node effect.

Another possible conceptualisation for the changes in $T_m$ and $T_g$ in Co/Zn-ZIF-62 and Cu/Zn-ZIF-4 is that the addition of a second metal ion leads to a eutectic point in a binary phase diagram. This would be conceptually analogous to the phase diagram presented by Widmer et al. (113). A phase diagram shows at which conditions (temperature, pressure…) certain thermodynamically distinct phases occur (182). This is typically used for alloys and is a very useful tool for reading out the thermodynamic behaviour of a specific composition of interest. However, several complications detract from using such a model to explain the melting behaviour of MOF glass formers.

First, MOFs can consist of several organic ligands and metal nodes. Because of this, it is difficult to avoid having composition variations that would lead to a three-dimensional composition-temperature phase diagram. Preparing such a phase diagram would be an arduous experimental endeavour.

Second, for the case of ZIF-62/ZIF-new mixtures, as observed in chapter 4, a phase diagram would potentially be viable. However, multiple unknown factors make the use of phase diagrams less appropriate. One, the ZIF-new is of an unknown crystal structure, which would reduce the information which could be gathered. Two, the chemical composition of ZIF-new is yet to be determined, meaning that it is not presently possible to discriminate neither the chemical nor the structural differences of such a phase diagram. Three, the ligand in ZIF-new is likely being synthesised catalytically by the presence of cobalt. This means that the phase separation displayed in a phase diagram from the work presented in chapter 4 is based on the fact that the novel linker is being synthesised locally at the cobalt sites. By extension, it is therefore

not possible to ascertain if the formation of these two distinct phases is a consequence of inhomogeneous mixtures. It is reasonable to believe that if the organic ligand was determined that a reaction solution of zinc nitrate, cobalt nitrate, imidazole, benzimidazole, and the unknown linker, would produce a homogenous crystal structure, or a mix of crystal structures with a homogenous mixture of Zn and Co. This level of uncertainty will undermine the validity of such a phase diagram, as most vital information would be absent.

Third, the construction of a phase diagram will reveal the empirical results of a specific modification to a specific initial MOF structure and is therefore a powerful tool for selecting a composition with the desired thermodynamic/kinetic properties. A phase diagram, however, offers little information to explain the physical cause of the change in, e.g., $T_m$. For this thesis, the main objective is to relate structural characteristics to glass-forming behaviour in MOFs, with the ultimate objective of contributing to the general understanding of the melting mechanism of MOFs for the predictive design of future MOF glasses. In this capacity, the construction of phase diagrams of MOF glass formers will contribute little to the understanding of the melting mechanism.

In contrast, the mixed metal node effect proposes an initial mechanism for the change in melting behaviour, which has the potential for computational work of MOF glass systems. The present computational methods for predicting the melting of crystalline MOFs involve the Lindemann criterion for melting (132,177), i.e., by taking the ratio of the metal-linker thermal vibrations $\langle u \rangle$ and the interatomic distance $r$ (86). However, these calculations are known to underestimate the vibrational dynamics, which makes the $\langle u \rangle / r$ ratio at $T_m$ is highly dependent on the individual material (132). This approach for determining to melt is still presently used, as no better model for predicting $T_m$ is presently available (132). One of the major limitations of simulations of MOF glasses is that the current computational models used in molecular dynamics simulations are insufficient to effectively predict melting temperature (177). Some of the current methods used for simulations are density functional theory (DFT) and force field simulations (132,183,184). DFT belongs to a group of simulation models based on quantum mechanical computations (185). The major advantage of these models is their non-empirical basis. This means that the models, when used appropriately, are quite good at predicting phenomena and trends especially when related to the electronic structure (184,186). The avoidance of empirical potentials and the ability to study reactions that involve dissociation and reassociation of covalent bonds are factors that make DFT and first principle simulations especially attractive (184).

However, the reason why many computational studies are based on empirical is due to the computational demands of analytical models (184). For most quantum mechanical simulations, simulations are generally not carried out on systems exceeding a few hundred atoms (187). With MOFs having unit cells that can exceed 50 unique atoms (95), it is clear how models with a high computational load will be limited in simulation size. For characteristics requiring larger simulation systems, like, crack propagation in glasses (188), ion-exchange strengthening (189), and ionic conduction (190), this limitation to the size of the system makes quantum mechanical models inappropriate.

Classical MD simulations based on empirical models like force field have a significantly lower computational demand (184). This means that the systems being simulated can be much larger when compared to that of DFT calculations, and the simulation systems are often several orders of magnitude larger in number of atoms when compared to quantum mechanical simulations (184). This would make simulations of $T_m$ of MOF glass formers much more appropriate. However, the predicting power of these simulations is dictated by which empirical model is being used (183). Most MD potential models are based on empirical developments, meaning that the applicability is tied to the specific potential models used (183). The development of silicate potentials outstrips that of less studied glass formers, like boron in borosilicate glasses (191). Therefore, simulations of novel glass systems like dmbIm-modified ZIF-62 are subject to much larger uncertainty.

Developing a rigorous model for the melting- and glass-forming mechanism would therefore be useful for simulation work. Understanding the melting mechanism and being able to incorporate this effect into a mathematical expression, that more reliably predicts the melting of MOFs would be a ground-breaking development. The successful implementation of simulations for predicting $T_m$ of new MOF glass formers will significantly improve future research output, as trial-and-error approaches for the development of novel MOF glasses can be largely avoided. The local disorder demonstrated by the solid-state NMR results in chapter 4, in combination with the mixed metal node effect, could be used for selecting or developing more appropriate models for predicting $T_m$ of MOFs in the future.

# 7. ZIF WITH BIMODAL MELTING BEHAVIOUR

During the preparation of the samples for chapter 3, a dmbIm-modified ZIF-62 crystal was prepared which presented with hitherto unprecedented calorimetric response to heating. A bimodal melting endotherm is observed during the initial heating cycle. This was attributed to a bimodal melting peak as subsequent cooling and heating cycles revealed a bimodal glass transition peak. This chapter seeks to elucidate the novel melting and glass transition characteristic of this dmbIm-ZIF-62 sample, through *in-situ* structural characterisations. VT-Raman, *in-situ* synchrotron PXRD, and *in-situ* PDF were carried out in this novel ZIF. The crystal phase exhibits minimal thermal expansion/contraction during heating. No secondary crystal phase was able to be detected during the heating of the samples. While the origin of this bimodal behaviour remains inconclusive, the dmbIm-ZIF-62 sample has exciting characteristics worth further investigation.

## 7.1. EXPERIMENTAL WORK

**Synthesis:** 0.46 grams of zinc nitrate hexahydrate ($Zn(NO_3)_2$), 6.6 grams of imidazole, 3 grams of benzimidazole, and 0.94 grams of 5,6-dimethylbenzimidazole were weighed into a glass beaker with a magnetic stir bar in it. The powders were dissolved in 60 mL DMF and stirred for 30 minutes, and transferred to a 100 mL Teflon-lined steel autoclave. The autoclaves were sealed and placed in an oven at 130 °C for 96 hours. After the given time, the solutions were allowed to cool naturally to ambient temperature inside the oven overnight. The recovered crystals were washed three times with DMF and one time with DCM. The washed crystals were dried in an oven at 110 °C overnight.

**PXRD:** The as-synthesised crystals were analysed with the same protocol as the one outlined in chapter 3 (146).

**STA:** Calorimetric analysis of these samples is carried out with the same protocol outlined in chapter 3 (146).

**Synchrotron *in-situ* PDF/PXRD:** All scattering data were collected at the I15-1 beamline at the Diamond Light Source ($\lambda$= 0.161669 Å, E=76.69 keV) (192). The samples were crushed using an agate mortar. The samples measured at ambient temperatures were loaded into 1 mm Kapton tubes, with quartz wool holding the sample, and super glue sealing the capillary. Measurements were carried out in the region Q~0.7 to 25 $Å^{-1}$ with data collection being 20 minutes each. Data acquisition was carried out for both samples and an empty capillary. Two PerkinElmer detectors were

used for recording PDF and powder diffraction simultaneously. The wavelength and sample-detector distance were calibrated with a Si standard using the program DAWN (193–195).

An empty container was used for subtracting the signal of the capillary, and Compton and absorption corrections were carried out on the GundrunX software before transforming the structure factor to pair distribution function. The GundrunX software package utilises the HHS function and a revised Lorch function for the conversion from reciprocal space to real space (196). For the *in-situ* measurements, borosilicate capillaries were used instead, with a similar approach as above. A hot air blower was used for heating the samples to the desired temperature.

**Synchrotron PXRD:** The samples were sent to the DIAMOND facilities. Measurements were carried out on beamline I12 (197,198) at ambient temperature. Kapton capillaries were used for the sample holder, with a Pilatus 2M CdTe detector for data acquisition. The wavelength and sample-detector distance were calibrated, using a CeO2 standard through the program DAWN (193–195).

**VT-Raman:** Variable temperature (VT) Raman was carried out on a Horiba Jobin Yvon (Japan) LabRAM HR800 with a semiconductor laser at 785 nm. A silicon wafer was used to calibrate the Raman shift. Each sample was tested at ambient temperature, and in increments of 50 K until 673 K was reached, followed by increments of 25 K until the signal quality deteriorated. The temperatures were controlled on a LINKAM FTIR 600 stage, connected to a nitrogen gas flow to protect the samples during heating.

**S-NMR:** solution $^{1}$H-NMR was carried out with the same method outlined in chapter 3 (146).

## 7.2. FINDINGS

Liquid NMR data analysis was carried out with the same procedure as in chapter 3. The chemical composition of ZIF-x is [Zn $(Im)_{1.67}$ $(bIm)_{0.28}$ $(dmbIm)_{0.05}$], determined by S-NMR. The decreased Im:(bIm+dmbIm) ratio is ascribed to the significantly different reaction conditions. To ensure the crystal structure still being a *Pbca* space group, in-house PXRD was conducted.

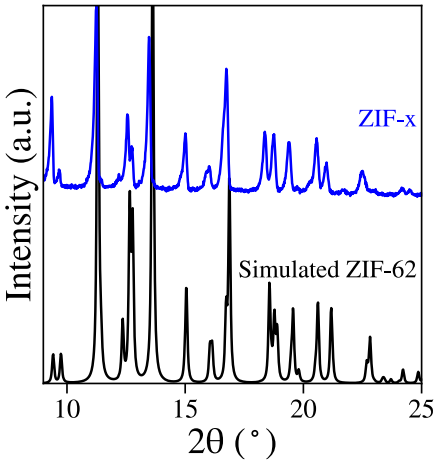


*Figure 7.1 PXRD measurement of ZIF-x with a ZIF-62 reference from the literature* (95)*. The asterisks (*) highlight peak differences.*

Figure 7.1 reveals the in-house PXRD measurement carried out on the ZIF-x sample with a reference ZIF-62 sample (199). The powder diffraction pattern confirms the presence of ZIF-62 crystals, however, several unaccounted peaks are present in the diffractogram, specifically at ~10°, 12.5°, and 16° 2θ. These points were initially attributed to imperfect sample preparation and were disregarded until the calorimetric analysis was carried out. A bimodal melting endotherm at 417 °C and 442 °C in Figure 7.2. In addition, Two $T_g$ were also detected at 319 °C and 329 °C respectively. The presence of a bimodal melting peak has previously been reported in studies dealing with mixed ZIF-4 and ZIF-62 samples (200). However, these samples produce only a bimodal melting peak, while the glass transition would be a singular unimodal peak. The presence of a bimodal $T_g$ suggests that both the crystalline sample and the resultant ZIF-x glass are phase separated.

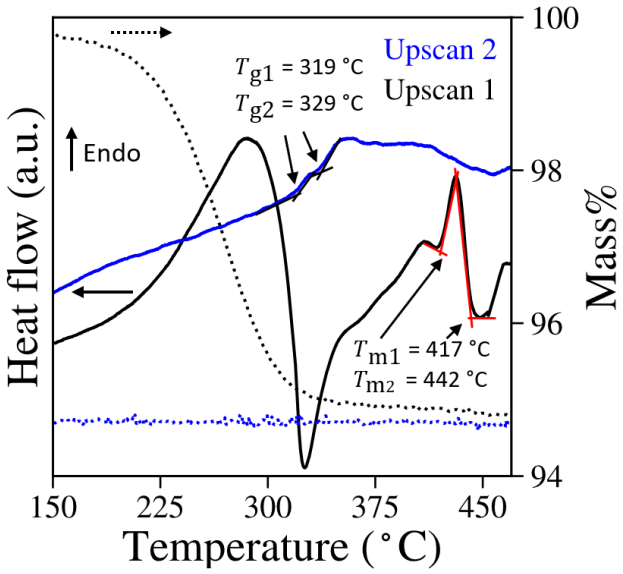


*Figure 7.2 STA measurement of ZIF-x showing the first and second upscan, highlighting the bimodal $T_m$ and $T_g$.*

The diffraction data from the in-house equipment does not provide sufficient resolution to be able to quantitatively determine the presence of a secondary phase. Single-crystal X-ray diffraction data would be preferable, however, the particle size is so small that single-crystal studies are unfeasible as seen in Figure 7.3. Additionally, Single-crystal analysis would not be able to detect the presence of two distinct crystal structures in a bulk sample unless the two crystals were intergrown on the same particle. As such, the powder samples were analysed by a synchrotron radiation source in an attempt to determine the presence of a secondary crystal phase. TOPAS academic version 7 was used for Rietveld refinement. The input file was constructed based on a ZIF-62 template (95) which was modified to accommodate the presence of the third linker type, dmbIm. The 2θ range was set to 0.5 – 3.6° for the initial refinement. The refinement was carried out using a 10$^{th}$ background polynomial, a 1/x background, as well as a simple axial asymmetry model to describe the peak asymmetry. Gaussian and Lorentzian crystal size and strain were used. After the fitting was optimised based on the initial parameters of the ZIF-62 structure, then the partial occupancy of the third linker was introduced in accordance with the ratio calculated from the S-NMR data. The refinement systematically underpredicted the <1 1 1>, <0 0 2>, and <1 0 2> plane. Two preferred orientation terms for the <1 1 1> and <1 0 2> planes were added. Further refinements were carried out by adding different solvent molecules into the cavities of the crystal, followed by an annealing procedure. However, the peaks associated with these crystal planes were unable to be described to a satisfactory degree, as can be seen in Figure 7.4.

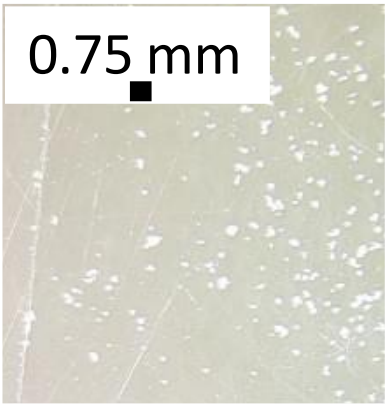


*Figure 7.3 optical image of ZIF-x sample.*

The inability to get a satisfactory refinement for the ZIF-x crystal can be caused by multiple possibilities. First, the crystalline sample may be contaminated with a crystal of a similar diffraction pattern, which is unable to be detected by powder diffraction. As there is presently no proposed structure for the hypothetical secondary phase, then it is not possible to introduce such a phase and get a reliable refinement. Second, the addition of the bIm and dmbIm linkers consistently reduced the intensity of these underpredicted peaks, hence it is possible that these linkers are present in the powder, but are more disordered than in the model used. Third, the solvent molecules in the pores are strongly disordered and have to be described by several partial occupancies. The final structure of the ZIF-x sample is thus still to be determined.

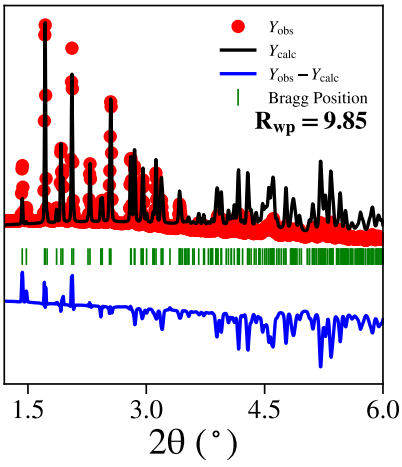


*Figure 7.4 Difference plot of crystalline ZIF-x refined via Rietveld refinement.*

In an attempt to reveal the nature of the bimodal melting behaviour, the ZIF-x sample was also measured and analysed by *in-situ* powder diffraction at several temperatures: RT, 200 °C, 289 °C, 376 °C and 400 °C. Above 400 °C, the diffraction pattern converted to a broad diffuse scattering peak, as can be seen in Figure 7.5 a). As can be noticed, there is no clear indication of two different crystal lattices melting at two different temperatures through the data, which inhibits further improvement of the Rietveld refinements in Figure 7.4. This further suggests that the structure might be a highly disordered *Pbca* space group sample, which causes the bimodal melting behaviour. However, an interesting finding is that the structure becomes significantly disordered at 376 °C and is completely amorphous above 400 °C. This transformation occurs significantly below the initial $T_m$ of 417 °C, however, the melting peak onset is quite difficult to determine exactly. Due to the loss of crystallinity, it appears that there is an amorphization occurring before 376 °C, which might act as a melting initiator. This amorphization prior to melting is a consistent observation with ZIF-62 and ZIF-4 by the work of Nozari et *al*. (201).

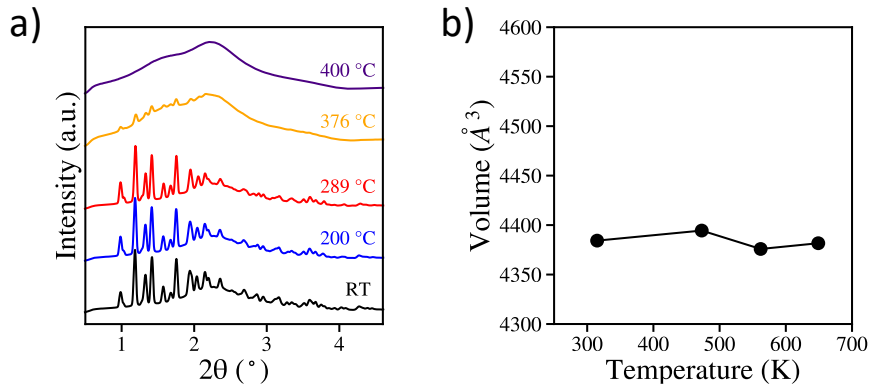


*Figure 7.5 a) in-situ PXRD study of ZIF-x at ambient temperature, 200 °C, 289 °C, 376 °C and 400 °C. b) lattice volume from LeBail refinement of ZIF-x as a function of temperature.*

LeBail refinements were carried out on each diffraction temperature. The initial structure was based on the same parameters as the Rietveld refinement carried out earlier. However, the goal where was the attain the lattice parameters, to correlate these with the thermal response. As can be seen in Figure 7.5 b), the thermal expansion is essentially negligible during the melting of these crystals. The addition of dmbIm into the crystal structure could likely increase the rigidity of the crystal, which could reduce the ability of the lattice to expand.

Figure 7.6 a) shows the pair distribution function (PDF) D(*r*) data of the crystalline ZIF-x being heated until melting, as well as the resultant glass. The intensity of the correlations in Figure 7.6 has been normalised, however, the correlation intensity decreases with increasing temperature, as is expected with the increased thermal energy of the atoms. As can be seen, minimal changes can be observed in the intra-tetrahedral correlations (peak 1-6 highlighted in Figure 7.6 a)) as temperatures increased. It should be noted that the PDF measurement at room temperature is noticeably different from that of the *in-situ* measurements. This is potentially caused by an experimental error, and the reproducibility of this result has yet to be verified.

Figure 7.6 b) reveals that all intermediate-range correlations are lost upon heating to 376 °C, which is expected as the crystallinity is lost in the X-ray diffractograms. Additionally, Figure 7.6 c) reveals little structural changes of the glass during heating to above $T_g$. The differences are small enough that they cannot presently be ascribed to any phenomenon like kinetic mobility.

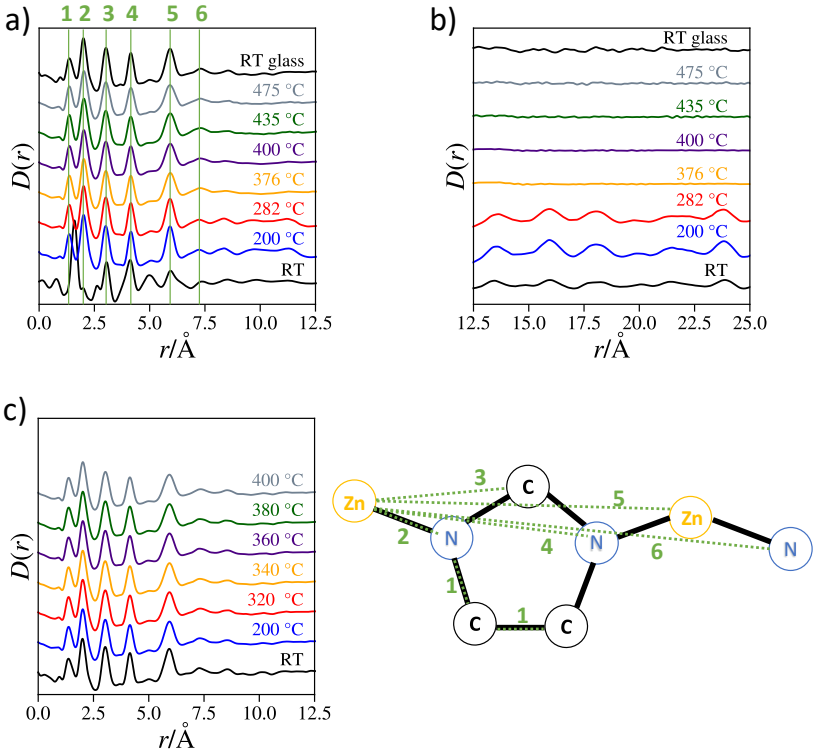


*Figure 7.6 in-situ PDF measurements of ZIF-x a) in-situ PDF of crystalline ZIF-x until glass formation, highlighting correlations from 0 to 12.5 Å c) in-situ PDF of ZIF-x glass. Correlations from 12.5 to 25 Å d) PDF measurements of ZIF-x glasses at different temperatures.*

To further investigate the intermediate structural changes during heating, Raman spectroscopy is employed. Figure 7.7 highlights the changes to the Raman spectrum in response to the temperature. The peak at 550 $cm^{-1}$ is ascribed to the $\nu_{ring}$ (stretching motion of the ring) as well as N-C-N out-of-plane bending ($\delta_{oop}$) (47,202). The peaks at ~636 $cm^{-1}$ are ascribed to ring torsion (203). The strong peak at 734 $cm^{-1}$ is ascribed to C-H $\delta_{oop}$ of the benzimidazole ring (47,202). At ~850 $cm^{-1}$ C-$H_{Im}$ $\delta_{oop}$ and $\delta_{ip}$ (in plane) at 975 is present (202). At ~1000 $cm^{-1}$ $\delta_{blm,ip}$ is observed, while ~1150 $cm^{-1}$ is stem from C-H $\delta_{ip}$ (47,202). The large peak at ~1283 $cm^{-1}$ is caused by the $\nu_{ring}$ and C-H $\delta_{ip}$. The at 1309 $cm^{-1}$ a peak associated with C-H $\delta_{ip}$ (202). The final major peaks at 1363 and 1422 are attributed to C=C $\nu$ (202). During heating, the peaks generally shift to a lower wavenumber, which is associated with increased bond length in the organic units (171). This is an expected finding, though the minimal change to the lattice volume suggests that the Zn-N bonds remain largely constant throughout heating.

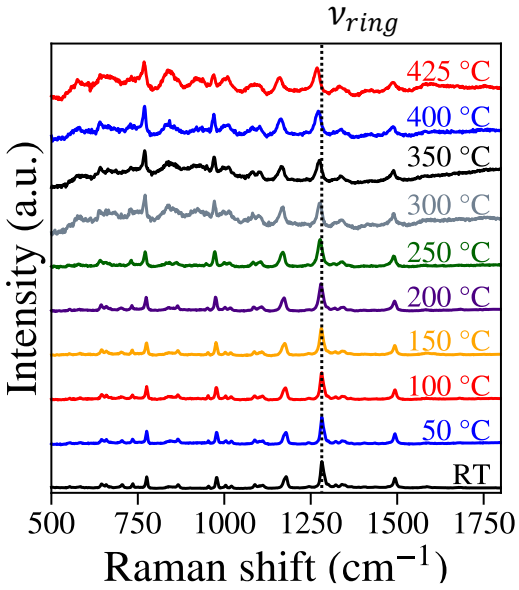


*Figure 7.7 VT-Raman spectroscopy analysis of ZIF-x.*

The use of Raman, PDF, powder refinement, and STA is unable to definitively attribute the bimodal $T_m$ and $T_g$ to any specific characteristic. However, the likely explanations are either that they stem from a highly disordered crystalline phase, or that two similar, crystalline phases are present in the sample. However, as the synthesis approach provides an extremely fine powder, it is not feasible to conduct single-crystal X-ray diffraction experiments with readily available equipment. However, the use of electron diffraction through TEM would provide the resolution required. Though the approach would be arduous, as the ZIFs are generally non-conductive, which can lead to the sample heating up and decomposing by charge effects and is generally avoided by low beam doses (204,205). Even in the case that thermal decomposition does not occur, then involuntary heating of the sample could significant complications.

What is more, the bimodal $T_m$ and $T_g$ behaviour is highly sensitive to preparation methods. This complicates the ability to grow larger single crystals, as the novel thermal behaviour is lost even with minor changes to the synthetic procedure. Even using the same synthesis parameters does not always lead to the crystalline powder having the same novel calorimetric response to heating. As the *in-situ* experiments yielded interesting results for this novel ZIF-x framework. The dmbIm-modified ZIF-62 samples from the published work in chapter 4, were also tested similarly.

# 8. IN-SITU STUDY OF DMBIM-MODIFIED ZIF-62 CRYSTALS

The dmbIm-modified ZIF-62 systems of chapter 4 were used for *in-situ* analysis. VT-Raman, *in-situ* synchrotron PXRD, and PDF were carried out. Rietveld refinement was attempted on the PXRD data, though similarly to chapter 7, the refinement resulted in a consistent underprediction of the first peaks on the diffraction patterns. LeBail refinement of ZIF-62 and 0.24-ZIF-62 revealed significantly different thermal expansion characteristics. ZIF-62 crystals exhibit a collapse in the lattice volume, while 0.24-ZIF-62 exhibits an increase in lattice volume as the temperature increases. Minimal intermediate-range structural changes were observed during heating and melting which would be able to address the difference in the thermal response of ZIF-62 and 0.24-ZIF-62.

## 8.1. EXPERIMENTAL WORK

**Synthesis:** The synthesis procedure used for this study is the same as in chapter 3 (146).

**Synchrotron *in-situ* PDF/PXRD:** PDF measurements were collected with the same method as outlined in 7.2.

**Synchrotron PXRD:** Same method approach as in 7.2.

**VT-Raman:** Variable temperature (VT) Raman was carried out on a Horiba Jobin Yvon (Japan) LabRAM HR800 with a semiconductor laser at 785 nm, using the same experimental procedure outlined in 7.2.

## 8.2. FINDINGS

*In-situ* Raman analysis of all samples was carried out with Figure 8.1 highlighting the differences between each sample. As expected, the similar chemical composition and crystal structure leave only minor differences. The peak at 550 $cm^{-1}$ is ascribed to the $\nu_{ring}$(stretching motion of the ring) as well as N-C-N out-of-plane bending ($\delta_{oop}$)(47,202). This peak is reduced in intensity, while a new peak at 575 $cm^{-1}$ emerges. The peaks at ~636 $cm^{-1}$ are ascribed to ring torsion (203). The strong peak at 734 $cm^{-1}$ for ZIF-62 is ascribed to C-H $\delta_{oop}$ of the benzimidazole ring (47,202), which goes to explain the discrepancy between ZIF-62 and 0.24-ZIF-62. At around 850 $cm^{-1}$ C-$H_{Im}$ $\delta_{oop}$ and $\delta_{ip}$ (in plane) at 975 is present (202). At ~1000 $cm^{-1}$ $\delta_{bIm,ip}$ is observed, while ~1150 $cm^{-1}$ originates from C-H $\delta_{ip}$ for bIm, which explains the absence of this peak in 0.24-ZIF-62 (47,202). The large peak at ~1283 $cm^{-1}$ is caused by the $\nu_{ring}$ and C-H $\delta_{ip}$. The at 1309 $cm^{-1}$ a peak associated with C-H $\delta_{ip}$ can be observed for ZIF-62, but is absent for 0.24-ZIF-62 (202). The final major peaks at 1363 and 1422 are attributed to C=C $\nu$ (202).

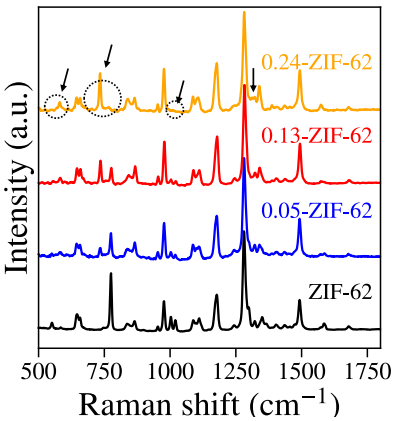


*Figure 8.1 Raman spectrum of ZIF-62 (black), 0.05-ZIF-62 (blue), 0.13-ZIF-62 (red), 0.24-ZIF-62 (orange). The black arrow indicates major differences between ZIF-62 and 0.24-ZIF-62.*

During the VT-Raman analysis (Figure 8.2), several findings were made. First, the signal quality deteriorated significantly above 400 °C, likely due to a combination of bond weakening (171) as well as thermal decomposition due to the insufficient protective atmosphere. As, dmbIm substitutes for bIm at increasing levels (0.13 and 0.24-ZIF-62) the stability is noticeably lower, as the signal-to-noise ratio is significantly lower at 400 °C than that of conventional ZIF-62. Another key finding is that the peaks shift to a lower wavenumber, as exemplified with the $\nu_{ring}$ at ~ 1283 cm$^{-1}$. This can be explained by the increase in thermal energy causing the bond-lengths of the organic ligands to increase (206).

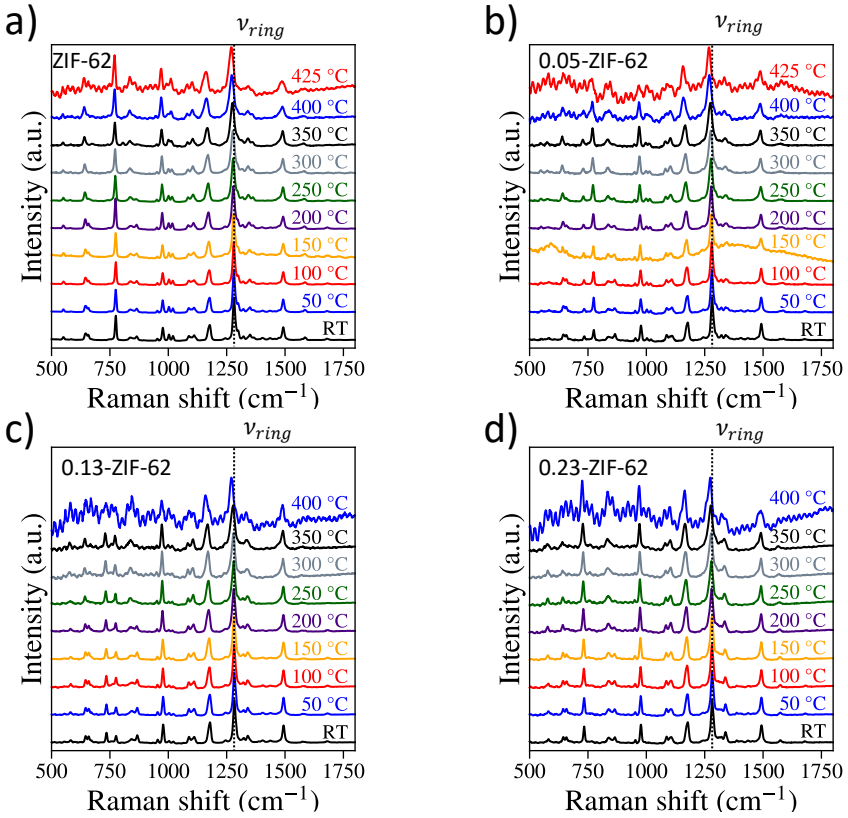


*Figure 8.2 VT-Raman spectroscopy analysis a) ZIF-62 b) 0.05-ZIF-62 c) 0.13-ZIF-62 d) 0.24-ZIF-62.*

Rietveld refinements from the diffraction data collected at Diamond were attempted in a similar fashion, as in 6.2.2. The refinement for un-modified ZIF-62 can be seen in Figure 8.3 a). The initial structure used is based on the work of Frentzel-Beyme et *al.* (95). As can be seen from the figure, the refinement process was quite successful with the ZIF-62 sample. However, The introduction of dmbIm into the structure consistently causes underprediction of initial peaks, as was the case with ZIF-x in Figure 7.4. Figure 8.3 b-d) highlights the same underprediction issue. With the same potential solutions to the inadequate refinements: the presence of a secondary phase that is difficult to detect with powder diffraction, distorted ligand positions, and disordered solvent positions. Hence it is presently not possible to provide a crystallographic structure of sufficient quality.

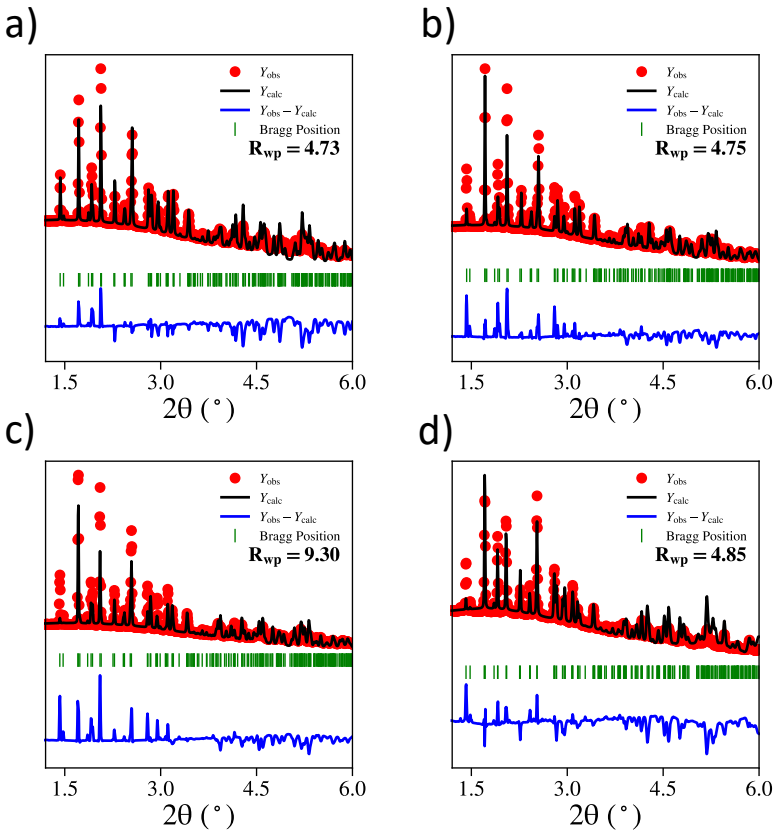


*Figure 8.3 Difference plots of dmbIm-modified ZIF-62 a) ZIF-62 b) 0.05-ZIF-62 c) 0.13-ZIF-62 d) 0.24-ZIF-62.*

Similarly to ZIF-x, ZIF-62 and 0.24-ZIF-62 were analysed by *in-situ* powder diffraction. Figure 8.4 a) outlines the PXRD of the ZIF-62 sample as it is being heated. Between 150 °C and 300 °C, the crystal structure is largely retained, however, there is a noticeable increase in the background when compared to the RT sample, as expected by the increased thermal motion. The diffraction peaks suddenly develop into a large diffuse scattering peak once the temperature reaches 400 °C. Like with ZIF-x, the structure is getting disordered by a mechanism separate from $T_m$ observed by DSC in chapter 3. Interestingly, 0.24-ZIF-62 retains a small degree of crystallinity at 400 °C, which is directly tied to the higher $T_m$.

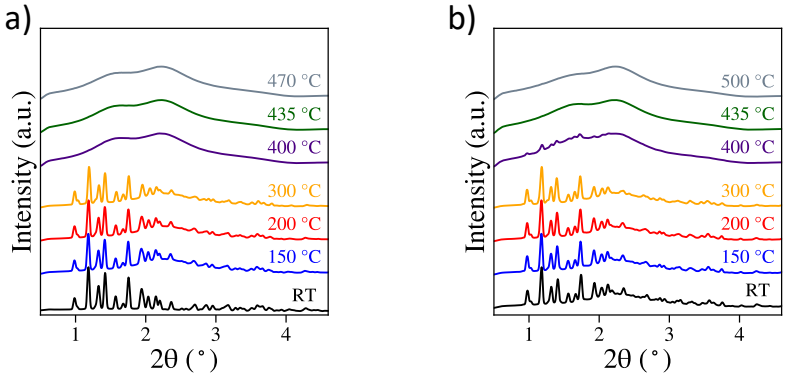


*Figure 8.4 in-situ powder X-ray diffraction data. a) ZIF-62 crystals being heated to 470 °C b) 0.24-ZIF-62 crystals heated to 500 °C.*

As there is no indication for these crystals to have any secondary crystalline phases (146). LeBail refinements were conducted on the *in-situ* ZIF-62 and 0.24-ZIF-62 samples. 0.05- and 0.13-ZIF-62 samples were not analysed *in-situ* due to time constraints associated with the beamtime. The thermal response of the lattice volume of ZIF-62 and 0.24-ZIF-62 can be seen in Figure 8.5. remarkably, the effects are opposite, ZIF-62 decreases in lattice volume, while 0.24-ZIF-62 increases in lattice volume. And what is more, the effects are significantly strong, when compared to that observed in Figure 7.5 b), which displays a mostly unchanging lattice volume. Usually, the lattice volume is expected to increase with temperature (18,207), and as such, the effect of ZIF-62 is likely caused by the framework being less rigid. This is corroborated by the desolvation observed in chapter 3 (146). The structure relaxes during the release of the solvent, as DMF is the structure-directing agent (132), and without it, the lattice volume decrease as a consequence of the fairly weak Zn-N coordination bonds. Despite the findings of Figure 8.5 intuitively contradicting that of Figure 8.2, these findings can be simultaneously valid. The bond lengths of the organic linkers do not necessitate an increase in lattice volume (132).

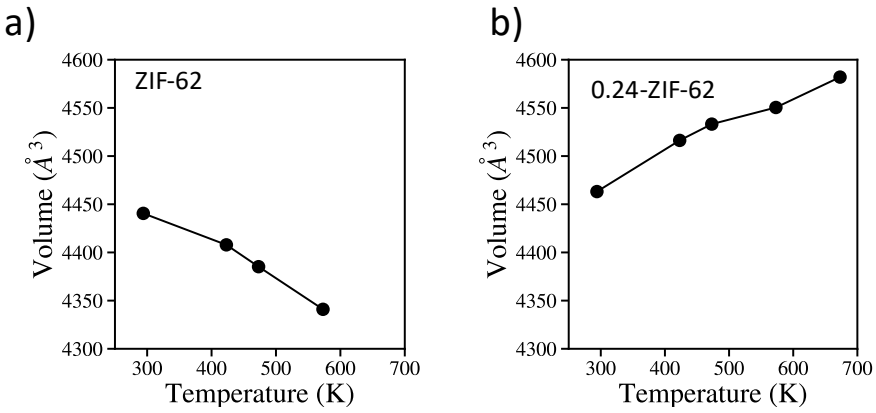


*Figure 8.5 Lattice volume vs Temperature plot. a) unmodified ZIF-62 crystals b) 0.24-ZIF-62 crystals.*

Interestingly, 0.24-ZIF-62, unlike ZIF-62, increases in lattice volume as the temperature increases. This can partially be explained by the solvent occupation as seen in the STA measurements in chapter 3 (146). However, due to the electron-donating methyl groups as well as their steric effect the structure has likely become more rigid due to stronger Zn-N bonds. This combined with the lowered topological degree of atomic freedom caused by the methyl groups, stabilises the framework against thermal relaxation.

PDF data from the dmbIm modified ZIF-62 (chapter 3) can be seen in Figure 8.6. Each sample has been normalised by the correlation intensity maximum, meaning that any potential discrepancies in measured intensities are not apparent in the figures. The overall short-range correlations are generally comparable between samples. However, minor peak position shifts are appearing, e.g., for the sixth correlation peak in Figure 8.6 a), a shift to lower radii is observed for higher dmbIm substitutions. When comparing ZIF-62 and 0.24-ZIF-62, the peak maxima are slightly off the reading aid line. This effect can be caused by several factors, however, given that the lattice parameters consistently increase with dmbIm substitution, this peak shift is unlikely to originate from the sixth correlation shown in the imidazolate molecule in Figure 8.6.

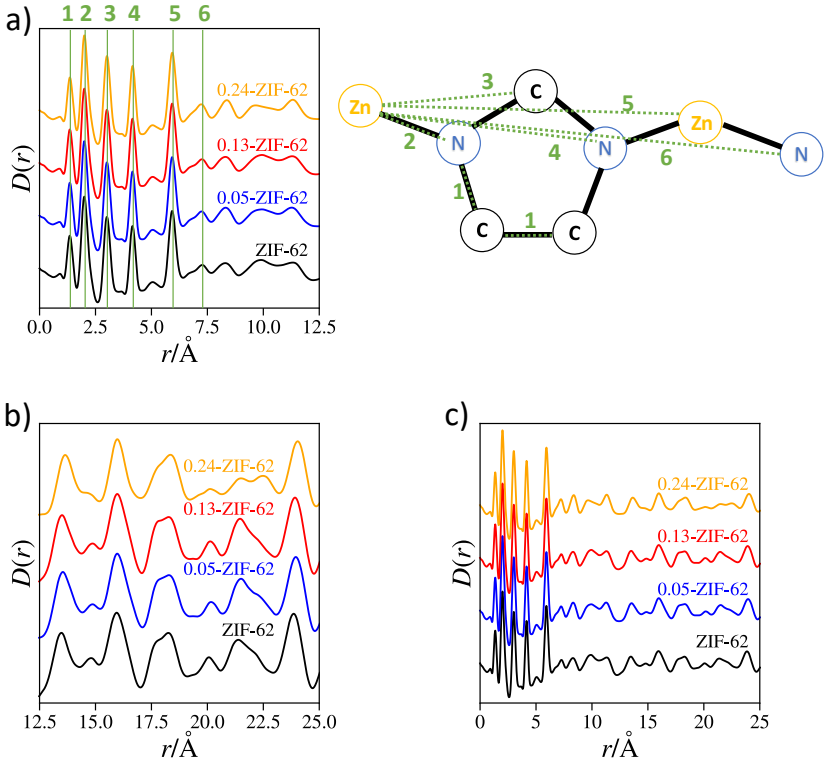


*Figure 8.6 Pair-distribution function plots of ZIF-62 and dmbIm-modified ZIF-62 samples a) 0 Å to 12.5 Å, with a reference imidazolate schematic to account for the first 6 major peaks* (102) *b) 12.5 Å to 25 Å c) 0 Å to 25 Å.*

However, given that two methyl groups have been added to the 5 and 6 positions in the benzimidazole, it is plausible that several new correlations facilitated this shift. Indeed, the distance between a zinc molecule and carbon on the far methyl group (Figure 8.7) is approximately 7.36 Å in the structure models used in the attempted Rietveld refinements. At higher correlation radii, several slight differences between ZIF-62 and 0.24-ZIF-62 are observed. At ~14.8 Å there is a minor peak which changes shape. Similarly, the peak at 20 Å changes significantly. The broad peak at ~ 20.5-22.6 Å changes from a broad peak with significant tailing to higher correlation radii, to a bimodal peak with two distinct correlation maxima. These features indicate that the change from dmbIm causes significant intermediate structural changes, while the crystal structure appears to be retained. With only minor short-range differences being observed, the addition of the two methyl groups appears to predominantly change Zn-N bond characteristics as well as intermediate-long range structure.

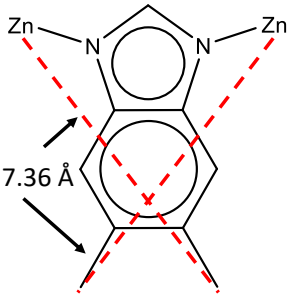


*Figure 8.7 Schematic illustrating the zinc to methyl correlation distance of 7.36 Å.*

The *in-situ* PDF of ZIF-62 and 0.24-ZIF-62 provided further insight into the melting mechanism. Figure 8.8 a-b) highlights the structural response of ZIF-62 to heating and subsequent quenching into a glass. Peak 1-6 remains largely similar during the melt-quench process of ZIF-62. Several changes are observed: two correlation peaks between 0 and 1 Å appear and increase with the increase in temperature until a temperature of 400 °C, by which these correlations decrease. Intermediate correlations (8-20 Å) are undetectable at 400 °C, signifying loss for long-range periodicity, following the PXRD data (Figure 8.4). In Figure 8.8 c-d) a similar trend is observed, however, there is a small discrepancy between the PDF data and the PXRD data in Figure 8.4, as crystallinity is still detectable at 400 °C, while intermediate-range correlations are not detectable in Figure 8.8 d). The root of this loss of structure is potentially due to the initiation of the scission and renewal of bonds. Several reasons can explain why the structural transformation is not visible in the DSC. One is that the transformation is so slight that it is hard to detect on a DSC, second, and perhaps

more likely, is that the structural change is masked by the solvent release signal, as seen with ZIF-x and with the dmbIm-modified ZIF-62 samples (146). Despite the significantly different thermal expansion of the lattice, as well as the differences in $T_m$ and $T_g$, limited differentiation can be made between ZIF-62 and 0.24-ZIF-62 through *in-situ* PDF.

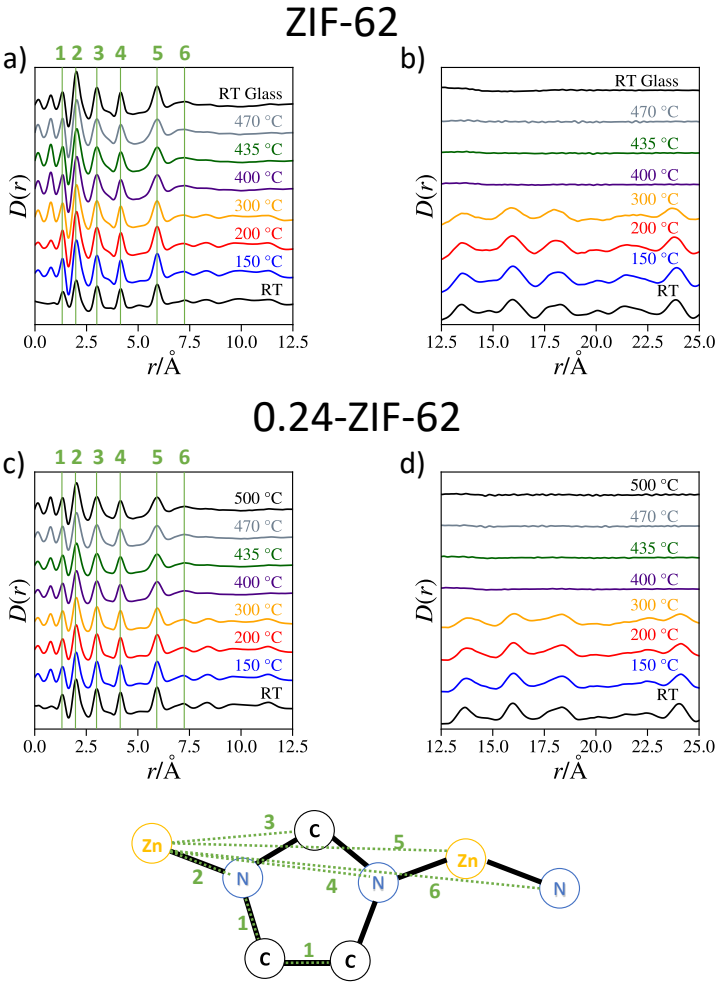


*Figure 8.8 8 in-situ PDF measurements of a) ZIF-62 crystals heated from room temperature to 470 °C, including the resultant glass upon cooling, with correlations from 0 Å to 12.5 Å b) ZIF-62 from RT to 470 °C including glass with correlations from 12.5 Å to 25 Å c) 0.24-ZIF-62 crystals heated from RT to 500 °C, with correlations from 0 Å to 12.5 Å d) 0.24-ZIF-62 crystals heated from RT to 500, with correlations from 12.5 Å to 25 Å.*

Overall, the *in-situ* studies in chapter 7 reveal minimal structural changes to the tetrahedral environment (1.5-8 Å), as observed by the *in-situ* PDF measurements of

ZIF-x. Similarly, the intermediate range structure (8-20 Å) reveals only moderate changes when substituting dmbIm for bIm, while also showing minimal changes to the structure when substituting dmbIm for bIm. It appears as though minimal structural changes in these length scales, meaning, that it is likely that structure effects as shorter range and longer ranges are likely to affect the melting and glass transition to a much larger extent, as seen in chapter 3 (146), the lattice volume correlates well with changes in $T_m$ and $T_g$. The crystal structure of a compound is traditionally influential in the thermodynamic responses of different allotropes e.g. with carbon (208).

However, perhaps more importantly, the metal-linker coordination environment appears to be directly tied to the melting and vitrification of MOFs (17). Chapter 4 provided the first experimental evidence for the melting of ZIFs being driven by the scission and renewal of Zn-N bonds. In conjunction with chapters 4 and 6, it is clear, that small variations to the coordination bonds have profound effects on the thermodynamic and kinetic characteristics. The electron-donating nature of 5,6-dimethylbenzimidazole can stabilise the ZIF-62 network and even increase $T_m$, which, is contradictory to the findings of Bumstead et al. (104). The proposed destabilising effect of disorder caused by multiple linkers is offset by strengthening the Zn-N bonds. In accordance with the findings of chapter 5 (17), stronger Zn-N bonds would result in lower meltability. The bond strength of these could either be investigated by electron density analysis, like the work of Sarkar et al. (171) or by far-IR spectroscopy similar to Hou et al. (102). The proposed effect of the electron-donating nature of dmbIm is an additional parallel to the mixed metal node effect discussed in chapters 4 and 6.1. specifically, the nature of the chemical metal-to-ligand bond has a profound effect on the specific melting characteristics.

## 8.3. SYNTHESIS OF LARGE CRYSTALLINE SAMPLES

During the synthesis of dmbIm-modified ZIF-62, the synthesis of large, multi-millimetre scale crystals occurred. Not all samples presented large crystals. Figure 8.9 presents crystals recovered from a 0.05, 0.13, and 0.24-ZIF-62 synthesis. These crystals are uncharacteristically large for the conventional synthesis approach. Crystals of this size would potentially be able to be analysed via X-ray single-crystal diffraction, assuming the crystal quality is sufficiently high. As such, this finding provides a potential solution to the insufficient Rietveld refinement quality. However, more interestingly, is the nature of the formation of these large crystals. If it is possible to reproduce the conditions which enabled the synthesis of large crystals, the production of large ZIF-x crystals would plausible as well. Presently several potential reasons need to be explored, i.e., the nature of the surface of the reaction vessel, and the preparation time for the reaction solution are the current primary candidates.

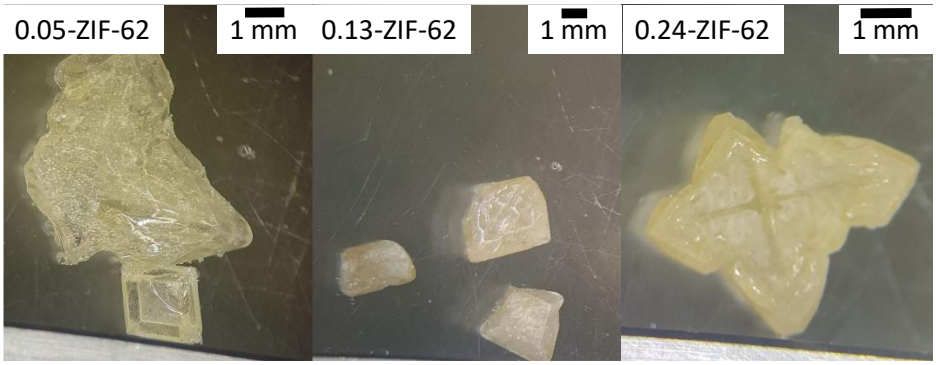


*Figure 8.9 optical image of large dmbIm-modified ZIF-62 crystals synthesised.*

# 9. CONCLUSIONS AND PERSPECTIVES

The title of the thesis is “Impact of Local structural Characteristics on Glass-formation in Metal-organic Frameworks”. In this aspect, this thesis provides novel insight into the melting mechanism of a range of zeolitic imidazolate frameworks. The solid-state NMR data support the currently proposed mechanism for melting metal-organic frameworks. The observed disappearance of the discrete ordered, zinc sites in ZIF crystals and the emergence of a single broad zinc signal described by a continuous distribution of coupling constants supports the notion that metal-to-ligand coordination bonds must be severed and reformed for melting to occur.

Knowing that the metal coordination bond is key to the melting mechanism plays a vital role in explaining the mixed metal node effect observed when systematically substituting a metal node in a framework for another. The characteristic drop in $T_m$ of ZIF-62 when substituting cobalt for zinc as well as the sharp drop observed in Cu/Zn-ZIF-4 is likely caused by electronic effects occurring at the metal-to-ligand bonds. This hypothesis is substantiated by the structure evolution in the metal coordination environments, as observed by solid-state NMR. Introducing a small quantity of a metal node with a higher electron affinity will shift the electron distribution in the aromatic imidazole-based rings towards the metal dopant, hence weakening the other coordination bond. By introducing a small number of weakened coordination bonds, the initiation of melting is enabled to occur at lower temperatures, i.e., increasing MA and by extension GFQ. The severing of the small number of weakened bonds then lowers the connectivity of the framework, which provides more thermal motion for the rest of the network to continue the scission and renewal of the metal-to-ligand coordination bonds.

In addition, this thesis has demonstrated the effects on the long-range structure by substituting dmbIm for bIm in ZIF-62 networks and what implications this has on the melting and vitrification of the systems. The lattice parameters of the dmbIm-modified ZIF-62 crystals correlate well with both $T_g$ and $T_m$. The crystal structure compensates for the introduction of bulky linkers by expanding the crystal lattice. The increase in both $T_m$ and $T_g$ can be ascribed to the steric effects of the bulky linkers, as this reduces the mobility of the linkers. Secondly, the electron-donating effect of the methyl groups is likely to provide a significant effect on the melting mechanism. By donating electrons to the aromatic ring, the coordination bonds between the zinc and ligands get strengthened. In tandem with the mixed metal node effect, the strengthening of the coordination bond is likely to increase the melting temperature significantly.

Additionally, the steric effects of the dmbIm units demonstrate a strong effect on the structure of the quenched glasses. The change in isobaric heat capacity ($\Delta C_p$) decreases consistently with increasing dmbIm/bIm ratio. This decrease causes the glass to be higher in the potential energy landscape, i.e. having a structure more closely related to that of the supercooled liquid. As observed with Cu-ZIF-4, the substitution of metal ions appear to have a minimal effect on the glass transition behaviour, while the introduction of dmbIm increases it. The sluggish diffusion of the bulky linker explains this phenomenon.

The *in-situ* study of the intermediate-range structure provided little to elucidate the melting mechanism. PDF and powder diffraction experiments revealed that the investigated ZIF structures become amorphous before melting. Interestingly, this is not observed clearly in the STA measurements. Despite the curious nature of this amorphization, the intermediate-range structures (8-20 Å) provide little information that is uniquely derived from the measurements. The inability to resolve any significant short-range structural evolution from the PDF, is not unsurprising, as the nature of the method does not discriminate chemical bonds of similar correlation radii. Therefore the subtle, though important changes observed in the zinc tetrahedral units during melting are not easily detected in PDF measurements, while the highly selective nature of $^{67}$Zn-NMR is a much more useful tool for short-range structure analysis. In contrast, the *in-situ* XRD studies revealed a fundamental change in the melting mechanism between ZIF-62 and fully dmbIm substituted ZIF-62. The incorporation of the bulky electron donating methyl groups causes the thermal expansion to change from a negative slope to a positive slope, i.e., ZIF-62 with better GFQ becomes more dense during heating, while 0.24-ZIF-62 expands during heating. This finding suggests that higher MA might be tied to frameworks which collapses during heating.

The overall findings of this thesis can therefore be summarized into the following: glass forming quality of ZIFs appears to be dictated to some extent by crystallographic characteristics, and predominantly by the nature of the metal-linker coordination bond. The mixed metal node effect and electron inductive effects of functional groups are the major tools for the manipulation of $T_m$ of ZIFs. The effect of the steric functional groups appears to consistently increase the $T_g$, hence it is likely that $T_g$ and $T_m$ can be manipulated independently of each other, thereby producing ZIF glasses with a consistently high GFA.

The findings of this thesis provide a solid foundation for future research in the field of MOF glasses. First, the validity of the proposed mechanism of the mixed metal node effect should be analysed by electron density studies. This could validate if the electron could get significantly distorted in the imidazole-based linkers. Two potential methods of study would be synchrotron X-ray diffraction of the singly crystals and computational simulation of the electron clouds. If validated, the proposed mechanism would have profound potential in future experimental and computational research.

Further understanding of the mixed metal node effect, to such an extent that can mathematically describe its structural effect would be critically important for the improvement of the current computational methods to approximate the melting temperature of ZIF during simulations. This could be by revisions to the currently used melting criteria (Lindemann criterion), or by the development of a novel measure for melting.

Similarly, combining the mixed metal node effect and the effect of introducing functional groups to the organic linkers should be investigated. By systematic variations in the ZIF compositions, it would be possible to determine if the design of MOF glass formers with independent variations of $T_m$ and $T_g$ is possible.

The aforementioned prospects are much broader in scope than this thesis. Unanswered questions directly related to this project would pertain to the following questions.

What is the cause of the large dmbIm-modified ZIF-62 crystals formed? The reproducibility should be tested to determine what synthetic parameter drives the synthesis of such large crystals.

What is the exact crystal structure of dmbIm-ZIF-62 and ZIF-x? The use of single-crystal X-ray diffraction could elucidate the nature of the dmbIm-ZIF-62 crystals. While single crystal X-ray diffraction is not feasible for ZIF-x, electron diffraction experiments are a potential avenue to test, as this would be able to detect differences in crystal structures at exceedingly small ranges.

What is the origin of the novel linker detected in Co/Zn-ZIF-new? By understanding the chemical structure (and crystal structure) of this novel framework, further development of the mixed metal node effect can be made. Especially by revealing the cause of the larger effect on $T_m$ and $T_g$ displayed by Co/Zn-ZIF-new when compared to Co/Zn-ZIF-62.

In addition to these, further solid-state NMR experimentation would provide significant possibilities for furthering the current understanding of the structural development of ZIFs during glass formation. By using labelled isotopes, such as $^{13}C$ and $^{15}N$ to make 2D $^{67}Zn$ NMR studies.

In summary, this thesis provides significant and new findings relevant to MOF glass research. The findings add to the current body of literature and help fill some of the current gaps in knowledge. These findings can aid in the future predictive design of novel MOF glass formers.

# 10. LITERATURE LIST


1. Shelby JE. Introduction to Glass Science and Technology. 2nd ed. Introduction to Glass Science and Technology. Royal Society of Chemistry; 2005. 291 p.
2. Chartier Thierry. Optical Fibers. In: Musgraves JD, Hu J, Calvez L, editors. Handbook of glass. Springer; 2019. p. 1851.
3. Clupper DC, Hench LL. Crystallization kinetics of tape cast bioactive glass 45S5. J Non Cryst Solids. 2003 Apr 1;318(1–2):43–8.
4. Angell CA. Formation of glasses from liquids and biopolymers. Science (1979). 1995;267(5206):1924–35.
5. Greaves GN, Sen S. Inorganic glasses, glass-forming liquids and amorphizing solids. Adv Phys. 2007 Jan;56(1):1–166.
6. Klement W, Willens RH, Duwez P. Non-crystalline Structure in Solidified Gold–Silicon Alloys. Nature 1960 187:4740. 1960;187(4740):869–70.
7. Bennett TD, Tan JC, Yue Y, Baxter E, Ducati C, Terrill NJ, et al. Hybrid glasses from strong and fragile metal-organic framework liquids. Nat Commun. 2015;6:1–7.
8. Zachariasen WH. The atomic arrangement in glass. J Am Chem Soc. 1932;54(10):3841–51.
9. Anderson PW. Through the Glass Lightly. Science (1979). 1995 Mar 17;267(5204):1615–6.
10. Furukawa H, Ko N, Go YB, Aratani N, Choi SB, Choi E, et al. Ultrahigh porosity in metal-organic frameworks. Science (1979). 2010 Jul 23;329(5990):424–8.
11. Wang Y, Jin H, Ma Q, Mo K, Mao H, Feldhoff A, et al. A MOF Glass Membrane for Gas Separation. Angewandte Chemie - International Edition. 2020;51(11):4365–9.
12. Fonseca J, Gong T, Jiao L, Jiang HL. Metal–organic frameworks (MOFs) beyond crystallinity: amorphous MOFs, MOF liquids and MOF glasses. J Mater Chem A Mater. 2021 May 4;9(17):10562–611.
13. Stock N, Biswas S. Synthesis of metal-organic frameworks (MOFs): Routes to various MOF topologies, morphologies, and composites. Chem Rev. 2012;112(2):933–69.
14. Wang Q, Astruc D. State of the Art and Prospects in Metal-Organic Framework (MOF)-Based and MOF-Derived Nanocatalysis. Chem Rev. 2020 Jan 22;120(2):1438–511.
15. Gao C, Jiang Z, Qi S, Wang P, Rosgaard Jensen L, Johansen M, et al. Metal-Organic Framework Glass Anode with an Exceptional Cycling-Induced Capacity Enhancement for Lithium-Ion Batteries. Advanced Materials. 2022 Mar 1;34(10):2110048.
16. Nandasiri MI, Jambovane SR, McGrail BP, Schaef HT, Nune SK. Adsorption, separation, and catalytic properties of densified metal-organic frameworks. Coord Chem Rev. 2016;311:38–52.

17. Madsen RSK, Qiao A, Sen J, Hung I, Chen K, Gan Z, et al. Ultrahigh-field 67Zn NMR reveals short-range disorder in zeolitic imidazolate framework glasses. Science (1979). 2020;367(6485):1473–6.
18. Dubbeldam D, Walton KS, Ellis DE, Snurr RQ. Exceptional negative thermal expansion in isoreticular metal-organic frameworks. Angewandte Chemie - International Edition. 2007;46(24):4496–9.
19. Bennett TD, Horike S. Liquid, glass and amorphous solid states of coordination polymers and metal–organic frameworks. Nat Rev Mater. 2018;3(11):431–40.
20. Hayashi H, Côté AP, Furukawa H, O'Keeffe M, Yaghi OM. Zeolite A imidazolate frameworks. Nat Mater. 2007;6(7):501–6.
21. Zhou C, Longley L, Krajnc A, Smales GJ, Qiao A, Erucar I, et al. Metal-organic framework glasses with permanent accessible porosity. Nat Commun. 2018;9(1):1–9.
22. Stepniewska M, Januchta K, Zhou C, Qiao A, Smedskjaer MM, Yue Y. Observation of indentation-induced shear bands in a metal − organic framework glass. PNAS. 2020;117(19):10149–54.
23. To T, Sørensen SS, Stepniewska M, Qiao A, Jensen LR, Bauchy M, et al. Fracture toughness of a metal–organic framework glass. Nat Commun. 2020;11(1):1–9.
24. Qiao A, Bennett TD, Tao H, Krajnc A, Mali G, Doherty CM, et al. A metal-organic framework with ultrahigh glass-forming ability. Sci Adv. 2018;4(3).
25. Hou J, Ríos Gómez ML, Krajnc A, McCaul A, Li S, Bumstead AM, et al. Halogenated Metal-Organic Framework Glasses and Liquids. J Am Chem Soc. 2020;142(8):3880–90.
26. Li H, Eddaoudi M, O'Keeffe M, Yaghi OM. Design and synthesis of an exceptionally stable and highly. Nature. 1999;402(November):276–9.
27. Ali MohamedA, Ren J, Zhao T, Liu X, Hua Y, Yue Y, et al. Broad Mid-Infrared Luminescence in a Metal–Organic Framework Glass. ACS Omega. 2019;4(7):12081–7.
28. Qiao A, Tao H, Carson MP, Aldrich SW, Thirion LM, Bennett TD, et al. Optical properties of a melt-quenched metal–organic framework glass. Opt Lett. 2019;44(7):1623.
29. Hughes JT, Bennett TD, Cheetham AK, Navrotsky A. Thermochemistry of zeolitic imidazolate frameworks of varying porosity. J Am Chem Soc. 2013;135(2):598–601.
30. Batten SR, Champness NR, Chen XM, Garcia-Martinez J, Kitagawa S, Öhrström L, et al. Terminology of metal-organic frameworks and coordination polymers (IUPAC recommendations 2013). Pure and Applied Chemistry. 2013 Jul 31;85(8):1715–24.
31. Öhrström L. Let's Talk about MOFs—Topology and Terminology of Metal-Organic Frameworks and Why We Need Them. Crystals 2015, Vol 5, Pages 154-162. 2015 Feb 16;5(1):154–62.
32. Atkins, P. W., de Paula J. KJ. Physical Chemistry, 11th ed. Oxford University Press, Oxford. 2017;944.
33. Sands D. Crystals and lattices. Introduction to crystallography. 1969;1–12.

34. Prince E. INTERNATIONAL TABLES FOR CRYSTALLOGRAPHY Volume C. 3rd ed. King SE, Ashcroft NJ, editors. Kluwer Academic Publishers; 2004.
35. Banerjee R, Phan A, Wang B, Knobler C, Furukawa H, O'Keeffe M, et al. High-Throughput Synthesis of Zeolitic. Science . 2008;319(February):939–43.
36. Park KS, Ni Z, Côté AP, Choi JY, Huang R, Uribe-Romo FJ, et al. Exceptional chemical and thermal stability of zeolitic imidazolate frameworks. Proc Natl Acad Sci U S A. 2006;103(27):10186–91.
37. Ma Y, Han X, Xu S, Wang Z, Li W, da Silva I, et al. Atomically Dispersed Copper Sites in a Metal-Organic Framework for Reduction of Nitrogen Dioxide. J Am Chem Soc. 2021 Jul 28;143(29):10977–85.
38. Wang T, Kim HK, Liu Y, Li W, Griffiths JT, Wu Y, et al. Bottom-up Formation of Carbon-Based Structures with MultilevelHierarchy from MOF−Guest Polyhedra. J Am Chem Soc. 2018;140:6130–6.
39. Levchenko Volodymyr A., Melanie Siah Huey-San, Øien-Ødegaard Sigurd, Kaur Gurpreet, Fiksdahl Anne, Tilset Mats. Catalytic studies of cyclometalated gold(III) complexes and their related UiO-67 MOF. Molecular Catalysis. 2020 Aug 1;492:111009.
40. Lebedev OI, Millange F, Serre C, van Tendeloo G, Férey G. First Direct Imaging of Giant Pores of the Metal-Organic Framework MIL-101. Chem Mater. 2005;15:6525–7.
41. Zorainy MY, Gar Alalm M, Kaliaguine S, Boffito DC. Revisiting the MIL-101 metal–organic framework: design, synthesis, modifications, advances, and recent applications. J Mater Chem A Mater. 2021 Oct 12;9(39):22159–217.
42. Volkringer C, Loiseau T. A new indium metal-organic 3D framework with 1,3,5-benzenetricarboxylate, MIL-96 (In), containing μ3-oxo-centered trinuclear units and a hexagonal 18-ring network. Mater Res Bull. 2006 May 25;41(5):948–54.
43. Frentzel-Beyme L, Kloß M, Kolodzeiski P, Pallach R, Henke S. Meltable Mixed-Linker Zeolitic Imidazolate Frameworks and Their Microporous Glasses: From Melting Point Engineering to Selective Hydrocarbon Sorption. J Am Chem Soc. 2019;141(31):12362–71.
44. Widmer RN, Lampronti GI, Chibani S, Wilson CW, Anzellini S, Farsang S, et al. Rich Polymorphism of a Metal-Organic Framework in Pressure-Temperature Space. J Am Chem Soc. 2019 Jun 12;141(23):9330–7.
45. Gandara-Loe J, Bueno-Perez R, Missyul A, Fairen-Jimenez D, Silvestre-Albero J. Molecular Sieving Properties of Nanoporous Mixed-Linker ZIF-62: Associated Structural Changes upon Gas Adsorption Application. ACS Appl Nano Mater. 2021 Apr 23;4(4):3519–28.
46. Wang Y, Jin H, Ma Q, Mo K, Mao H, Feldhoff A, et al. A MOF Glass Membrane for Gas Separation. Angewandte Chemie - International Edition. 2020;59(11):4365–9.
47. Zhao P, Lampronti GI, Lloyd GO, Wharmby MT, Facq S, Cheetham AK, et al. Phase transitions in zeolitic imidazolate framework 7: The importance of

framework flexibility and guest-induced instability. Chemistry of Materials. 2014;26(5):1767–9.
48. Morris W, Stevens CJ, Taylor RE, Dybowski C, Yaghi OM, Garcia-Garibay MA. NMR and X-ray study revealing the rigidity of zeolitic imidazolate frameworks. Journal of Physical Chemistry C. 2012 Jun 21;116(24):13307–12.
49. Byrappa K, Yoshimura M. Handbook of Hydrothermal Technology A Technology for Crystal Growth and Materials Processing. William Andrew; 2001. 870 p.
50. Rabenau A. The Role of Hydrothermal Synthesis in Preparative Chemistry. Angewandte Chemie International Edition in English. 1985;24(12):1026–40.
51. Safaei M, Foroughi MM, Ebrahimpoor N, Jahani S, Omidi A, Khatami M. A review on metal-organic frameworks: Synthesis and applications. TrAC - Trends in Analytical Chemistry. 2019;118:401–25.
52. Klinowski J, Almeida Paz FA, Silva P, Rocha J. Microwave-assisted synthesis of metal-organic frameworks. Dalton Transactions. 2011;40(2):321–30.
53. Sud D, Kaur G. A comprehensive review on synthetic approaches for metal-organic frameworks: From traditional solvothermal to greener protocols. Polyhedron. 2021;193:114897.
54. Varsha M. V., Nageswaran Gomathi. Review-Direct Electrochemical Synthesis of Metal Organic Frameworks. Journal of The Electrochemical Society . 2020;167.
55. Mueller U, Schubert M, Teich F, Puetter H, Schierle-Arndt K, Pastré J. Metal-organic frameworks-prospective industrial applications{. 2005;
56. Li M, Dincă M. Selective formation of biphasic thin films of metal–organic frameworks by potential-controlled cathodic electrodeposition. Chem Sci. 2013 Nov 26;5(1):107–11.
57. Ortiz AU, Boutin A, Fuchs AH, Coudert FX. Investigating the pressure-induced amorphization of zeolitic imidazolate framework ZIF-8: Mechanical instability due to shear mode softening. Journal of Physical Chemistry Letters. 2013 Jun 6;4(11):1861–5.
58. Safaei M, Foroughi MM, Ebrahimpoor N, Jahani S, Omidi A, Khatami M. A review on metal-organic frameworks: Synthesis and applications. TrAC - Trends in Analytical Chemistry. 2019 Sep 1;118:401–25.
59. Boldyrev V v, Tkáčová K. Mechanochemistry of Solids: Past, Present, and Prospects. Journal of Materials Synthesis and Processing. 2000;8:121–32.
60. Safaei M, Foroughi MM, Ebrahimpoor N, Jahani S, Omidi A, Khatami M. A review on metal-organic frameworks: Synthesis and applications. TrAC - Trends in Analytical Chemistry. 2019;118:401–25. Available from: https://doi.org/10.1016/j.trac.2019.06.007
61. Lv D, Chen Y, Li Y, Shi R, Wu H, Sun X, et al. Efficient Mechanochemical Synthesis of MOF-5 for Linear Alkanes Adsorption. J Chem Eng Data. 2017 Jul 13;62(7):2030–6.
62. Rouquerol J, Avnir D, Fairbridge CW, Everett DH, Haynes JM, Pernicone N, et al. Recommendations for the characterization of porous solids (Technical Report). Pure and Applied Chemistry. 1994 Jan 1;66(8):1739–58.

63. Furukawa H, Cordova KE, O'Keeffe M, Yaghi OM. The chemistry and applications of metal-organic frameworks. Science (1979). 2013;341(6149).
64. Yaghi OM, O'Keeffe M, Ockwig NW, Chae HK, Eddaoudi M, Jaheon Kim. Reticular synthesis and the design of new materials. Nature. 2003;423:705–14.
65. Kitagawa S, Kitaura R, Noro SI. Functional Porous Coordination Polymers. Angewandte Chemie International Edition. 2004 Apr 26;43(18):2334–75.
66. Kim CR, Uemura T, Kitagawa S. Inorganic nanoparticles in porous coordination polymers. Chem Soc Rev. 2016 Jul 11;45(14):3828–45.
67. Hu Z, Deibert BJ, Li J. Luminescent metal-organic frameworks for chemical sensing and explosive detection. Chem Soc Rev. 2014;43(16):5815–40.
68. Maksimchuk N v., Zalomaeva O v., Skobelev IY, Kovalenko KA, Fedin VP, Kholdeeva OA. Metalorganic frameworks of the MIL-101 family as heterogeneous single-site catalysts. Proceedings of the Royal Society A: Mathematical, Physical and Engineering Sciences. 2012 Jul 8;468(2143):2017–34.
69. Horike S, Dincă M, Tamaki K, Long JR. Size-selective Lewis acid catalysis in a microporous metal-organic framework with exposed Mn2+ coordination sites. J Am Chem Soc. 2008 May 7;130(18):5854–5.
70. Schlichte K, Kratzke T, Kaskel S. Improved synthesis, thermal stability and catalytic properties of the metal-organic framework compound Cu3(BTC)2. Microporous and Mesoporous Materials. 2004 Aug 6;73(1–2):81–8.
71. Alaerts L, Séguin E, Poelman H, Thibault-Starzyk F, Jacobs PA, de Vos DE. Probing the Lewis Acidity and Catalytic Activity of the Metal–Organic Framework [Cu3(btc)2] (BTC=Benzene-1,3,5-tricarboxylate). Chemistry – A European Journal. 2006 Sep 25;12(28):7353–63.
72. Kuruppathparambil RR, Babu R, Jeong HM, Hwang GY, Jeong GS, Kim M il, et al. A solid solution zeolitic imidazolate framework as a room temperature efficient catalyst for the chemical fixation of CO2. Green Chemistry. 2016;18(23):6349–56.
73. Chen YZ, Zhou YX, Wang H, Lu J, Uchida T, Xu Q, et al. Multifunctional PdAg@MIL-101 for One-Pot Cascade Reactions: Combination of Host-Guest Cooperation and Bimetallic Synergy in Catalysis. ACS Catal. 2015 Apr 3;5(4):2062–9.
74. Chen YZ, Zhang R, Jiao L, Jiang HL. Metal–organic framework-derived porous materials for catalysis. Coord Chem Rev. 2018 May 1;362:1–23.
75. Lin L, Liu H, Zhang X. Flower-Like ZnO-Assisted One-Pot Encapsulation of Noble Metal Nanoparticles Supported Catalysts with ZIFs. Appl Surf Sci. 2018 Mar 1;433:602–9.
76. Yang S, Zhang ZH, Chen Q, He MY, Wang L. Magnetically Recyclable Metal–Organic Framework@Fe3O4 Composite-Catalyzed Facile Reduction of Nitroarene Compounds in Aqueous Medium. Appl Organomet Chem. 2018 Mar 1;32(3):e4132.
77. Qian Q, Asinger PA, Lee MJ, Han G, Mizrahi Rodriguez K, Lin S, et al. MOF-Based Membranes for Gas Separations. Chem Rev. 2020 Aug 26;120(16):8161–266.

78. Wen Y, Zhang X, Li X, Wang Z, Tang CY. Metal-Organic Framework Nanosheets for Thin-Film Composite Membranes with Enhanced Permeability and Selectivity. ACS Appl Nano Mater. 2020 Sep 25;3(9):9238–48.
79. Tanh Jeazet HB, Staudt C, Janiak C. Metal–organic frameworks in mixed-matrix membranes for gas separation. Dalton Transactions. 2012 Nov 6;41(46):14003–27.
80. Robeson LM. The upper bound revisited. J Memb Sci. 2008 Jul 15;320(1–2):390–400.
81. Li L, Yao J, Wang X, Cheng YB, Wang H. ZIF-11/Polybenzimidazole composite membrane with improved hydrogen separation performance. J Appl Polym Sci. 2014 Nov 15;131(22):41056.
82. Yang T, Chung TS. High performance ZIF-8/PBI nano-composite membranes for high temperature hydrogen separation consisting of carbon monoxide and water vapor. Int J Hydrogen Energy. 2013 Jan 11;38(1):229–39.
83. Krokidas P, Moncho S, Brothers EN, Castier M, Economou IG. Tailoring the gas separation efficiency of metal organic framework ZIF-8 through metal substitution: A computational study. Physical Chemistry Chemical Physics. 2018;20(7):4879–92.
84. Krokidas P, Castier M, Moncho S, Brothers E, Economou IG. Molecular simulation studies of the diffusion of methane, ethane, propane, and propylene in ZIF-8. The Journal of Physical Chemistry C. 2015;119(48):27028–27037.
85. Kaur G, Rai RK, Tyagi D, Yao X, Li PZ, Yang XC, et al. Room-temperature synthesis of bimetallic Co-Zn based zeolitic imidazolate frameworks in water for enhanced CO2 and H2 uptakes. J Mater Chem A Mater. 2016;4(39):14932–8.
86. Umeyama D, Horike S, Inukai M, Itakura T, Kitagawa S. Reversible solid-to-liquid phase transition of coordination polymer crystals. J Am Chem Soc. 2015;137(2):864–70.
87. Healy C, Patil KM, Wilson BH, Hermanspahn L, Harvey-Reid NC, Howard BI, et al. The thermal stability of metal-organic frameworks. Coord Chem Rev. 2020 Sep 15;419:213388.
88. Burtch NC, Jasuja H, Walton KS. Water stability and adsorption in metal-organic frameworks. Chem Rev. 2014 Oct 22;114(20):10575–612.
89. Nugent P, Giannopoulou EG, Burd SD, Elemento O, Giannopoulou EG, Forrest K, et al. Porous materials with optimal adsorption thermodynamics and kinetics for CO2 separation. Nature 2013 495:7439. 2013 Feb 27;495(7439):80–4.
90. Wade CR, Corrales-Sanchez T, Narayan TC, Dincă M. Postsynthetic tuning of hydrophilicity in pyrazolate MOFs to modulate water adsorption properties. Energy Environ Sci. 2013 Jun 21;6(7):2172–7.
91. Jasuja H, Burtch NC, Huang YG, Cai Y, Walton KS. Kinetic water stability of an isostructural family of zinc-based pillared metal-organic frameworks. Langmuir [Internet]. 2013 Jan 15 [cited 2022 Sep 12];29(2):633–42. Available from: https://pubs.acs.org/doi/full/10.1021/la304204k

92. Low JJ, Benin AI, Jakubczak P, Abrahamian JF, Faheem SA, Willis RR. Virtual high throughput screening confirmed experimentally: Porous coordination polymer hydration. J Am Chem Soc. 2009 Nov 4;131(43):15834–42.
93. McKinstry C, Cathcart RJ, Cussen EJ, Fletcher AJ, Patwardhan S v., Sefcik J. Scalable continuous solvothermal synthesis of metal organic framework (MOF-5) crystals. Chemical Engineering Journal. 2016 Feb 1;285:718–25.
94. Greenwood N. N., Earnshaw A. Chemistry of Elements. 2nd ed. Sykepleien. Butterworth-Heinemann; 1997.
95. Frentzel-Beyme L, Kloß M, Pallach R, Salamon S, Moldenhauer H, Landers J, et al. Porous purple glass – a cobalt imidazolate glass with accessible porosity from a meltable cobalt imidazolate framework. J Mater Chem A Mater. 2019 Jan 15;7(3):985–90.
96. Stepniewska M, Østergaard MB, Zhou C, Yue Y. Towards large-size bulk ZIF-62 glasses via optimizing the melting conditions. J Non Cryst Solids. 2020;530(December 2019):119806.
97. Zhou C, Stepniewska M, Longley L, Ashling CW, Chater PA, Keen DA, et al. Thermodynamic features and enthalpy relaxation in a metal-organic framework glass. Physical Chemistry Chemical Physics. 2018;20(27):18291–6.
98. Umeyama D, Funnell NP, Cliffe MJ, Hill JA, Goodwin AL, Hijikata Y, et al. Glass formation via structural fragmentation of a 2D coordination network. Chemical Communications. 2015;51(64):12728–31.
99. Horike S, Ma N, Fan Z, Kosasang S, Smedskjaer MM. Mechanics, Ionics, and Optics of Metal–Organic Framework and Coordination Polymer Glasses. Nano Lett. 2021;
100. Bumstead AM, Ríos Gómez ML, Thorne MF, Sapnik AF, Longley L, Tuffnell JM, et al. Investigating the melting behaviour of polymorphic zeolitic imidazolate frameworks. CrystEngComm. 2020 Jun 1;22(21):3627–37.
101. Bennett TD, Yue Y, Li P, Qiao A, Tao H, Greaves NG, et al. Melt-Quenched Glasses of Metal-Organic Frameworks. J Am Chem Soc. 2016;138(10):3484–92.
102. Hou J, Ríos Gómez ML, Krajnc A, McCaul A, Li S, Bumstead AM, et al. Halogenated Metal-Organic Framework Glasses and Liquids. J Am Chem Soc. 2020;142(8):3880–90.
103. Thorne MF, Gómez MLR, Bumstead AM, Li S, Bennett TD. Mechanochemical synthesis of mixed metal, mixed linker, glass-forming metal–organic frameworks. Green Chemistry. 2020 Apr 27;22(8):2505–12.
104. Bumstead AM, Thorne MF, Bennett TD. Identifying the liquid and glassy states of coordination polymers and metal-organic frameworks. Faraday Discuss. 2021;225(Im):210–25.
105. Ríos Gómez ML, Lampronti GI, Yang Y, Mauro JC, Bennett TD. Relating structural disorder and melting in complex mixed ligand zeolitic imidazolate framework glasses. Dalton Transactions. 2020 Jan 21;49(3):850–7.
106. Zheng Q, Zhang Y, Montazerian M, Gulbiten O, Mauro JC, Zanotto ED, et al. Understanding Glass through Differential Scanning Calorimetry. Chem Rev. 2019;119(13):7848–939.

107. Zhang J, Longley L, Liu H, Ashling CW, Chater PA, Beyer KA, et al. Structural evolution in a melt-quenched zeolitic imidazolate framework glass during heat-treatment. Chemical Communications. 2019;55(17):2521–4.
108. Frentzel-Beyme L, Kloß M, Kolodzeiski P, Pallach R, Henke S. Meltable Mixed-Linker Zeolitic Imidazolate Frameworks and Their Microporous Glasses: From Melting Point Engineering to Selective Hydrocarbon Sorption. J Am Chem Soc. 2019;141:12362–71.
109. Ito K, Moynihan CT, Austen Angell C. Thermodynamic determination of fragility in liquids and a fragile-to-strong liquid transition in water. Nature . 1999 Apr 8;398(6727):492–5.
110. Orava J, Greer AL. Fast and slow crystal growth kinetics in glass-forming melts. J Chem Phys. 2014 Jun 5;140(21):214504.
111. Henke S, Wharmby MT, Kieslich G, Hante I, Schneemann A, Wu Y, et al. Pore closure in zeolitic imidazolate frameworks under mechanical pressure. Chem Sci. 2018;9(6):1654–60.
112. Wharmby MT, Henke S, Bennett TD, Bajpe SR, Schwedler I, Thompson SP, et al. Extreme Flexibility in a Zeolitic Imidazolate Framework: Porous to Dense Phase Transition in Desolvated ZIF-4. Angewandte Chemie International Edition. 2015 May 26;54(22):6447–51.
113. Widmer RN, Lampronti GI, Anzellini S, Gaillac R, Farsang S, Zhou C, et al. Pressure promoted low-temperature melting of metal–organic frameworks. Nat Mater. 2019;18(4):370–6.
114. Gaillac R, Pullumbi P, Coudert FX. Melting of Zeolitic Imidazolate Frameworks with Different Topologies: Insight from First-Principles Molecular Dynamics. Journal of Physical Chemistry C. 2018;122(12):6730–6.
115. Zhao Y, Lee SY, Becknell N, Yaghi OM, Angell CA. Nanoporous Transparent MOF Glasses with Accessible Internal Surface. J Am Chem Soc. 2016;138(34):10818–21.
116. Chen B, Yang Z, Zhu Y, Xia Y. Zeolitic imidazolate framework materials: Recent progress in synthesis and applications. J Mater Chem A Mater. 2014;2(40):16811–31.
117. Kertik A, Wee LH, Sentosun K, Navarro JAR, Bals S, Martens JA, et al. High-Performance CO2-Selective Hybrid Membranes by Exploiting MOF-Breathing Effects. ACS Appl Mater Interfaces. 2020;12(2):2952–61.
118. Kwon HT, Jeong HK. In situ synthesis of thin zeolitic-imidazolate framework ZIF-8 membranes exhibiting exceptionally high propylene/propane separation. J Am Chem Soc. 2013;135(29):10763–8.
119. Pimentel BR, Parulkar A, Zhou EK, Brunelli NA, Lively RP. Zeolitic imidazolate frameworks: Next-generation materials for energy-efficient gas separations. ChemSusChem. 2014;7(12):3202–40.
120. Coudert FX, Fuchs AH. Computational characterization and prediction of metal–organic framework properties. Coord Chem Rev. 2016;307:211–236.
121. Getman RB, Bae YS, Wilmer CE, Snurr RQ. Review and analysis of molecular simulations of methane, hydrogen, and acetylene storage in metal–organic frameworks. Chem Rev. 2011;112(2):703–723.

122. Tan JC, Civalleri B, Lin CC, Valenzano L, Galvelis R, Chen PF, et al. Exceptionally low shear modulus in a prototypical imidazole-based metal-organic framework. Phys Rev Lett. 2012;108(9):095502.
123. Tan JC, Bennett TD, Cheetham AK. Chemical structure, network topology, and porosity effects on the mechanical properties of zeolitic imidazolate frameworks. Proc Natl Acad Sci U S A. 2010;107(22):9938–43.
124. Walker AM, Civalleri B, Slater B, Mellot-Draznieks C, Corà F, Zicovich-Wilson CM, et al. Flexibility in a Metal–Organic Framework Material Controlled by Weak Dispersion Forces: The Bistability of MIL-53 (Al). Angewandte Chemie International Edition. 2010;49(41):7501–7503.
125. Gao M, Misquitta AJ, Rimmer LH, Dove MT. Molecular dynamics simulation study of various zeolitic imidazolate framework structures. Dalton Transactions. 2016;45(10):4289–4302.
126. Boyd PG, Moosavi SM, Witman M, Smit B. Force-Field Prediction of Materials Properties in Metal-Organic Frameworks. J Phys Chem Lett. 2017;8(2):357–363.
127. Zhang L, Hu Z, Jiang J. Sorption-induced structural transition of zeolitic imidazolate framework-8: a hybrid molecular simulation study. J Am Chem Soc. 2013;135(9):3722–3728.
128. Hu Z, Chen Y, Jiang J. Zeolitic imidazolate framework-8 as a reverse osmosis membrane for water desalination: Insight from molecular simulation. J Chem Phys. 2011;134(13):134705.
129. Yang Y, Shin YK, Li S, Bennett TD, van Duin AC, Mauro JC. Enabling Computational Design of ZIFs Using ReaxFF. J Phys Chem B. 2018;122:9616–24.
130. Yang Y, Wilkinson CJ, Lee KH, Doss K, Bennett TD, Shin YK, et al. Prediction of the Glass Transition Temperatures of Zeolitic Imidazolate Glasses through Topological Constraint Theory. Journal of Physical Chemistry Letters. 2018;9(24):6985–90.
131. Gaillac R, Pullumbi P, Beyer KA, Chapman KW, Keen DA, Bennett TD, et al. Liquid metal–organic frameworks. Nat Mater. 2017;16(11):1149–55.
132. Greaves GN. Hybrid Glasses: From Metal Organic Frameworks and Co-ordination Polymers to Hybrid Organic Inorganic Perovskites. In: Springer Handbook of Glass. 2019. p. 719–65.
133. Gan Z, Hung I, Wang X, Paulino J, Wu G, Litvak IM, et al. NMR spectroscopy up to 35.2T using a series-connected hybrid magnet. J Magn Reson. 2017 Nov 1;284:125–36.
134. Sutrisno A, Terskikh V v., Shi Q, Song Z, Dong J, Ding SY, et al. Characterization of zn-containing metal-organic frameworks by solid-state 67Zn NMR spectroscopy and computational modeling. Chemistry - A European Journal. 2012;18(39):12251–9.
135. Kentgens APM. A practical guide to solid-state NMR of half-integer quadrupolar nuclei with some applications to disordered systems. Geoderma. 1997;80(3–4):271–306.

136. Mroué KH, Power WP. High-field solid-state 67Zn NMR spectroscopy of several zinc-amino acid complexes. Journal of Physical Chemistry A. 2010;114(1):324–35.
137. Bastow TJ. 67Zn-NMR in zinc metal. Journal of Physics: Condensed Matter. 1996;8:11309–15.
138. Wu G, Kroeker S, Wasylishen RE. Multimiclear NMR Study of Dipotassium Tetracyanometalates of the Group 12 Metals in the Solid State. Inorg Chem. 1995;34(6):1595–8.
139. Larsen FH, Lipton AS, Jakobsen HJ, Nielsen NC, Ellis PD. 67Zn QCPMG solid-state NMR studies of zinc complexes as models for metalloproteins [3]. J Am Chem Soc. 1999;121(15):3783–4.
140. Lipton AS, Heck RW, Ellis PD. Zinc Solid-State NMR Spectroscopy of Human Carbonic Anhydrase: Implications for the Enzymatic Mechanism. J Am Chem Soc. 2004;126(14):4735–9.
141. Kjeldsen J, Smedskjaer MM, Mauro JC, Yue Y. Hardness and incipient plasticity in silicate glasses: Origin of the mixed modifier effect. Appl Phys Lett. 2014 Feb 7;104(5):051913.
142. Kjeldsen J, Smedskjaer MM, Mauro JC, Yue Y. On the origin of the mixed alkali effect on indentation in silicate glasses. J Non Cryst Solids. 2014 Dec 15;406:22–6.
143. le Bail A., Duroy H., FourQuet J. L. AB-INITIO STRUCTURE DETERMINATION OF LiSbW08 BY X-RAY POWDER DIFFRACTION. Mat Res Bull. 1988;23(c):447–52.
144. Denton A. R., Ashcroft N. W. Vegard's law. Phys Rev A (Coll Park). 1991;43(6):3161–4.
145. Smedskjaer MM, Mauro JC, Youngman RE, Hogue CL, Potuzak M, Yue Y. Topological principles of borosilicate glass chemistry. Journal of Physical Chemistry B. 2011;115(44):12930–46.
146. Madsen RSK, Sarkar S, Iversen BB, Yue Y. Sensitivity of the glass transition and melting in a metal–organic framework to ligand chemistry. Chemical Communications. 2022;58(6):823–6.
147. Bax A. A spatially selective composite 90° radiofrequency pulse. Journal of Magnetic Resonance (1969). 1985;65(1):142–5.
148. Madsen RSK, Stepniewska M, Yang Y, Qiao A, Winters WMW, Zhou C, et al. Mixed metal node effect in zeolitic imidazolate frameworks. RSC Adv. 2022;12(17):10815–24.
149. P. J. Linstrom, W. G. Mallard. NIST Chemistry WebBook National Institute of Standards and Technology, Gaithersburg MD. NIST Standard Reference Database Number 69. 2005. p. 20899.
150. Grimme S, Antony J, Ehrlich S, Krieg H. A consistent and accurate ab initio parametrization of density functional dispersion correction (DFT-D) for the 94 elements H-Pu. Journal of Chemical Physics. 2010;132(15).
151. Birch F. Finite elastic strain of cubic crystals. Physical review. 1947;71(11):809.
152. Plimpton S. Fast parallel algorithms for short-range molecular dynamics. J Comput Phys. 1995;117(1):1–19.

153. Addicoat MA, Vankova N, Akter IF, Heine T. Extension of the universal force field to metal–organic frameworks. J Chem Theory Comput. 2014;10(2):880–891.
154. Coupry DE, Addicoat MA, Heine T. Extension of the universal force field for metal–organic frameworks. J Chem Theory Comput. 2016;12(10):5215–5225.
155. Rappé AK, Casewit CJ, Colwell K, Goddard Iii W, Skiff W. UFF, a full periodic table force field for molecular mechanics and molecular dynamics simulations. J Am Chem Soc. 1992;114(25):10024–10035.
156. Vanduyfhuys L, Vandenbrande S, Wieme J, Waroquier M, Verstraelen T, van Speybroeck V. Extension of the QuickFF force field protocol for an improved accuracy of structural, vibrational, mechanical and thermal properties of metal–organic frameworks. J Comput Chem. 2018;39(16):999–1011.
157. Li K, Ding Z, Xue D. Composition dependence of bulk modulus and bond length of Mg xZn1-xO(x = 0.0-1.0) alloy semiconductors. Functional Materials Letters. 2010;3(4):241–4.
158. Brown ID, Klages P, Skowron A. Influence of pressure on the lengths of chemical bonds. Acta Crystallogr B. 2003;59(4):439–48.
159. Chen L, Mashimo T, Iwamoto C, Okudera H, Omurzak E, Ganapathy HS, et al. Synthesis of novel CoCx@C nanoparticles. Nanotechnology. 2013;24(4).
160. Radhakrishnan D, Narayana C. Effect of pore occupancy on the acoustic properties of zeolitic imidazolate framework (ZIF)-8: A Brillouin spectroscopic study at ambient and low temperatures. Journal of Chemical Physics. 2015;143(23).
161. Khandelwal G, Maria Joseph Raj NP, Kim SJ. ZIF-62: a mixed linker metal-organic framework for triboelectric nanogenerators. J Mater Chem A Mater. 2020;8(34):17817–25.
162. Massiot D, Fayon F, Capron M, King I, le Calvé S, Alonso B, et al. Modelling one- and two-dimensional solid-state NMR spectra. Magnetic Resonance in Chemistry. 2002;40(1):70–6.
163. d'Espinose de Lacaillerie JB, Fretigny C, Massiot D. MAS NMR spectra of quadrupolar nuclei in disordered solids: The Czjzek model. Journal of Magnetic Resonance. 2008;192(2):244–51.
164. Siegel R, Nakashima TT, Wasylishen RE. Sensitivity enhancement of NMR spectra of half-integer quadrupolar nuclei in the solid state via population transfer. Concepts in Magnetic Resonance Part A. 2005 Jul 1;26A(2):47–61.
165. Kupče Ē, Freeman R. Adiabatic Pulses for Wideband Inversion and Broadband Decoupling. J Magn Reson A. 1995 Aug 1;115(2):273–6.
166. Harris RK, Becker ED, de Menezes SMC, Goodfellow R, Granger P. NMR Nomenclature: Nuclear Spin Properties and Conventions for Chemical Shifts: IUPAC Recommendations 2001. Solid State Nucl Magn Reson. 2002 Dec 1;22(4):458–83.
167. Spearing DR. ptchg: A FORTRAN program for point-charge calculations of electric field gradients (EFGs). Comput Geosci. 1994 May 1;20(4):615–24.

168. Bennett TD, Yue Y, Li P, Qiao A, Tao H, Greaves NG, et al. Melt-Quenched Glasses of Metal-Organic Frameworks. J Am Chem Soc. 2016;138(10):3484–92.
169. Stepniewska M. Fabrication and Mechanical Properties of Melt-Quenched Zeolitic Imidazolate Glasses. G. Balint, Antala B, Carty C, Mabieme JMA, Amar IB, Kaplanova A, editors. Aalborg Universitetsforlag. [Aalborg]; 2019.
170. Liu M, McGillicuddy RD, Vuong H, Tao S, Slavney AH, Gonzalez MI, et al. Network-forming liquids from metal-bis(acetamide) frameworks with low melting temperatures. J Am Chem Soc. 2021 Feb 24;143(7):2801–11.
171. Sarkar S, Bjørn T, Grønbech E, Mamakhel A, Bondesgaard M, Sugimoto K, et al. X-ray Electron Density Study of the Chemical Bonding Origin of Glass Formation in Metal–Organic Frameworks**. Angewandte Chemie. 2022 May 23;134(22):e202202742.
172. Zumdahl SS, DeCoste DJ. Chemical Principles. Vol. 136, Journal of Experimental Psychology: General. Mary Finch; 2007. 1–1199 p.
173. Adhikari P, Xiong M, Li N, Zhao X, Rulis P, Ching WY. Structure and Electronic Properties of a Continuous Random Network Model of an Amorphous Zeolitic Imidazolate Framework (a-ZIF). Journal of Physical Chemistry C. 2016;120(28):15362–8.
174. Bennett TD, Goodwin AL, Dove MT, Keen DA, Tucker MG, Barney ER, et al. Structure and properties of an amorphous metal-organic framework. Phys Rev Lett. 2010;104(11):2–5.
175. Bennett TD, Keen DA, Tan JC, Barney ER, Goodwin AL, Cheetham AK. Thermal Amorphization of Zeolitic Imidazolate Frameworks. Angewandte Chemie International Edition. 2011 Mar 21;50(13):3067–71.
176. Lindemann FA. The calculation of molecular vibration frequencies. Physik Z. 1910;11:609–12.
177. Gaillac R, Pullumbi P, Beyer KA, Chapman K, Keen DA, Bennett TD, et al. Liquid metal–organic frameworks. Nat Mater. 2017;16(11):1149–55.
178. Friebolin H. Basic One and Two Dimensional NMR Spectroscopy. Basic One- and Two-Dimensional Spectroscopy. 5th Edition. Wiley-VCH; 2010.
179. Li JJ. Name Reactions. Name Reactions. Springer International Publishing; 2021.
180. McMurry J. Organic Chemistry. Organic chemistry. Cengage Learning, Inc; 2016. 1512 p.
181. Espinal Viguri M, Huertos MA, Pérez J, Riera L, Ara I. Re-mediated C-C coupling of pyridines and imidazoles. J Am Chem Soc. 2012 Dec 19;134(50):20326–9.
182. Gersten JI (Joel I, Smith FW (Frederick W. The physics and chemistry of materials. Wiley; 2001. 826 p.
183. du J. Molecular Dynamic Simulations of Oxide Glasses. In: Musgraves, Hu, Calvez, editors. Springer Handbook o*f* Glass . 2019. p. 1129–53.
184. Ching WY. First-Principles Calculation. Springer Handbook of Glass. 2019;1095–122.
185. Hafner J. Ab-initio simulations of materials using VASP: Density-functional theory and beyond. J Comput Chem. 2008;29(13):2044–78.

186. Ching WY, Rulis P. Electronic Structure Methods for Complex Materials: The orthogonalized linear combination of atomic orbitals. Electronic Structure Methods for Complex Materials: The Orthogonalized Linear Combination of Atomic Orbitals. Oxford University Press; 2012. 1–328 p.
187. Dickel D, Mun S, Baskes M, Gwaltney S, Prabhu RK, Horstemeyer MF. Density functional theory and bridging to classical interatomic force fields. Multiscale Biomechanical Modeling of the Brain. 2022 Jan 1;39–52.
188. Christensen JFS, Sørensen SS, To T, Bauchy M, Smedskjaer MM. Toughening of soda-lime-silica glass by nanoscale phase separation: Molecular dynamics study. Phys Rev Mater. 2021 Sep 1;5(9):093602.
189. Vargheese KD, Tandia A, Mauro JC. Molecular dynamics simulations of ion-exchanged glass. J Non Cryst Solids. 2014 Nov 1;403:107–12.
190. Du J, Chen CH. Structure and lithium ion diffusion in lithium silicate glasses and at their interfaces with lithium lanthanum titanate crystals. J Non Cryst Solids. 2012 Dec 15;358(24):3531–8.
191. Deng L, Du J. Development of effective empirical potentials for molecular dynamics simulations of the structures and properties of boroaluminosilicate glasses. J Non Cryst Solids. 2016 Dec 1;453:177–94.
192. I15-1 - Diamond Light Source [Internet]. [cited 2022 Sep 11]. Available from: https://www.diamond.ac.uk/Instruments/Crystallography/I15-1.html#
193. Basham M, Filik J, Wharmby MT, Chang PCY, el Kassaby B, Gerring M, et al. Data Analysis WorkbeNch (DAWN). J Synchrotron Radiat. 2015 May 1;22(3):853–8.
194. Filik J, Ashton AW, Chang PCY, Chater PA, Day SJ, Drakopoulos M, et al. Processing two-dimensional X-ray diffraction and small-angle scattering data in DAWN 2. Journal of applied crystallography . 2017 May 8;50(3):959–66.
195. Hart ML, Drakopoulos M, Reinhard C, Connolley T. Complete elliptical ring geometry provides energy and instrument calibration for synchrotron-based two-dimensional X-ray diffraction. J Appl Crystallogr. 2013 Oct;46(Pt 5):1249–60.
196. Soper AK. GudrunN and GudrunX Programs for correcting raw neutron and x-ray total scattering data to differential cross section. 2012. p. 1–148.
197. I12 – Diamond Light Source [Internet]. [cited 2022 Sep 11]. Available from: https://www.diamond.ac.uk/Instruments/Imaging-and-Microscopy/I12.html
198. Drakopoulos M, Connolley T, Reinhard C, Atwood R, Magdysyuk O, Vo N, et al. I12: the Joint Engineering, Environment and Processing (JEEP) beamline at Diamond Light Source. urn:issn:1600-5775. 2015 Apr 8;22(3):828–38.
199. Moghadam PZ, Li A, Wiggin SB, Tao A, Maloney AGP, Wood PA, et al. Development of a Cambridge Structural Database Subset: A Collection of Metal − Organic Frameworks for Past, Present, and Future. 2017;
200. Longley L, Collins SM, Zhou C, Smales GJ, Norman SE, Brownbill NJ, et al. Liquid phase blending of metal-organic frameworks. Nat Commun. 2018;9(1):2–11.
201. Nozari V, Calahoo C, Longley L, Bennett TD, Wondraczek L. Structural integrity, meltability, and variability of thermal properties in the mixed-linker

zeolitic imidazolate framework ZIF-62. J Chem Phys. 2020 Nov 23;153(20):204501.
202. Suwaiyan A, Zwaricht R, Baig N. Infrared and Raman Spectra of Benzimidazole. Vol. 21, JOURNAL OF RAMAN SPECTROSCOPY. 1990.
203. Kim MS, Kim MK, Lee CJ, Jung YM, Lee MS. Surface-enhanced Raman Spectroscopy of Benzimidazolic Fungicides: Benzimidazole and Thiabendazole. Bull Korean Chem Soc. 2009 Dec;30(12):2930–4.
204. Han X, Chen W, Su R, Tian Y, Liu P, Guan P, et al. Visualizing the {110} surface structure of equilibrium-form ZIF-8 crystals by low-dose Cs-corrected TEM. Nanoscale. 2021 Aug 12;13(31):13215–9.
205. Żak A. Guide to controlling the electron dose to improve low-dose imaging of sensitive samples. Micron. 2021 Jun 1;145:103058.
206. Lewis IR, Edwards H. Handbook of Raman Spectroscopy : From the Research Laboratory to the Process Line. Handbook of Raman Spectroscopy. 2001 Aug 8;
207. Takenaka K. Negative thermal expansion materials: technological key for control of thermal expansion. http://www.tandfonline.com/action/journalInformation?show=aimsScope&journalCode=tsta20#VmBmuzZFCUk. 2012 Feb;13(1):11.
208. Kashiwaya Y, Iwasa M, Ishii K. Kinetic Analysis of the Gasification of Diamond. Mater Trans. 2008 Jul 1;49(7):1563–71.

ISSN (online): 2446-1636
ISBN (online): 978-87-7573-792-5

AALBORG UNIVERSITY PRESS